TECHNISCHE UNIVERSITÄT WIEN

ILSB

MASTER THESIS

Mechanical testing of individual osteons of cortical bone

carried out for the purpose of obtaining the degree of Master of Science (MSc)
submitted at TU Wien, Faculty of Mechanical and Industrial Engineering, by

Maria KOZYREV
Mat.Nr.:01128661

under supervision of

Univ.Prof. Dipl.-Ing. Dr.sc.nat. Philipp J THURNER
Dr.sc.nat. Caitlyn COLLINS
Institute of Lightweight Design and Structural Biomechanics

Vienna, September, 2017

Mechanical testing of individual Osteons of Cortical bone

Maria Kozyrev

Mat.Nr.:01128661

Declaration of Authorship

I confirm, that going to press of this thesis needs the confirmation of the examination committee.

Affidavit

I declare in lieu of oath, that I wrote this thesis and performed the associated research myself, using only literature cited in this volume. If text passages from sources are listed literally, they are marked as such.
I confirm that this work is original and has not been submitted elsewhere for any examination, nor is it currently under consideration for a thesis elsewhere.

Vienna, September, 2017

Mechanical testing of individual Osteons of Cortical bone

Maria Kozyrev

Mat.Nr.:01128661

Acknowledgments

I would like to express my sincere gratitude to my thesis advisor prof. Philipp Thurner for his continuous guidance. I appreciate the opportunity and trust I have been given. I would also like to thank my second thesis advisor Caitlyn Collins, for sharing her professional knowledge, guidance, support and encouragement. She was open for help, whenever I ran into a trouble spot or had a question about my research or writing.

I am also grateful to Orestis Andriotis who helped me with the SHG measurments. Many thanks to Andreas Reisinger for supporting me at the first steps of the project. Many thanks go to Robert Exler for manufacturing all the needed experimental equipment. I would also like to thank Martin Frank and Vedran Nedelkovski for answering my regular questions.

Special words of gratitude to my family and my friends who always listened, supported and believed in me.

Mechanical testing of individual Osteons of Cortical bone

Maria Kozyrev

Mat.Nr.:01128661

Abstract

An increase in incidence of bone fractures, related to ageing or bone disease, is a significant socio-economic burden. The reasons for the impaired mechanical function of cortical bone are difficult to identify, due to the limited understanding of mechanical properties of the basic functional unit of cortical bone, the osteon. Secondary osteons are formed as a result of bone remodelling and adaptation processes. Ageing and bone disease debilitate bone remodelling function leading to bone loss and increased bone fragility. The technique that is currently used to diagnose bone diseases and predict pathological fractures is based on the bone mineral density measure. As the diagnosis is often made only after the occurrence of the pathological fracture, the need in development of new techniques to assess the "quality" of bone is increasing. Understanding the mechanical function of the osteon, as a product of the bone remodelling process, can provide vital insights into mechanisms of bone change with ageing and disease. The compressive mechanical properties of single osteons were studied by Ascenzi et al. in 1968 [1] and the results reported by the research group were not validated so far. In this master thesis, a methodology was developed to extract individual osteons from the bulk material of bone and test them in uni-axial compression. Bovine bone was used to calibrate and optimize the developed procedure. Furthermore, this thesis provides insights on how ageing can possibly affect the mechanical properties of human osteons. Bone tissue from two male donors, ages 64 and 93, was used to harvest two sets of osteons. The results of continuous and step-wise uni-axial compression testing suggest that there is a difference in mechanical properties between the two age groups of osteons. The younger osteon group consistently showed a higher variation in the measured parameters compared to the older group. Additionally, the younger donor had more osteons with lower σ_{max}, σ_{yield} and higher ε_{max}, ε_{yield} and, therefore, were more ductile. Elastic modulus and bone mineral density of the older osteon group ($E = 6.6[1.5]$ GPa, $BMD = 1214$ [32] mg HA/ccm) were found to be higher (ANOVA, $p < 0.05$) than those of the younger osteon group ($E = 4.7[1.1]$ GPa, $BMD = 1186$ [31] mg HA/ccm). However, recent research suggest that damage may accumulate already within an apparent elastic region leading to possibly underestimated values of elastic modulus [2]. In this thesis, the results of the step-wise compression testing suggested that the values of elastic modulus determined by the uniaxial compression testing are underestimated up to 1.7 times and that micro-damage accumulates within the apparent elastic region. Furthermore, BV/TV and *SHG intensity* were found to be the only significant predictors of the osteonal mechanical properties (regression analysis, $p < 0.05$). Investigating the differences in osteonal structural and mechanical properties may be the key to a better understanding of bone ageing and pathological processes.

Contents

List of Figures

List of Tables

Chapter 1

Introduction

1.1 Motivation

Musculoskeletal disorders are estimated to be the second most common cause of disability worldwide, with an increase of 45% between years 1990 and 2010. [3] Disability due to musculoskeletal diseases impose a great economic burden on the life of the individual as well as on social and economic systems. In 2015 the aggregated cost of musculoskeletal disease took up 5.7 % of the United States' gross domestic profit (GDP) [4].

Bone fragility diseases account for a large fraction of the aforementioned burden, they include osteoporosis, osteogenesis imperfecta, Rickets, osteomalacia, Paget's disease, osteopetrosis and hyperpadathiodism. A debilitated skeletal system substantially lowers the quality of life of the patient and increases fracture risks. The increasing incidence of pathological fractures indicates a clear need for an improvement in the current approach to diagnosis, prevention and treatment of bone diseases [5].

As an example, osteoporosis is often diagnosed only after a low-trauma fracture has already occurred. For asymptomatic patients the diagnosis of osteoporosis and assessment of fracture risks are based on bone mineral density (BMD) values, which are most commonly determined by dual-energy x-ray absorptiommetry (DXA) [6]. This diagnositc method assumes that bone mass per unit volume is the main factor influencing fracture strength of the bone. DXA measured BMD values from the patient are compared to the statistically averaged ones from a young healthy population and this comparison determines the diagnosis of the patient.

Over recent decades it has become clear that BMD, as a determinant of bone fracture risk, is not sufficient for the successful diagnosis and treatment of the bone disease [7, 8]. Challenges in developing new approaches for diagnosis and treatment arise due to poor understanding of bone's complex structure and its mechanobiological behavior. Bone is an organic/inorganic, hierarchically-organized structure that undergoes constant remodeling. Seven hierarchical levels are commonly distinguished [9], ranging from the whole bone level to the nano-level which is made up of the basic bone components such as collagen, mineral, noncollagenous proteins and water. Mechanical and material properties differ within these hierarchical levels. Bone at the macro-level has been extensively studied, establishing that bone is anisotropic, heterogeneous and generally inelastic. Structurally, bone can be distinguished into cortical bone, which provides all bones with their shape, and trabecular bone, which is highly porous and is

situated within the ends of long bones. Mechanical properties of cortical and trabecular bone significantly differ; results from the various methods of mechanical testing state that the elastic modulus of cortical bone at tissue level is 10-26 GPa, whereas similar methods yield an elastic modulus of 1-15 GPa for trabecular bone. The pronounced mechanical strength of cortical bone is explained by its complex composite micro-structure made up of mineralized collagen fibres arrange into sheets called lamellae, that in turn concentrically align to form cylindrical structures called osteons. Osteons stack together, much like the fibres in continuous fibre-reinforced composites, to withstand high mechanical load. As osteons are formed through remodelling processes of bone, they serve as hallmarks of the bone change. However, mechanical properties of single osteons have not yet been clearly established. Compressive mechanical properties of single osteons were studies by Ascenzi et al. in 1968 and since then the values of osteonal the elastic modulus were nor validated. The lack of an established experimental set-up for mechanical testing of micro-structures as well as the lack of a reliable means of harvesting them from the bulk material of bone are the main challenges in investigating the micrometer-scale mechanical properties of bone.

1.2 Project Objectives

In order to get a deeper understanding of the micro-mechanical properties of bone, the following objectives are addressed in this Master's Project:

1. Establish a methodology to harvest single osteons from the bulk material of bone and test them in compression,

2. Evaluate the effects of age on the mechanical properties of human osteons.

Chapter 2

Background

2.1 Structure of bone

The hierarchical organisation of bone and its cell activity distinguish bone from any engineering material (Figure 2.1). Further, this complex organization and activity provides bone with a unique combination of mechanical properties. According to Weiner et. al, the hierarchical structure of bone can be subdivided into seven levels based on structural length scales [9]. The 7th level, or whole bone level, differentiates between individual bones whose macroscale structural properties vary according to anatomical location within the body. There are 206 bones in a human skeleton, taking up to 20% of the body mass [10]. Moving down to the length scale of millimetres (6th level), two types of bone are distinguished:

- Spongy or Trabecular bone: Found at the ends of long bones, trabecular bone accounts for roughly 20% of the total bone mass in the human body and has high porosity (from 75 to 85 % [11]). In the highly porous trabecular bone tissue, the "packets" of bone are arranged to form a network of rods and plates about 100 to 300 μm thick interspersed with large marrow spaces.
- Cortical bone: Found surrounding a central marrow cavity of long bones, cortical bone accounts for 80% of the total bone mass in the human body and has comparatively low porosity (usually <5% [11]).

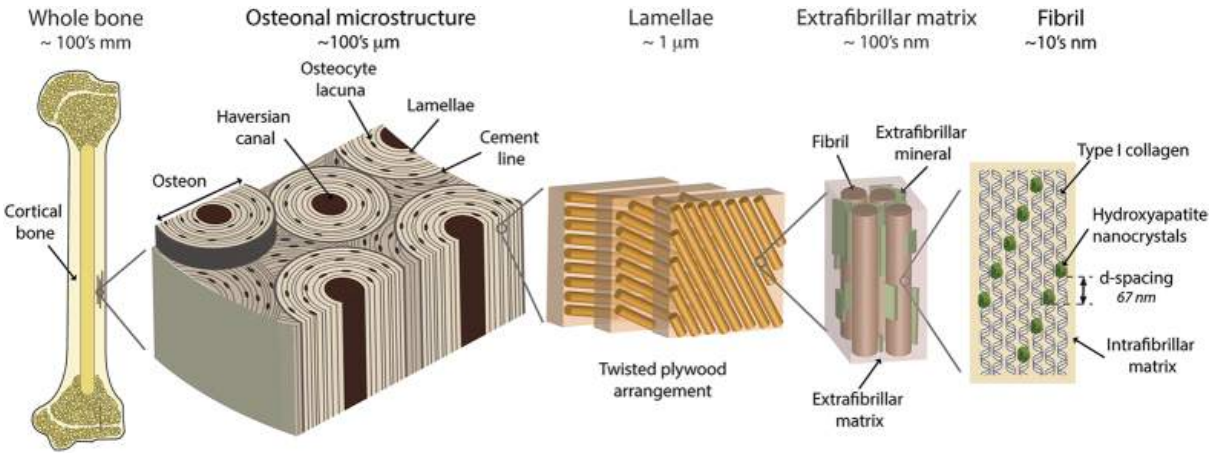

Figure 2.1: Hierarchical organisation of bone. Adapted from [12]

The difference in structure and distribution of trabecular and cortical bone is designed to fulfil different functions in the body.

Trabecular bone's porous structure is adapted to transmit loads, individual trabeculi are organised along the principle direction of stresses and can realign if the direction of stress changes. Due to its great surface area, trabecular bone is ideal for metabolic activity. Trabecular bone marrow is highly vascular, and hematopoiesis often occurs there.

The functions of cortical bone are to support the whole body, protect organs, provide anchorage for muscles, as well as store and release chemical elements. Metabolic activity of cortical bone happens at a much lower rate than that of trabecular bone, and the primary function of cortical bone is to withstand the applied loads and support the body. Therefore, cortical bone is much stiffer than trabecular bone, along with stronger and tougher. The load-bearing ability of cortical bone is ensured by its structural organisation shown in Figure 2.1.

At a sub millimetre-scale or on the 5th level of bone hierarchy, human cortical bone consists of closely packed osteons, interstitial bone and a few layers of lamellar bone in proximity to the periosteum, see Figure 2.2. The functional unit of human cortical bone is the osteon, which is comprised of a central canal, called the Haversian canal, surrounded by concentric rings of lamellae 5-7 μm thick [13]. The structure of the osteon at levels 4 and 3 is described in detail in section 2.2. Osteons formed by the bone remodelling process are called secondary osteons. Interstitial bone is composed of concentric lamellae parts that were not removed by a cutting cone of the bone remodelling process. According to recent research, interstitial and osteonal bone exhibit significantly different mechanical properties [14]. The interface between the secondary osteon and the interstitial bone is surrounded by a thin layer of calcified mucopolysaccharides with very little collagen and low mineral content, this interface is called a cement line. Cement lines are believed to be mechanically weaker than the surrounding tissue and positively contribute to the bone's toughness [15].

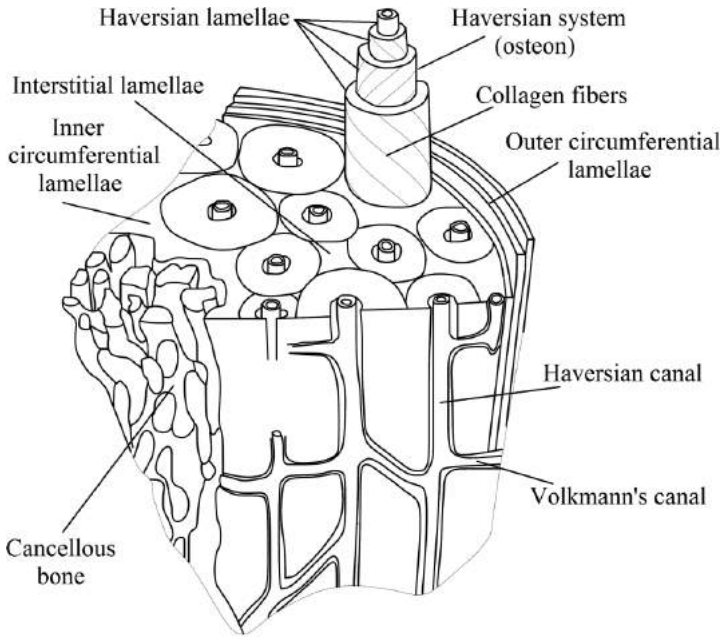

Figure 2.2: Schematic representation of the cortical-trabecular bone. Adapted from [16]

The aforementioned lamellae sheets are comprised of mineralised collagen fibres that are organised in different manners in accordance to the bone sample

site. They are present in both cortical and trabecular bone and correspond to the 4th level of bone hierarchy. On the 3rd and 2nd level, mineralised collagen fibres are composed of mineralised collagen fibrils which, in turn, contain collagen microfibrils and mineral crystals (Figure 2.5a,b,c). The structure of collagen at the nano meter-scale is presented in Figure 2.3.

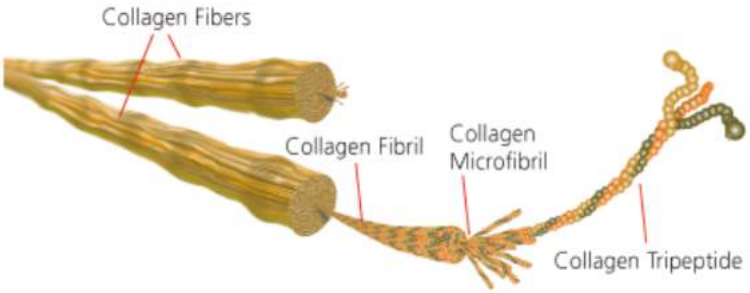

Figure 2.3: Collagen fibre assembly at the nano scale. Adapted from Sigma-Aldrich Co. LLC. web-site (2015)

The organisation of bone at the nano-scale remains a controversial topic in current research. Several models of bone ultrastructure have been proposed. The most commonly accepted model was developed by Hodge Petruska et al. in the 1950s. In this model, a collagen fibril is assumed to contain straight and rod-like collagen molecules arranged in parallels and quarter-staggered, as shown in Figure 2.4a. Mineral crystals are postulated to nucleate and grow within the gap spaces between the ends of collagen molecules. At the later stages of mineralisation, mineral is assumed to grow out of gap channels into the 'intermolecular spaces' (Figure 2.4b) [17]. Parallel collagen arrangement was recently challenged by works of Orgel et al. (2006), who argued that the collagen molecule lattice is helicoidally twisted along the longitudal direction of the molecules (Figure 2.4c), so that mineral platelets can be accommodated in the elongated gap spaces (Figure 2.4d) [18].

On the first level of hierarchy, bone tissue is comprised of inorganic/mineral and organic/non-mineral phases and water. Bone is approximately 60% mineral, 30% non-mineral and 10% water by weight, whereas by volume these proportions are about 40%, 35% and 25%, respectively [20]. The mineral part of bone consists of hydroxyapatite crystals, with the chemical formula $Ca_{10}(PO_4)_6(OH)_2$ (Figure 2.5d). The size of the mineral crystals is reported to change with age, becoming thinner and longer [21].

A variety of proteins compose the non-mineral part of bone. The most abundant protein is type I collagen (90% by weight), the remaining proteins include other collagen types, osteocalcin, osteonectin, osteopontin and bone sialoprotein [17]. A single collagen molecule consist of 3 amino acid helices joined together in a right-handed triple helix. The collagen triple helix is approximately 20 to 40 nm in diameter and up to 500 nm long [22]. At each end of the collagen molecule, non-helical domains are present which are referred to as telopeptides. Collagen molecules are held together by forming cross-links, and telopeptides form the region where collagen cross-linking is believed to initiate.

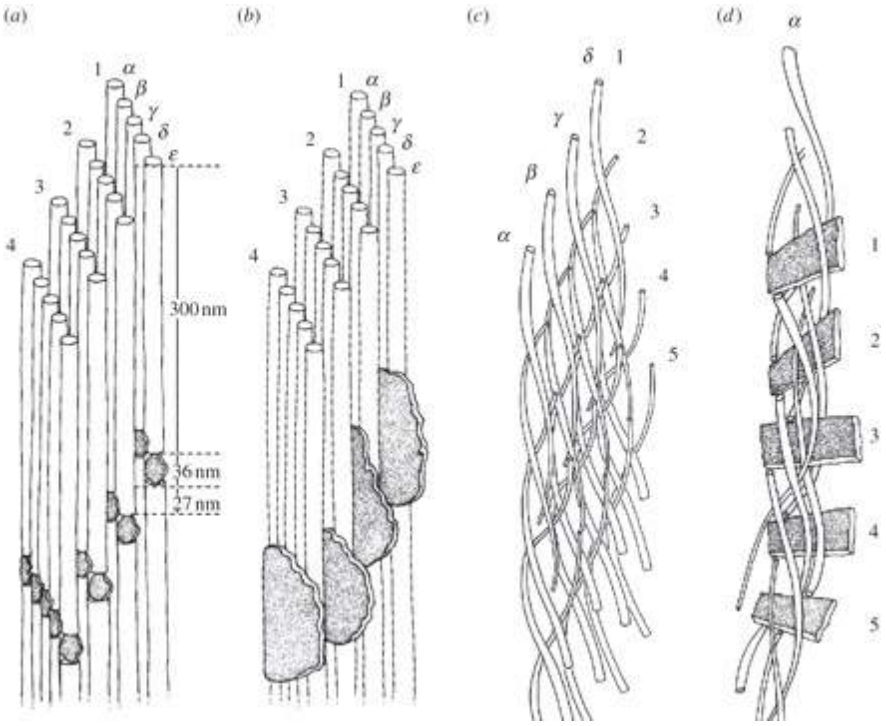

Figure 2.4: The models of collagen-mineral fibril organisation proposed by Orgel et al. (1963). Adapted from [19]

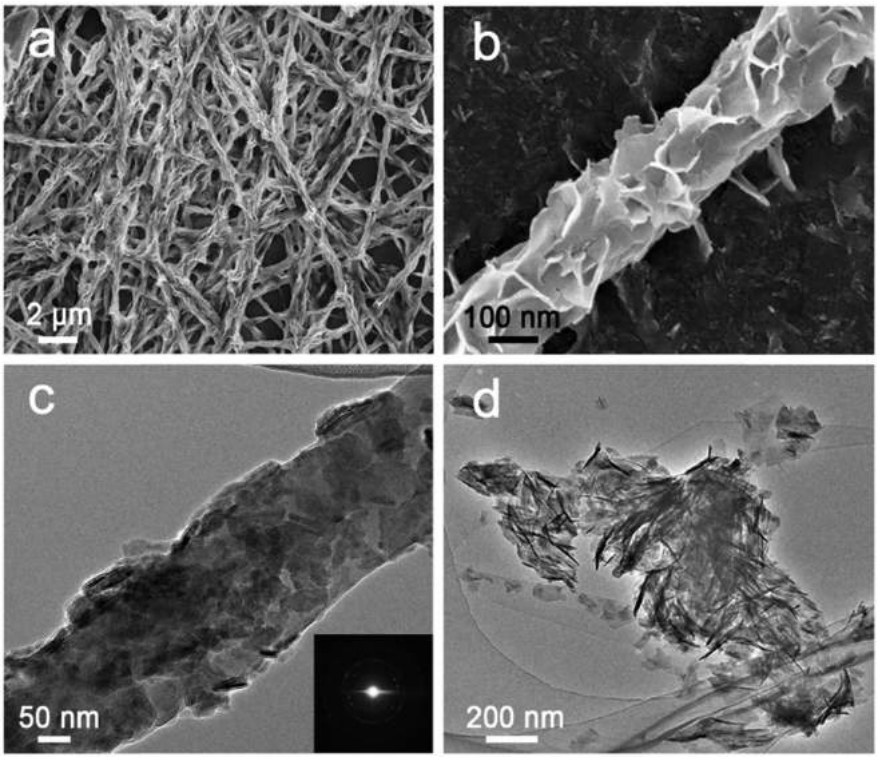

Figure 2.5: Electron microscopy images of mineralized collagen fibrils. (a) Low and (b) high magnification of SEM images of mineralized collagen fibrils, (c) TEM image of an isolated collagen fibril and (d) TEM image of mineral crystals. Adapted from [23]

2.2 Structure of the osteon

This thesis will take a closer look into osteonal bone organization. In particular, the mechanical and structural properties of individual osteons will be investigated. The osteon is a cylindrical, onion-like structure composed of a central Haversian canal housing blood, nerve and lymph vessels, which is surrounded by alternating mineralized collagen lamellae (Figure 2.6). René van Oers et al. (2008) reported the average osteon diameter to vary within 150 – 350 μm [24]. The Haversian canal diameter in diaphyseal compact bone has been found to

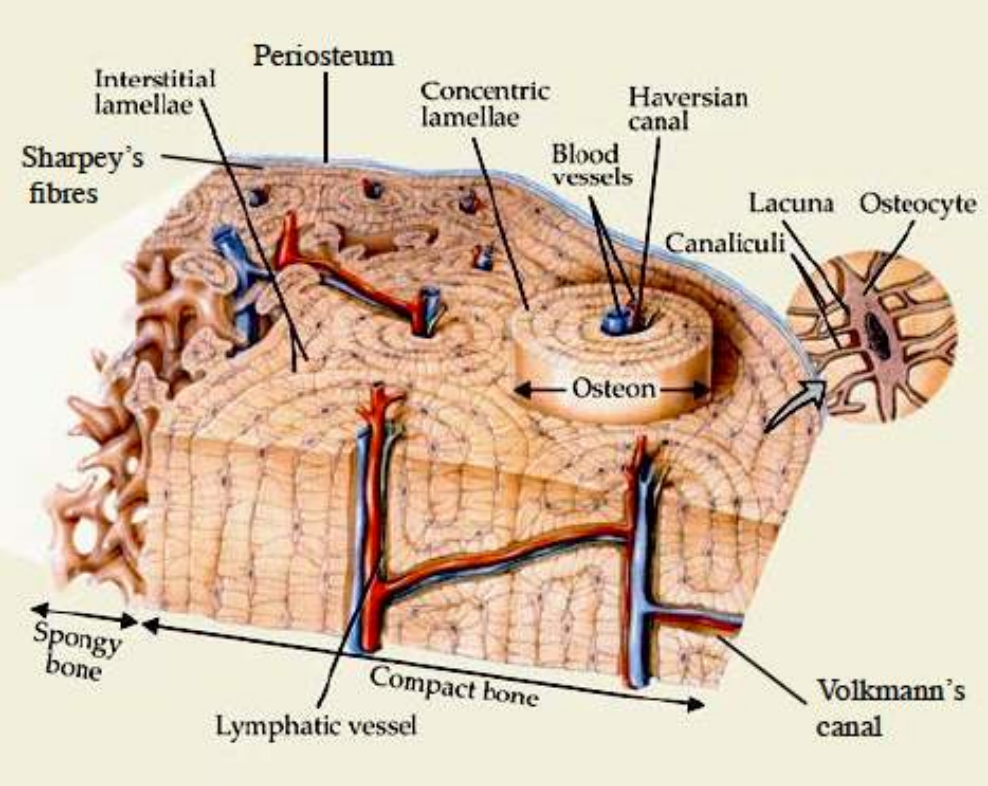

Figure 2.6: Structure of the osteonal bone. Adapted from "Tissue biomechanics" lecture notes, Thurner 2016

be approximately 68.8 μm [25]. Haversian canals of individual osteons interconnect with each other by the smaller in diameter Volkmann's canals. Volkmann's canals run transverse to the diaphyseal axis, providing a radial path for blood flow within the bone. Between the lamellae small ellipsoidal holes (4 to 22 μm diameter) called lacunae are present [26]. In these spaces bone cells, Osteocytes, reside surrounded by a thin layer of extracellular fluid. Osteocytes have long dendritic extentions that extend from the cell through tiny channels called canaliculi, contributing to the lower-scale porosity of cortical bone.

Structural organisation of the osteonal lamellae remains a subject of debate. Two principal hypotheses exist concerning the structural composition of the osteonal lamellae. The first one is based on the assumption that one lamellae layer is different from another due to the change in orientation of the mineralised collagen fibres. The second hypothesis explains this difference by the changing relative densities of the elementary components in the lamellae layers, in particular by the change in collagen density.

The first hypothesis was proposed by Gebhardt in 1906 [27] and was adapted by Ascenzi et al. in the late 1960s, suggesting that the mineralised collagen fibres within one lamellae layer are predominantly parallel and the orientation of the mineralised collagen fibres can change up to 90 degrees in the adjacent lamellae layers. Based on this, osteons were classified into 3 structural types: transversal, alternate and longitudinal (Figure 2.7). Cross-sections of transversal osteons appeared light under a polarising light microscope due to the transverse orientation of collagen fibre bundles, relative to the long axis of the Haversian canal, in successive lamellae (Figure 2.7a). Cross-sections of alternate osteons appeared grey under the microscope due to near cross-ply orientation of the collagen fibre bundles in adjacent lamella, i.e. fibres oriented at approximately 0° and 90° in adjacent layers (Figure 2.7b). Cross-sections of longitudinal osteons appeared dark under the microscope due to longitudinal orientation of fibre bundles in successive lamellae (Figure 2.7b).

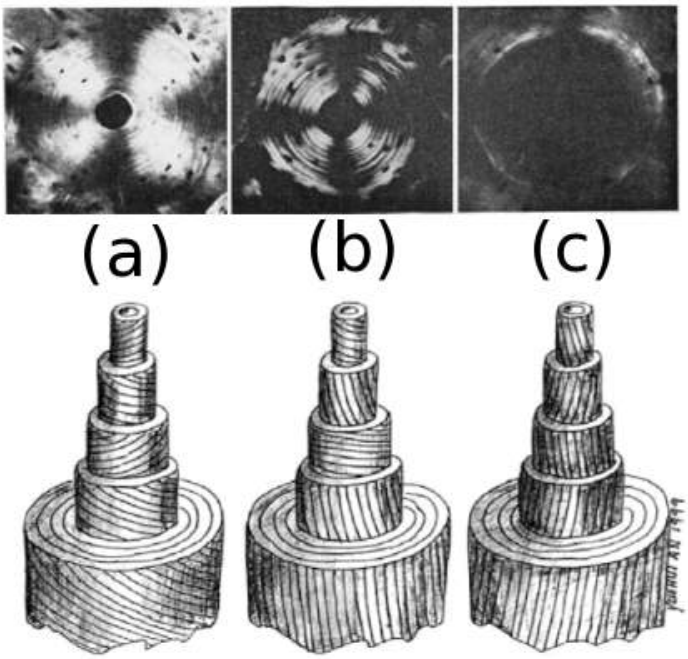

Figure 2.7: The three types of osteons roposed by Ascenzi et al. (1968), (a) transversal, (b) alternate and (c) longitudinal, under a polarizing light microscope (Top) with corresponding diagrams illustrating the orientation of fibre bundles in successive lamellae (Bottom). Adapted from [28] and [1]

A new theory of collagen fibril orientation in successive lamellae was presented by Giraud-Guille in 1988 [29]. Based on the analysis of transmission electron microscopy images of decalcified human cortical bone sections, orthogonal and twisted plywood models were suggested, as shown in Figure 2.8.

In the twisted plywood model parallel collagen fibrils are continuously rotated by an angle from 0 to 45 degrees within each lamella. The twisted plywood model was regarded as an analogy of the alternating type of osteon proposed by Ascenzi. Another schematic of the twisted plywood model is shown in Figure 2.9. The orthogonal plywood model consisted of collagen fibrils which were parallel within one lamella, but, unlike the twisted plywood fibrils, did not rotate. Orthogonal osteon organisation resembled the combination of Ascenzi's longitudional and

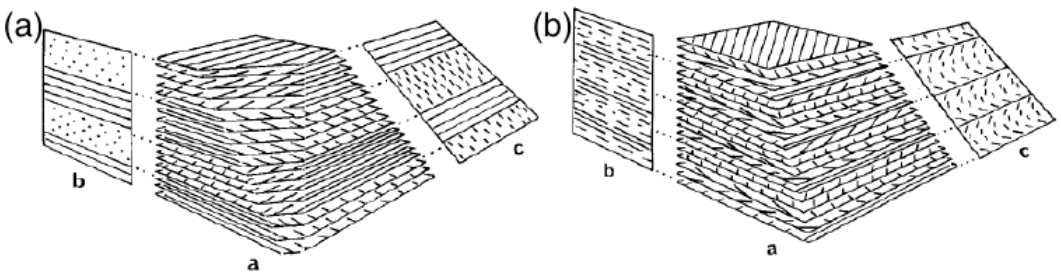

Figure 2.8: The two types of osteons roposed by Giraud-Guille (1988), (a) orphogonal and (b) twisted. Adapted from [29]

transverse osteons.

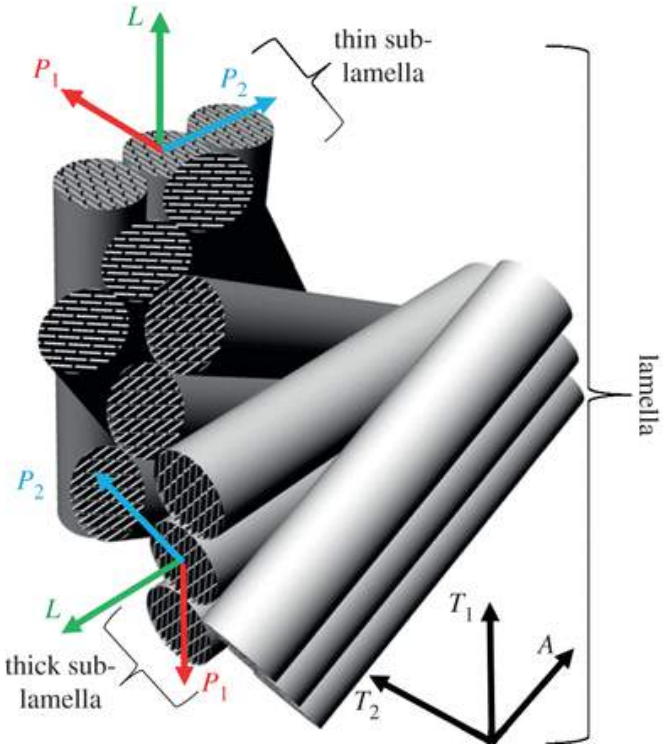

Figure 2.9: The twisted plywood model. Adapted from [30]

The second hyposesis of collagen lamellar organisation was proposed by Marotti and Muglia in 1988 was further adapted by Weiner et al. (1997) [30] and Wagermaier et al. (2006) [31]. This hypothesis stated that collagen fibrils within one lamellae were not parallel to each other but instead had random orientations [32]. The alternating dark and light patterns observed by polarized light microscopy were explained to be a result of different relative densities of collagen. Marotti and Muglia (1988) defined lamellae as densely and loosely packed collagen fibrils. The "bright" lamellae corresponded to the loosely packed collagen fibrils while the "dark" lamellae attributed to the densely packed collagen fibrils.

In more recent research, organisation of mineralised collagen fibrils within the osteon remains a subject of discussion. As an example, the oscillating plywood model with three distinct motifs was developed as yet another interpretation of the twisted plywood model. An overview of all the existing models is given in

the work of Mitchell et al. (2016) [33]. They summarised the existing models of lamellae organisation in one image, presented in Figure 2.10.

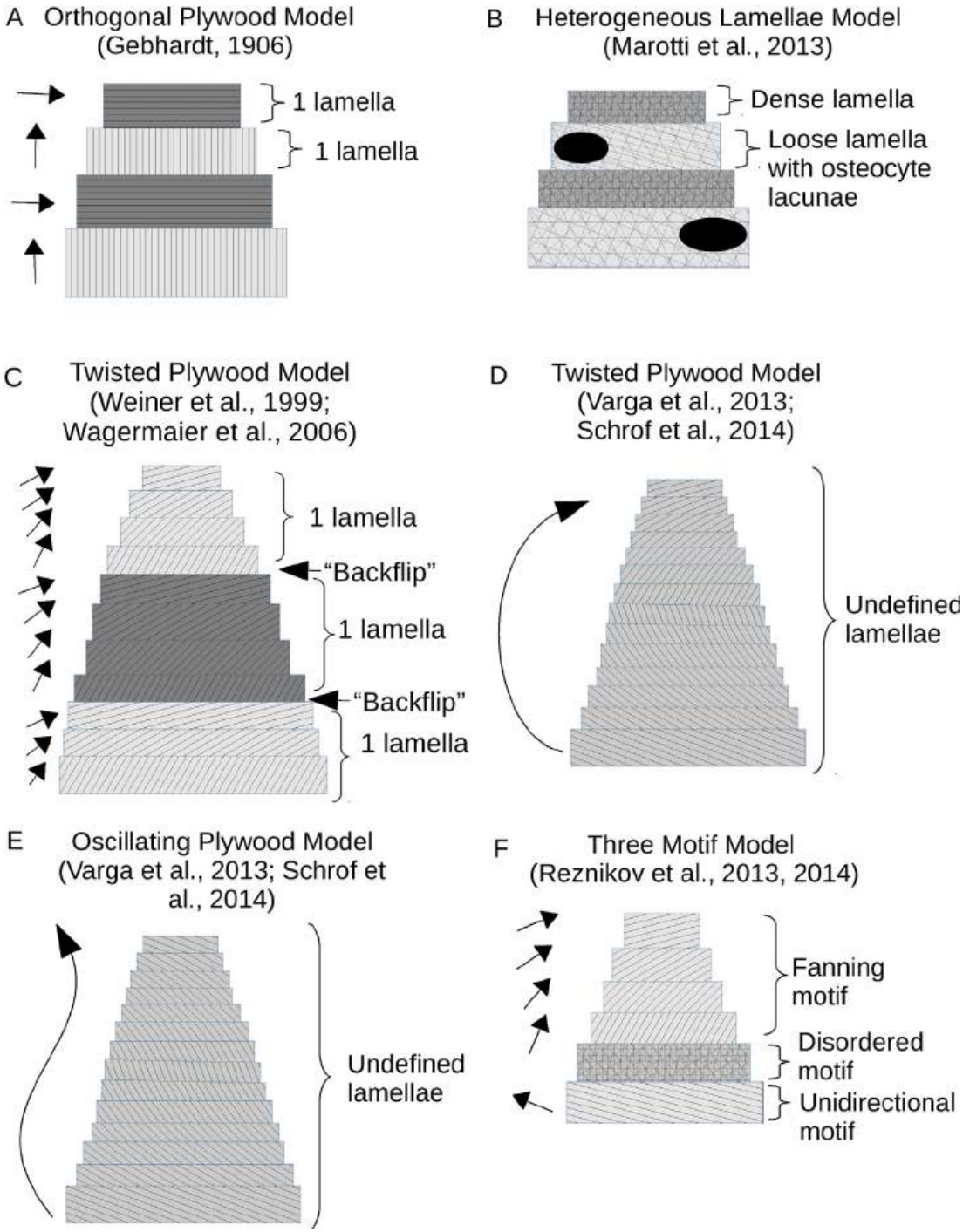

Figure 2.10: The summary of the existing models of lamellae organisation. Adapted from [33]

2.3 Formation of the osteon

As bone is a dynamic living tissue, osteons are continually being resorbed and newly formed by the bone remodeling process. The secondary osteon is a result of these processes. Remodelling initiates within the Haversian canal in response to changes in both mechanical and biochemical stimuli. Three main types of bone cells are involved in the process of bone remodelling: osteocytes, osteoclasts and osteoblasts. The aforementioned osteocytes are believed to act as mechanosensors [34]. They sense and trigger a regulated response to mechanical and chemical signals from their surrounding environment in order to promote either bone resorption or formation [34]. Osteocytes initiate bone remodelling via activation of two effector cells (osteoblasts, osteoclasts), which act together as a bone remodeling unit (Figure 2.11). Osteoclasts resorb bone while osteoblasts form new, unmineralised bone matrix. The cyclic process of remodelling is essential for skeletal growth and comprises four phases: resorption, reversal, formation and a resting phase. The resorption phase in healthy bone is a fast process taking from 7 to 10 days, whereas formation lasts longer (up to 2-3 months) [35]. The total surface of cortical bone is estimated to be completely remodelled over a period of 2 years [36]. The rate of bone turnover, however, is influenced by a number of parameters, including mechanical stimuli and systemic hormones [37].

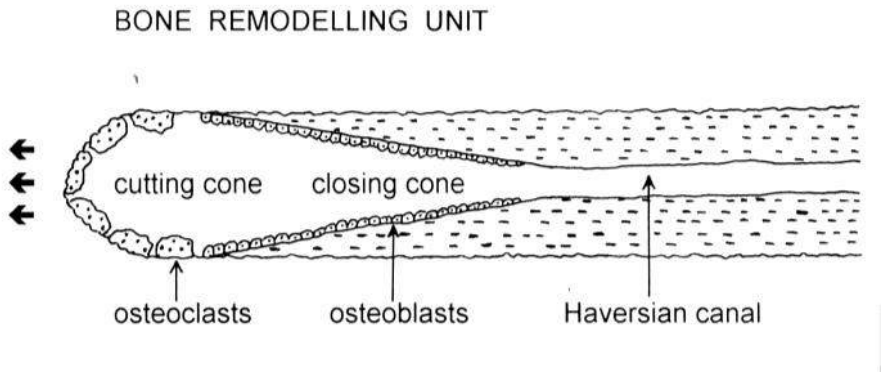

Figure 2.11: Osteoclasts cut through the surrounding material at the front of the developing osteon while osteocytes fill in the void around the vessels within the Haversian canal. Adapted from [38]

2.4 The change of osteon morphology with age

Secondary osteons show distinctive morphological heterogeneity that depends on the age of the individual, skeletal site and presence or absence of systemic factors that can alter the bone tissue [39]. The relationship between osteonal geometry and age is a subject of ongoing research. An overview of the morphological changes observed in osteons are given below and schematically represented in Figure 2.12:

- The cross-sectional area and diameter of the osteon decrease with age, but the circularity increases [40], [41].
- Young osteons are reported to have thicker osteonal walls with a higher number of lamella sheets [42].
- The density of osteons in cortical bone increases with age [43].
- Young individuals displayed higher numbers of osteocyte lacunae per osteon [40].
- The Haversian canal size is reported to be inversely affected by weight [44].

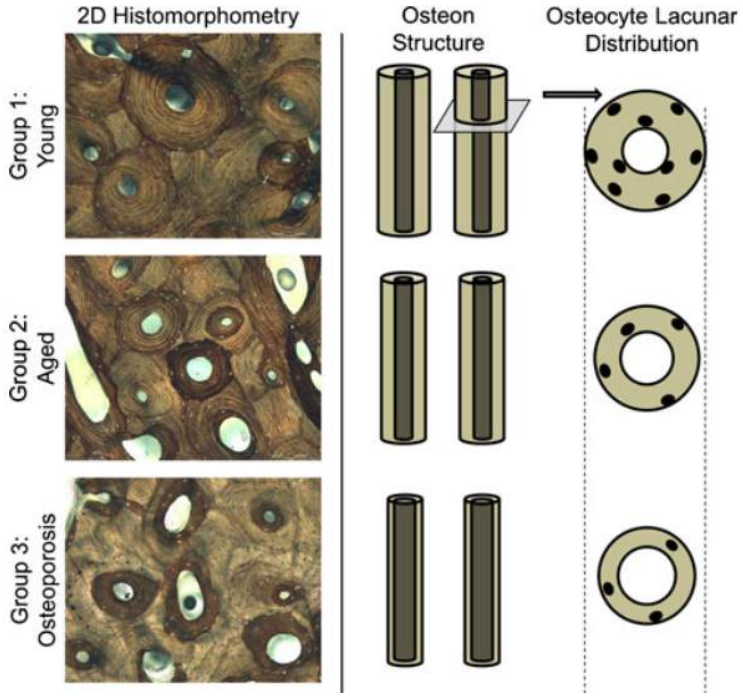

Figure 2.12: Representative microscope images and schematics highlighting the differences in osteon structure and osteocyte lacunar distribution between cortical bone of young (Top), aged (Middle) and osteoporotic (Bottom) women. Adapted from [40]

With morphological changes occurring at the micrometer-scale and mechanical properties of bone at the macro-scale tending to deteriorate with age, i.e. increased fragility, decreased fracture toughness, and a loss in total mass, there appears to be an interdependence between micrometer scale changes in osteon morphology and the mechanical properties of bone. However, to bridge the responses of bone at these two length scales mechanical properties of osteons should be first understood.

2.5 Mechanical properties of the osteon

Osteons are tightly packed within cortical bone. The border between individual osteons, in addition to the border between osteons and interstitial lamellae, is made up of an interface rich in mineral and non collagenous proteins. During fracture, osteons absorb energy and in healthy, tough bone the crack propagates through the mechanically weaker cement line, as shown in Figure 2.13. Osteons act as barriers to crack propagation, they perform a similar function as grains do in composite materials. The mechanisms of crack propagation seem to change with age. Recent studies have shown that the ability of osteons to withstand crack propagation substantially reduces with age; however, the underlying mechanisms of this phenomenon are not yet clear [45, 46].

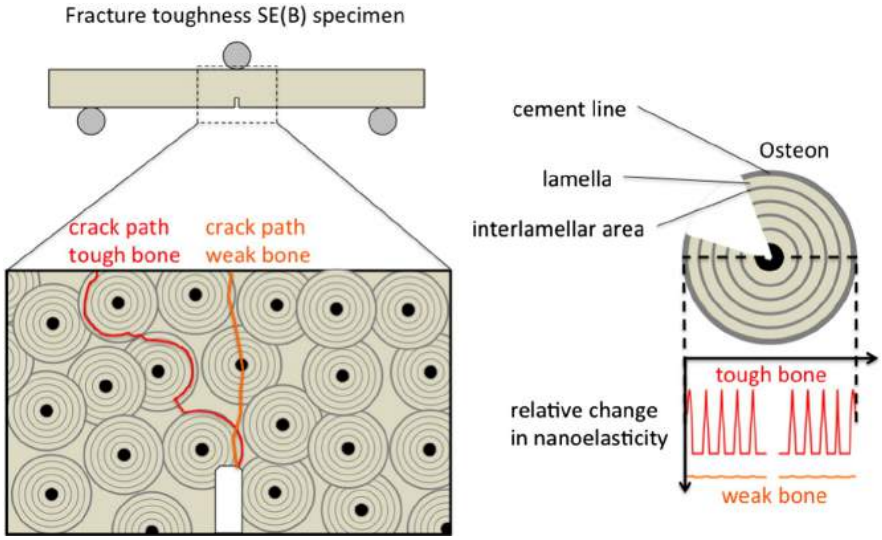

Figure 2.13: Schematic of putative crack propagation in young and elderly human cortical bone specimens. Adapted from [45]

To this day, studies conducted from 1964 to 1994 by Ascenzi et al. are the primary source of information on the structural and mechanical properties of individual secondary osteons [47]. In this series of studies, osteons were tested in compression, tension, bending and torsion. Elastic moduli of single osteons were reported to range from 1.6 to 9.3 GPa in compression [1], 2.6–11.7 GPa in tension [48] and 0.93–2.69 GPa in three-point bending [49]. The compressive elastic moduli were reported to change in correlation with mineral content and collagen fibre orientation of the osteons. As shown in Figure 2.14, osteons with transversely oriented collagen fibres exhibited a higher stiffness while longitudinal osteons produced a lower stiffness. Osteons at an initial stage of calcification showed higher ductility and lower stiffness.

The values of osteonal stiffness seem to be at odds with the values of bone stiffness at the macro scale. Secondary osteon stiffness appears to be less than that of large cortical bone specimens. It remains unclear what structure or mechanism in bone contributes to the overall higher stiffness of cortical bone. The elastic modulus of cortical bone is approximately 19-26 GPa [50], [51]. Cortical bone is the strongest in compression. When loaded in compression along its longitudinal axis, the maximum stress values are reported to be approximatly 180 MPa, whereas for tension and shear maximum stresses are reported as 120 and

60 MPa, respectively [51]. Due to its anisotropy, bone tends to fail more easily when loaded transversely or at an angle, as shown in Figure 2.15.

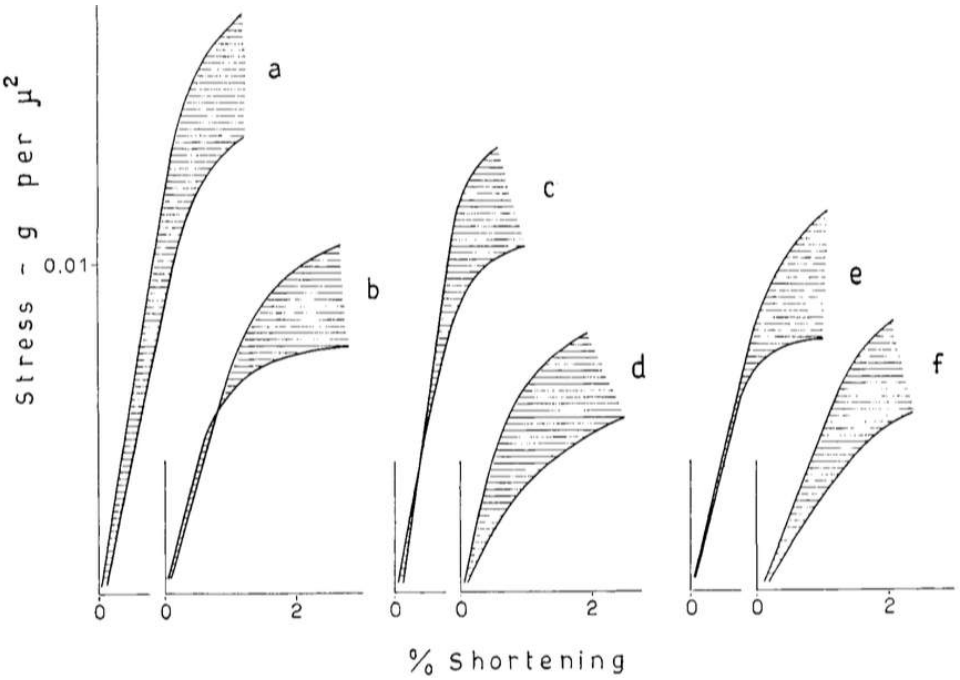

Figure 2.14: Stress-strain curves of (a) fully calcified transverse osteons with E=9.307 GPa; (b) initially calcified transverse osteons with E= 7.223 GPa; (c) fully calcified alternating osteons with E=8.375 GPa; (d) initially calcified alternating osteons with E= 3.296 GPa; (e) fully calcified longitudinal osteons with E=6.324 GPa and (f) initially calcified longitudinal osteons with E=4.811 GPa. Adapted from [1]

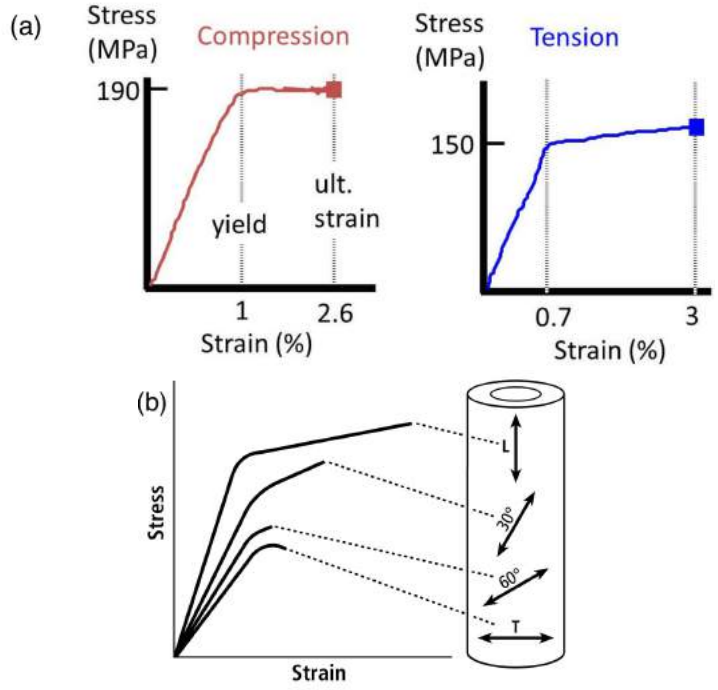

Figure 2.15: (a) Cortical bone in compression and tension. (b) Anisotropic behaviour of cortical bone in tension. Adapted from [52]

2.6 Fracture mechanisms and bone failure

Osteonal organisation of bone has a significant effect on macro-scale fracture toughness of bone. Bone fracture is characterised by dissipation of elastically stored energy from an applied load. Within the structure of cortical bone there are many compliant interfaces, such as cement lines which provide opportunities for energy dissipation and crack arrest. Toughening mechanisms are believed to be present in bone at each level of hierarchy, as shown in Figure 2.16.

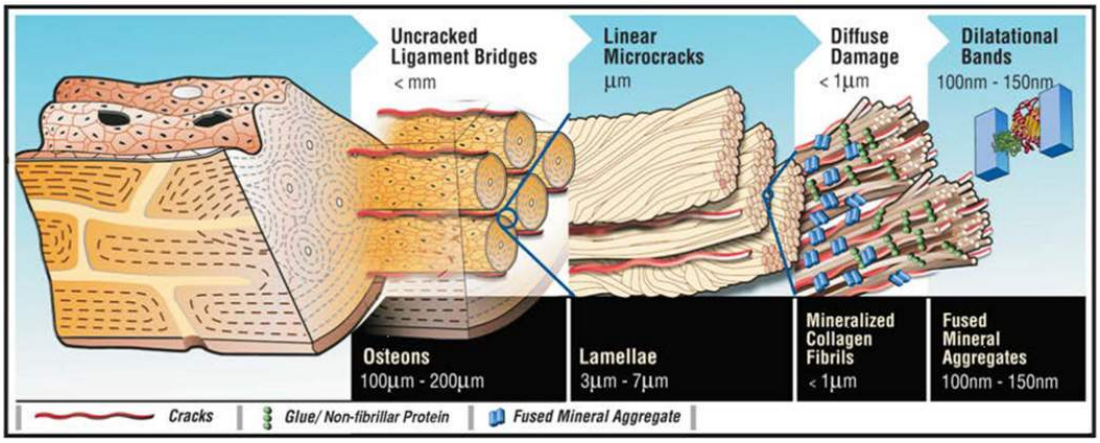

Figure 2.16: Hierarchy of fracture mechanisms. Adapted from [53]

At the osteonal level, toughness is a function of the path that a crack follows through the tissue. The toughening mechanisms at this level are crack deflection at cement lines and uncracked ligament bridging. The uncracked ligaments are formed across the faces of the crack, which results in crack bridging and retardation of fracture propagation. The crack deflection and ligament bridges are shown in Figure 2.17.

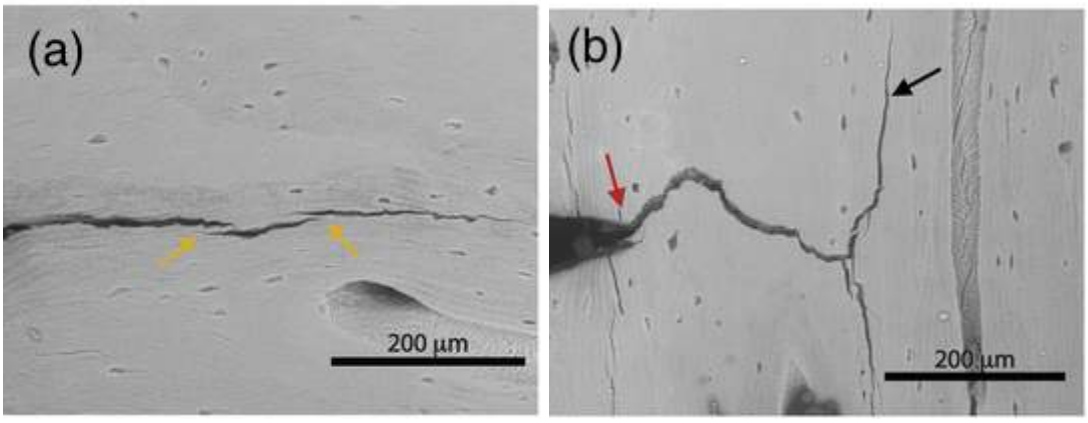

Figure 2.17: SEM images of (a) uncracked ligament bridging and (b) crack deflection mechanisms. Adapted from [12]

At the lower levels of single lamellae and single mineralised collagen fibrils, there are two types of micro-damage, namely microcracks and diffuse damage. Microcracks occur in both cortical and trabecular bone when the tissue is loaded in the post-yield region. Microcracks propagate along the lamellae interfaces and are believed to induce bone remodelling [54]. Furthermore, microcracks have

been shown to initiate in interstitial bone. Interestingly osteons do not always act as barriers to microcrack propagation, but may actually act as a weakness and accelerate the propagation when microcracks are long enough [55]. The propagation of a microcrack through an osteon is shown in Figure 2.18b.

Diffuse damage is characterized by a pool of sub-micron cracks over a certain area, as shown in Figure 2.18c. These sub-micron cracks separate mineral aggregates from each other and from the surrounding organic matrix. Creation of a large surface area of sub-micron cracks dissipates energy that would otherwise result in linear microcrack growth and propagation. Recent research suggests that there might be important biological responses to diffuse damage, which are completely distinct from the response to linear microdamage [56]. Overall, diffuse damage shows more ductile behaviour, while microckrack fracture exhibits the features of a brittle fracture.

Notably, the ability of bone to form diffuse damage diminishes with age. [53]. As it was mentioned in section 2.4, the average size of an osteon decreases in older bone but the number of osteons increases. This leads to an increased amount of interstitial bone within older bone. Since the interstitial bone is harder, stiffer and, hence, more brittle than osteonal bone [57], the increased fragility of older bone can be explained by predominant formation of brittle microcracks that are more likely to develop into catastrophic bone fractures. However, mechanistic understanding of the changing fracture behaviour of aging bone is lacking.

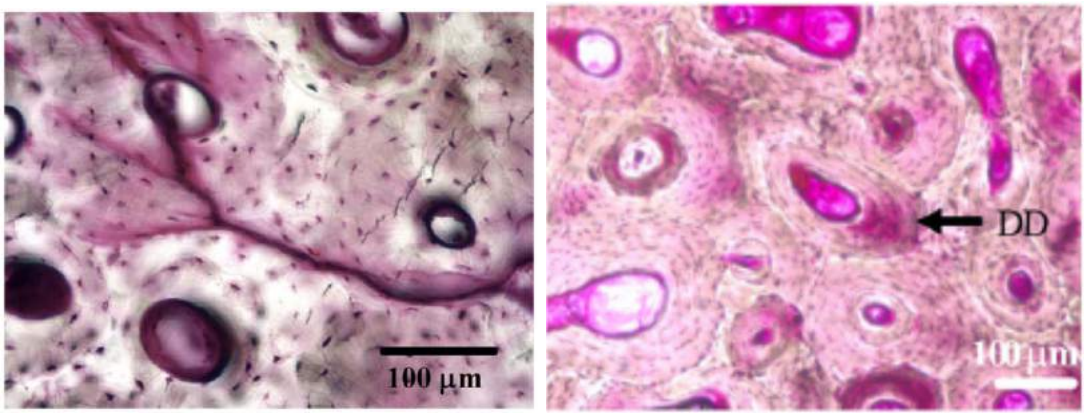

Figure 2.18: Light microscopy images of (a) a linear microcrack and (b) diffuse damage. Adapted from [58]

At the level of bone's nanostructure, the initiation of fracture is believed to occur in form of dilatational bands. Noncollageneous proteins play a major role in fracture formation at this level. Osteocalcin (OC) and osteopontin (OPN) proteins link mineral and non-mineral components of bone. OC binds strongly to hydroxyapatite and it complexes with and links to collagen through OPN. In the model hypothesised by Poundarik et al. (2012) continuous nano-scale tensile loading of OC and OPN results in inelastic deformation of the protein complexes; thus, dilatational bands are formed [59]. Subsequent loading of the dilatational bands will cause shearing and rupture of the mineralized collagen fibrils and result in the formation of diffuse damage. OC-OPN protein complexes are, therefore, believed to contribute to the fracture toughness of bone [60].

2.7 Isolation of osteons

Several approaches for single osteon isolation have been developed over the recent years. The first major works dedicated to developing osteon isolation techniques was done by Ascenzi et al. in the late 1960s [1, 61]. Two experimental techniques were developed by Ascenzi's group and special micro-instrumentation was designed for the both techniques.

With the first technique developed in 1968, osteons were isolated for further compression testing [1]. The cross-sections of bone were cut transversely to the Haversian canal's general direction. The prepared cross-sections were then fixed on the stage of the microscope where the hand-piece of a dentist's drill substituted the microscope's tube. This setup is shown in Figure 2.19. A thin steel needle inserted into a dental drill was used as a drill-bit to mill out the desired osteons. The position of the dentist's drill above the fixed bone cross-section was regulated manually by the coarse adjustment and visually controlled with a stereoscopic microscope. As the dental drill rotated, the eccentric needle drill-bit made a circular cut around the targeted osteon throughout the bone cross-section (Figure 2.20).

The second of Ascenzi's osteon isolation techniques was developed in 1994, the produced osteons had lugs on both ends and were used in mechanical torsion testing. Longitudinal sections, slightly thicker than osteon diameter were cut from the bone. Circularly polarized light microscopy was used to select an osteon to mill out. A box shaped sample was cut out of the longitudinal bone section with the dental drill setup. A micro-grinding lathe was then used to make the middle portion of the sample cylindrical. A schematic representation of the steps of the second osteon isolation technique is shown in Figure 2.21.

Besides the Ascenzi et. al techniques, one more approach for osteon isolation was described in recent studies. Frasca, Harper and Katz et al. were able to isolate whole osteons from the cross-sections of bone by propagating fractures along their natural boundaries [62]. Using the diference in mechanical properties of the osteon and its surrounding tissue, whole osteons were isolated with lengths ranging from approximately 0.1 to 2 cm.

With the third, Frasca's, technique, it was possible to isolate osteons in their original physiological shape. However, the irregular geometrical shape of the osteons made it difficult to use conventional micro-mechanical testing techniques. In Ascenzi's methods, the assumption was made that the produced cylindrical samples with an Haversian canal along the central longitudonal axis represented the osteon structure. The advantage of Ascenzi's techniques was that the produced osteons had the same geometrical shape and, therefore, micro-mechanical testing on these samples produced results that were possible to compare and analyse.

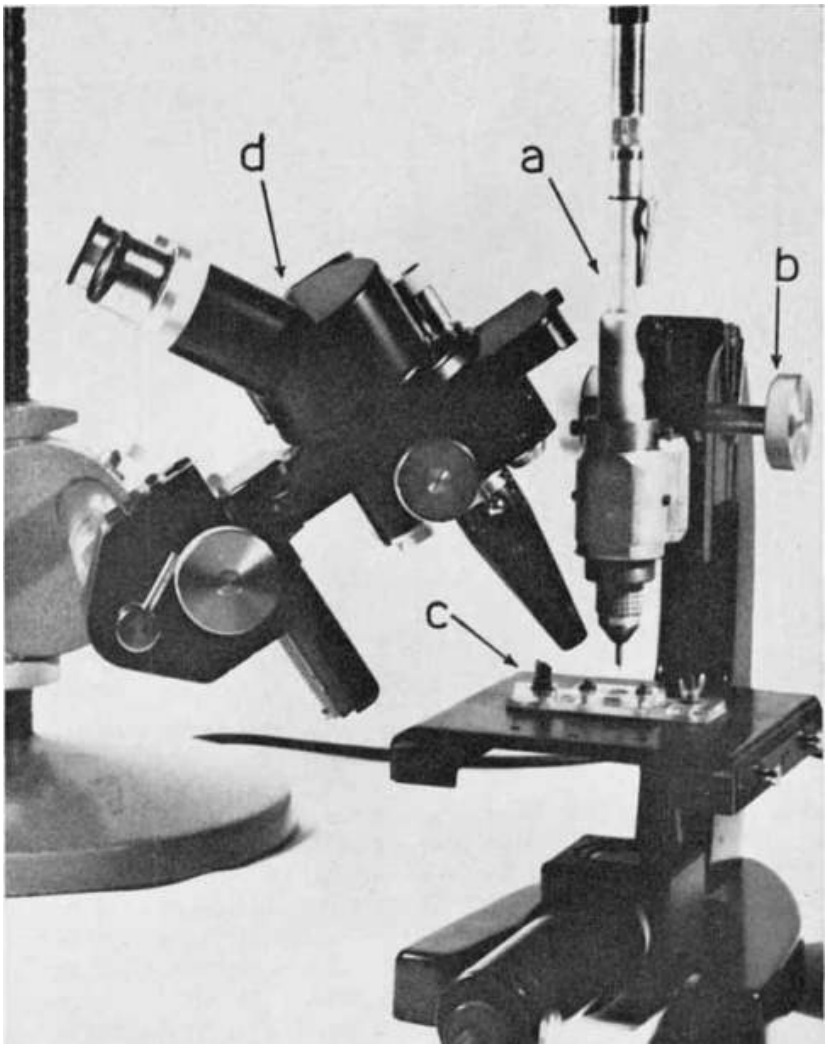

Figure 2.19: A photograph of the setup to isolate single osteons for compression testing developed by Ascenzi et al. in 1968. (a) The hand-piece of a dentist's drill, (b) the coarse adjustment, (c) the microscope stage and (d) the stereoscopic microscope. Adapted from [1]

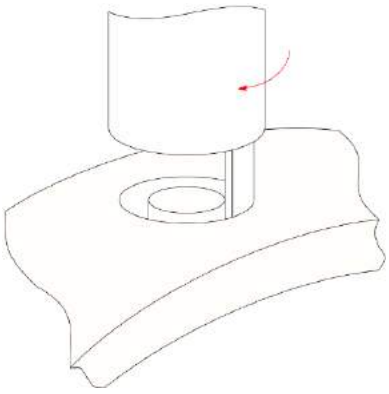

Figure 2.20: A schematic representation of a circular cut performed by the eccentric drill-bit throughout the bone cross-section to isolate a single osteon in the first technique developed by Ascenzi et al. in 1968

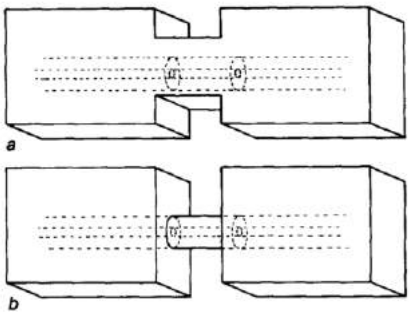

Figure 2.21: A schematic representation of the osteon isolation developed by Ascenzi et al. in 1994. (a) The sample was cut by the dental drill and then (b) the sample was ground with the micro-grinding lathe. Adapted from [61]

Chapter 3

Development of methods for isolation and compression testing of individual osteons

3.1 Introduction

As computational modelling becomes an increasingly common tool to predict mechanical behaviour of bone, the need to collect the experimental data for refinement and validation of such models also grows. However, the limited number of investigation tools remains a main challenge for experimental biomechanics research. As bone is a hierarchical material, sample preparation becomes increasingly difficult. At a micrometer scale, trabecular bone consists of individual trabeculae and cortical bone is comprised of tightly packed individual osteons. Small size, dense osteon arrangement and irregularity in shapes of individual osteons makes it difficult to extract single osteons from the bulk material of bone.

In the late 1960s, Ascenzi et al. successfully isolated osteons from the cross-sections of bone with a modified dental drill, where an eccentric needle tool was installed and used as a drill bit. However, manual operation of the dental drill made it difficult to automate the procedure for future research. In 2006, Nyman et al. described a similar milling procedure using an eccentric drilling tool. A CNC-system was modified to house a camera-microscope. Then, a region of interest was identified with the camera-microscope and the bone cross-section was moved under the eccentric drill-bit. The produced osteons were then used to evaluate the concentration of collagen crosslinks. The research of Nyman et al. showed that it was possible to effectively isolate single osteon from bone cross-sections with a modified CNC-system and an eccentric coring tool.

Micro-mechanical compression testing of individual osteons were first performed by Ascenzi et al. (1968) and not repeated afterwards. In Ascenzi's work, samples were tested in continuous uni-axial compression in a micro-compressor with a microwave micrometer based in the cavity. Displacements were deduced from the changes of the resonant frequency of the cavity. The existent knowledge of oteonal mechanical properties is greatly based on this research. At present, a number of mechanical testers have been developed that allow for a more precise and reliable measurement of the force-deflection data in comparison to mechanical testers used in the 1960s.

With technological progress, the need to re-establish a methodology for isolation and compression testing of individual osteons became apparent.

In this thesis, a new osteon isolation procedure was developed which can be performed by an operator without extensive training and allows for a greater automation of the process. The described concepts of a modified CNC-system and an eccentric coring tool were used to design the new osteon isolation procedure. For the design of the mechanical testing setup, a static load frame was used. The high stiffness of the system and its highly precise servo-electric linear motors allowed for high reliability of the data. With a number of conducted experiments, the developed methotology was optimised. Detailed information on the produced osteons, mechanical testing and improvements of the developed procedure can be found in Appendix A.

In this chapter, the established osteon isolation procedure and the designed mechanical testing setup are described, in addition to the approaches used to evaluate the morphology of the osteons and interpret the results of compression testing.

3.2 Research objectives

- Develop an osteon isolation method,
- Develop a compression testing set-up,
- Establish a methodology for assessment of osteonal mechanical properties for direct comparison of the values with the ones reported by Ascenzi et al..

3.3 Bone tissue

One ovine and one bovine femur were obtained and stored at -20 degrees Celsius (C). Two human femurs (male, aged 92 and 76) were obtained from the Anatomy Department of the Medical University of Vienna and stored at -80 C.

Using a band saw (Exact 300 CP, Norderstedt, Germany) and a low speed precision saw (IsoMet, Buehler, Lake Bluff, IL, USA) with diamond coated blades, a number of cross-sections with thickness ranging from 400 to 500 μm were cut from the midshaft of each femur (figure 3.1).

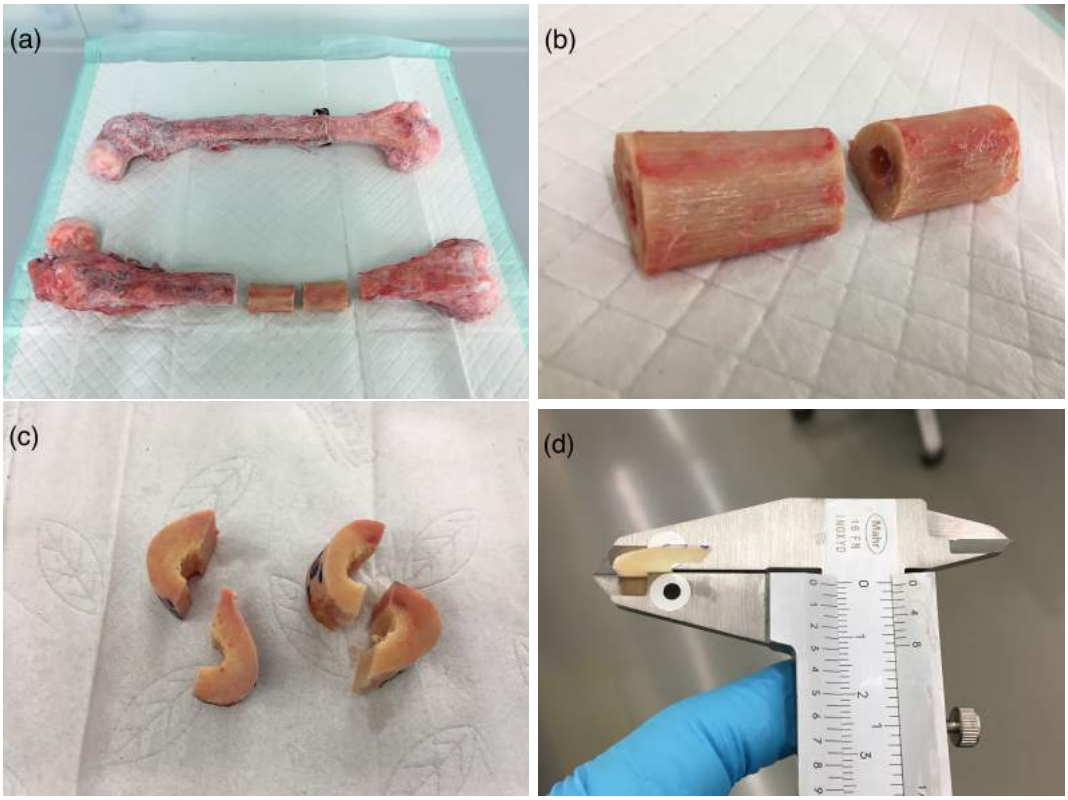

Figure 3.1: Preparation of the human bone cross-sections. (a) Femurs, (b) big bone slabs, (c) small bone slabs and (d) an individual bone cross-section

To make osteonal structures visible under the light microscope, the obtained cross-sections were then subjected to a hand-polishing procedure (Figure 3.2). The steps of the polishing procedure are listed below:

- Each cross section was firmly fixed on a plastic slide using superglue (Super Glue Liquid, Pattex, Germany).
- The free face of the cross-section was watered and brought into contact with the silicon carbide abrasive paper disc of grit size 1000. When holding the plastic slide in hand, the bone sample was slightly pressed and moved against the abrasive grinding paper disc. By moving the sample along the surface of the abrasive paper for 2-3 minutes the bottom surface of the bone sample was evenly ground.
- The second step was then repeated with the abrasive paper discs of grit size 1200 and 1500 for 5-6 and 9-12 minutes.

- The ground surface was inspected under the light microscope to ensure the even distribution of the grinding grooves. Otherwise, step three was repaeted until the desired surface quality was reached.
- Then, free abrasive of 3 μm particle size was applied on a cloth. The sample was pressed and moved alone the cloth with the abrasive particles for 14-15 minutes.
- To remove the abrasive particles from the surface of the cross-section, the sample was washed in an ultrasound bath.

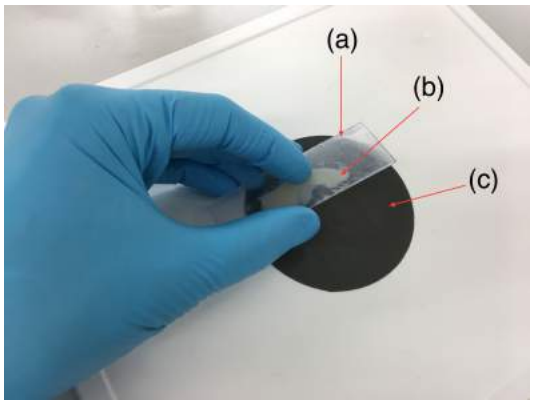

Figure 3.2: A bone cross-section is fixed on a plastic slide and is being polished. (a) Plastic slide, (b) bone cross-section and (c) silicon carbide abrasive paper disc

After the hand-polishing procedure, the cross-sections were affixed to a computer-numeric-control (CNC)-machine (BZT PFK-0203-PX, BZT Maschinenbau GmbH, Germany).

After each step of preparation big slabs of animal tissue were stored in the freezer at -20 C, while big slabs of human tissue were stored in the freezer at -80 C. The final sets of osteons were stored in vials with distilled water or Hanks Balanced Salt Solution (HBSS, pH 7.4) in the refrigerator at 0 C or in the freezer at -80 C. Further details on sample storage conditions are specified for each set of samples in sections 4 and 5.

3.4 Drilling tools

During the course of the project, 44 drilling tools were produced and tested. This includes:

- one dental centric drill bit,
- 6 eccentric drill bits produced during the Osteomill project,
- 6 centric drill bits produed by Robert Exler,
- 31 custom made eccentric drill bits.

Only the custom made eccentric drill bits were able to produce bone cylinders with diameter s of less than 400 μm. Therefore, the sets of cored out osteons subjected to mechanical testing were all machined using the custom eccentric drill bits.

3.4.1 Producing drill bits

Machining procedure

Commercially available stainless steel rods with diameter of 2 and 3 mm were used to produce eccentric coring tools. Machining of the tools were performed using an IsoMet low speed saw with a circular diamond blade, Figure 3.3. The steel rods were fixed on the support arm of the saw by a chuck clamp. Cutting was performed under constant water irrigation with positioning controlled via a manual micrometer.

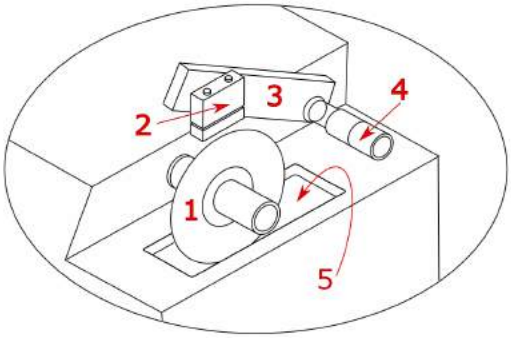

Figure 3.3: Schematic of the IsoMet low speed saw: 1) Circular diamond blade; 2) Chuck clamp; 3) Support arm; 4) Manual micrometer; 5) Water bath

The long steel rods were cut along the transverse plane (Figure 3.4a) into smaller bits with lengths of 3.5 - 4 cm. The produced bits were fixed in the chuck clamp such that a cut in the longitudinal plane of the rod could be made to a depth of 1 - 1.5 mm (Figure 3.4b). A number of cuts were then performed to form and refine the rectangular shape of the tip of the drill bit. Each cut is graphically represented in Figure 3.5.

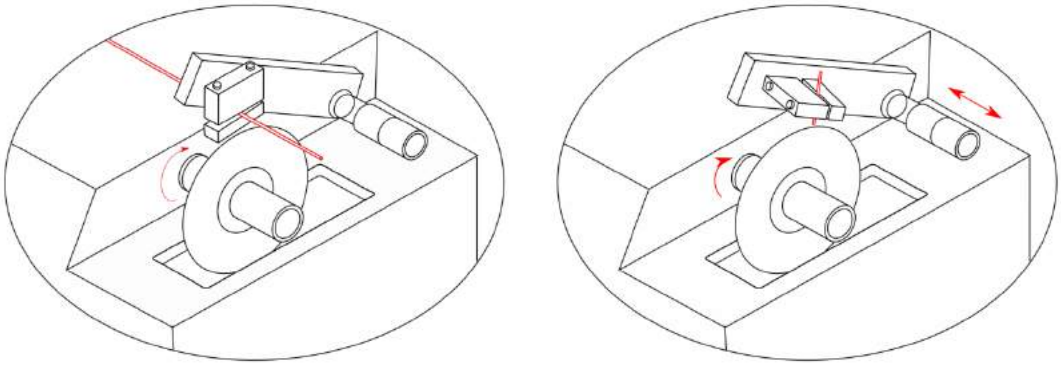

Figure 3.4: (a) A long steel rod clamped in the IsoMetTM low speed saw to cut along the transverse plane, (b) First longitudinal cut on a produced 3.5-4 mm steel bit

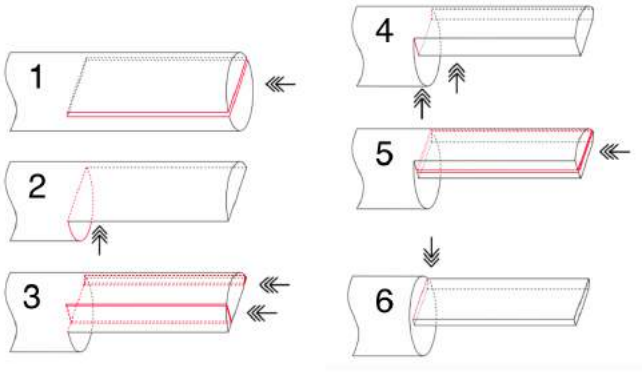

Figure 3.5: The cuts made on a steel bit by the diamond blade to form an eccentric drill bit

In the production of the drill bits, the first longitudinal cut defined the diameter of the cylinders that would be milled out by the drill bit. Therefore, particular attention was paid to the positioning accuracy of the steel bit above the diamond blade (Figure 3.6).

Precision of the manual micrometer of the IsoMet diamond saw is stated to be $\pm 5\ \mu m$. However, after extended use of the diamond saw and continued wear on the dimaond blade the whole "IsoMet" system (e.g. arm, clamp, blade) became less rigid. Therefore, the error of manual positioning was found to be $\pm 30\ \mu m$. The desired radius for the cylinders milled out by the produced drill bits was 100 μm (200 μm in diameter) which corresponds to the average radius of osteons in human cortical bone. Due to the insufficient precision of the first longitudinal cut, it was difficult to predict the diameter of the osteon that would be milled out by the produced drill bits. Therefore, 30 drill bits were produced with the same machining parameters and each one was tested on the CNC-machine to identify which diameter of osteon it could mill out. Out of 30 produced drill bits, 2 could mill out the desired osteon diameter of 200 μm.

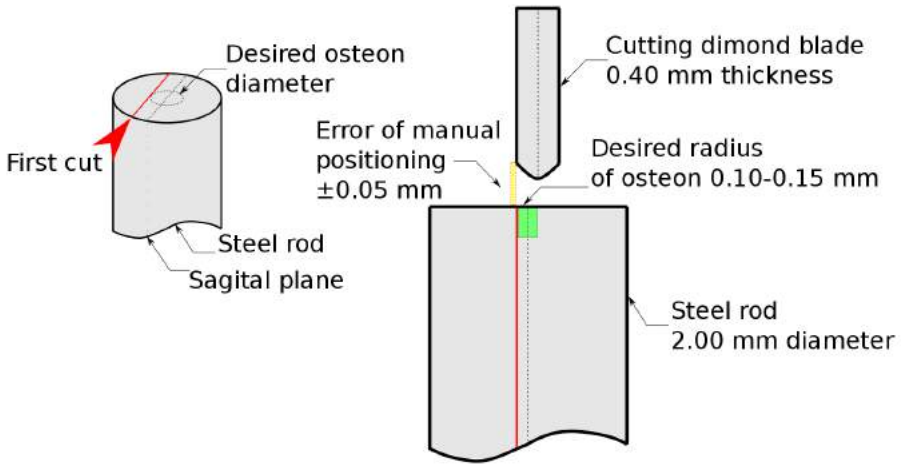

Figure 3.6: Inverted graphical representation of the manual positioning of the cutting diamond blade above the steel bit with corresponding precisions labelled

Sharpening procedure

During the coring procedure the drill bits were becoming blunt, which substantially influenced the quality of the harvested osteons. In Figure 3.7 a freshly made custom drill bit with sharp edges is presented. The drill bit in Figure 3.8 was used to mill out 10 osteons and the tip edges of the drill bit became blunt. No osteons could be cored out after $20 - 25$ harvesting procedures. Milling was performed at 7000 rpm with a plunge rate of 0.075 mm/min. Blunting of the tip of the drill bit resulted in the presence of a plate at the base of the milled cylinders after repeated use of the same drill bit. A sharpening procedure was developed and used at routine intervals to ensure the quality of the harvested osteons.

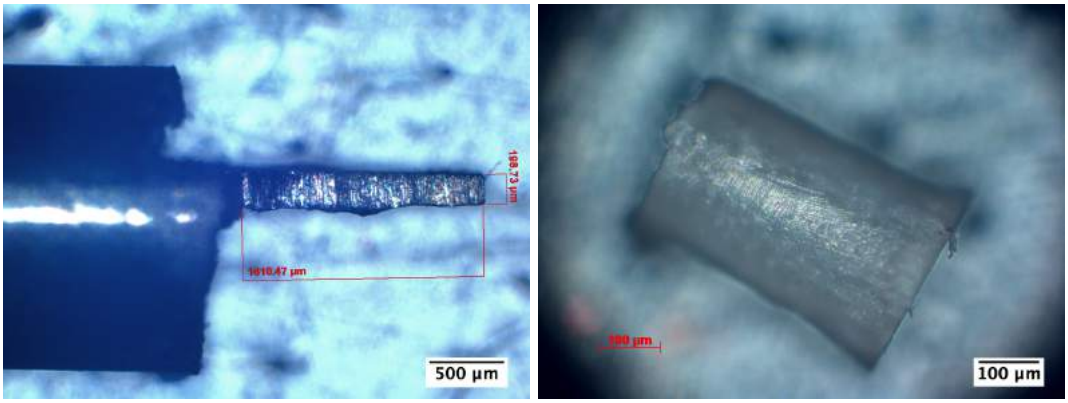

Figure 3.7: A sharp drill bit and the cylinder produced by it

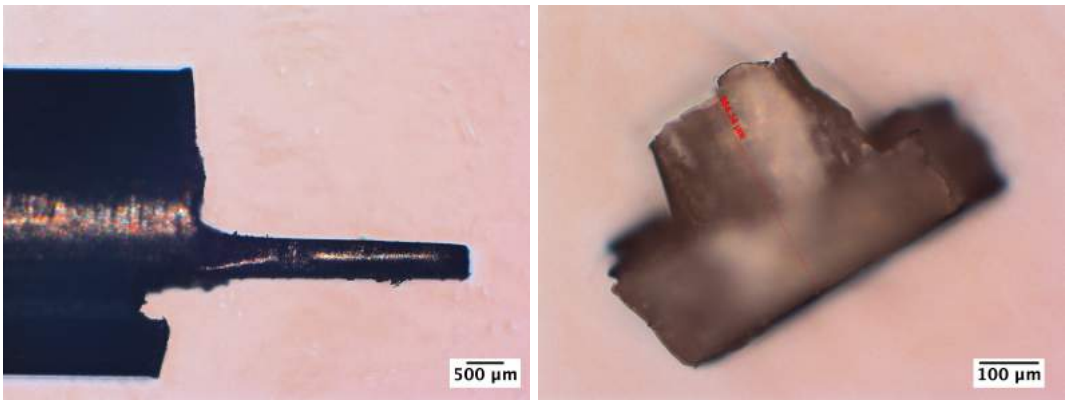

Figure 3.8: A blunt drill bit and the partially damaged cylinder with base-plate produced by it

In order to sharpen a worn-out edge, the drill-bit was clamped in the low speed saw with the blunt edge facing the side of the moving dimond blade (at the lowest speed possible) and gradually pressed into contact with the blade. Attention was paid to keep the surface of the drill bit edge parallel to the plane of the diamond blade (Figure 3.9).

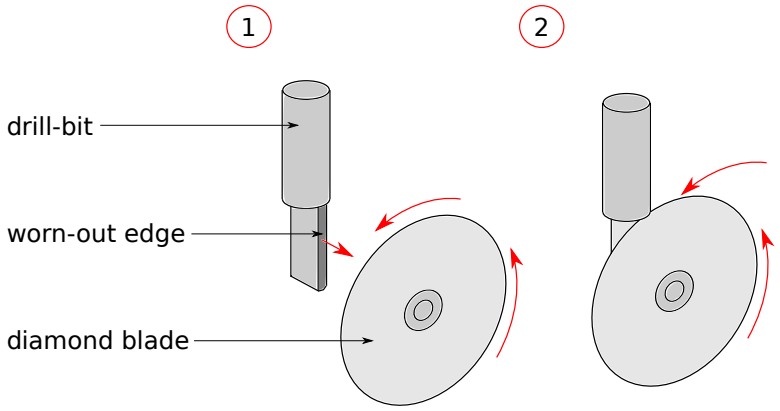

Figure 3.9: The two-step sharpening procedure of the drill-bit

3.5 Harvesting of osteons

3.5.1 Inspecting bone tissue

Three types of bone tissue were inspected in order to measure average osteon diameter. Due to the ellipticity and small diameter (less than $100\mu m$) of the ovine osteons, the ovine cross-sections were not used to harvest osteons for mechanical testing. The light microscopy images of the ovine, bovine and human osteon bone are shown in Figures 3.10, 3.11 and 3.12 with characteristic osteonal diameters indicated.

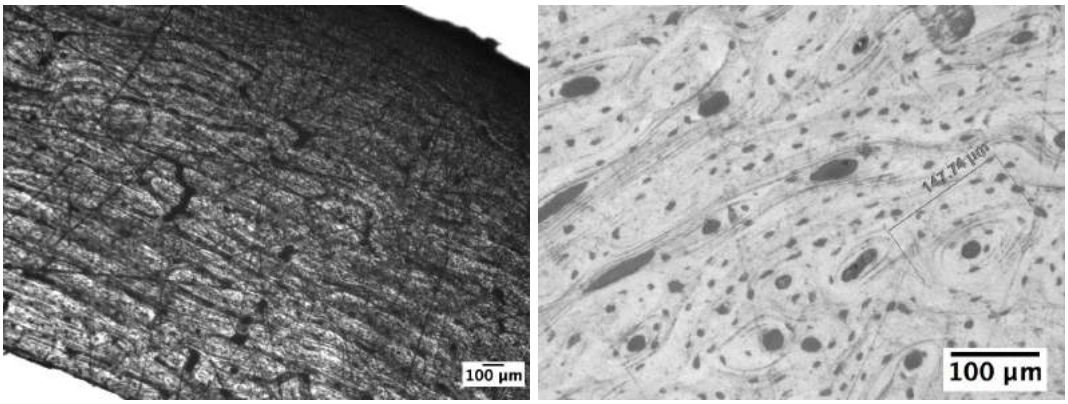

Figure 3.10: Ovine bone with osteon diameters ranging from 50 to 150 μm, average of 80 μm

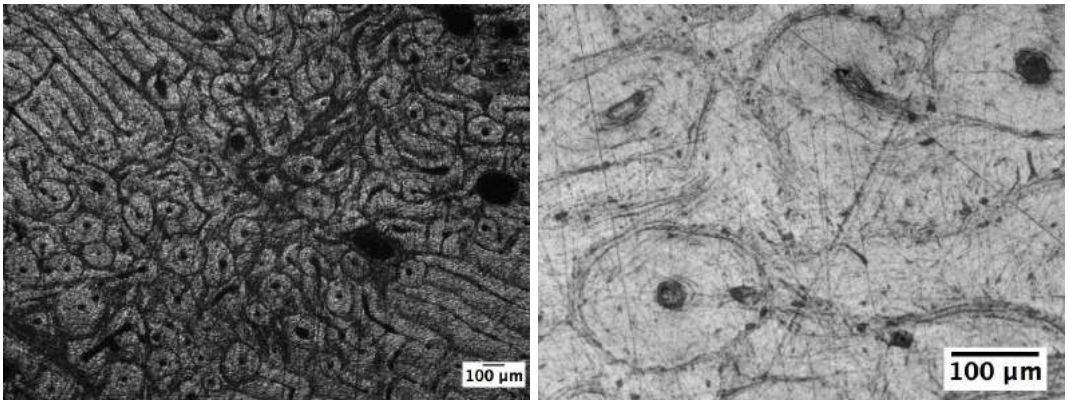

Figure 3.11: Bovine bone with osteon diameters ranging from 80 to 250 μm, average of 150 μm

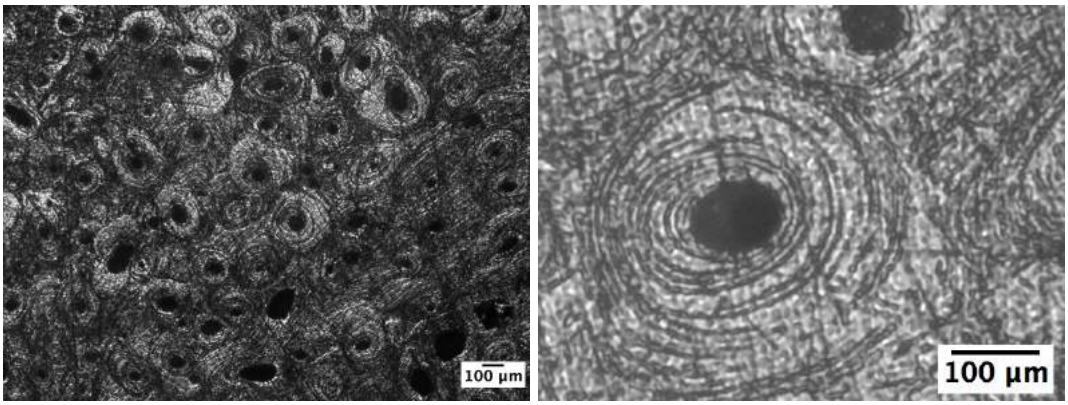

Figure 3.12: Human bone with osteon diameters ranging from 100 to 400 μm, average of 200 μm

3.5.2 Coring procedure

The bone sample was cored out using a CNC-machine. The cross-section of the femoral bone was immersed in a water bath, fixed by a custom clamping set-up to the 2-axis moving stage of the CNC-machine, and positioned under the drill. The entire set-up is shown in Figure 3.13. A camera (Mako U-130B USB 3.0, AlliedVision, USA) with an optical system (12X Zoom Lens System, Navitar, USA) was mounted to the CNC-machine in order to provide visual feedback for accurate positioning of the drill bit above the osteonal structures. The video feed was captured by MatLab software, which allowed micrometer-precise live positioning. Cross-hairs in the program window (Figure 3.14) were set at the centre of the captured osteon image, insuring that the centre of the osteon was aligned with the vertical axis of the camera. Positioning of the drill bit above the osteon was performed with 20 μm accuracy.

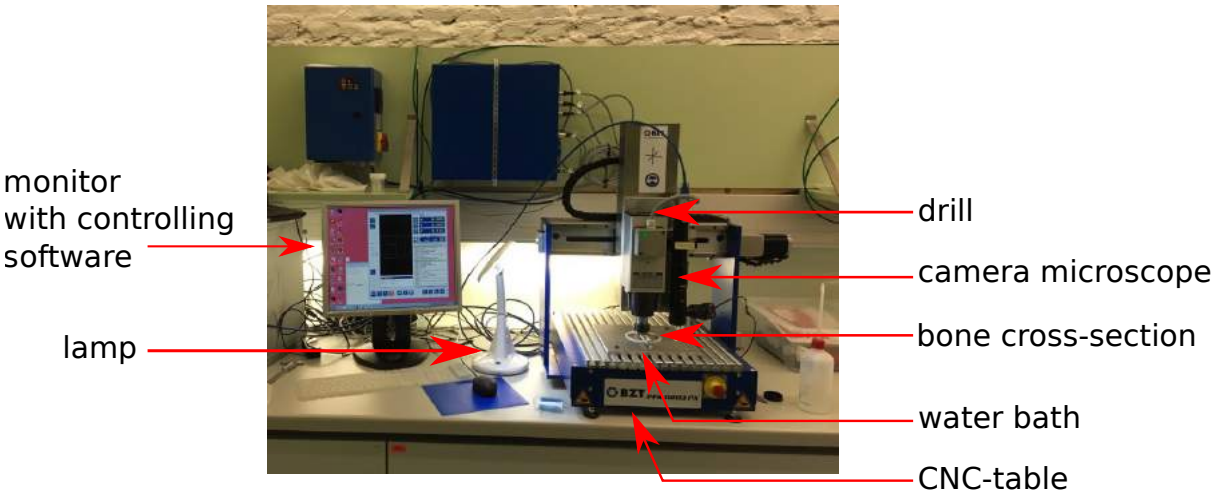

Figure 3.13: A photograph of the modified CNC-system

After the surface of the affixed cross-section was viewed through the microscope to identify a target osteon to harvest, the determined x- and y-coordinate off-sets of the camera position relative to the drill bit position were typed in the CNC-software (offset values determined from a calibration procedure are given in Section 3.5.3) and the target osteon was milled out following the steps described below:

Step 1 - Make contact with the dry surface of the cross-section using the tip of the drill bit, contact should be made at a distance from the target osteon, and set the Z-position to zero on the CNC-machine;

Step 2 - Re-positioning of the drill-bit above the target osteon using the cross-hairs and camera-to-drill bit x- and y-coordinate offsets. Set the x- and y-axis of the CNC-machine to zero;

Step 3 - Apply a drop of water on the cross-section (Figure 3.15) and penetrate the cross-section with a single plunge. Spindle speed should be set to approximately 7000 rpm and a plunge speed of 0.75 mm/min should be used (these milling parameters were kept constant throughout the project);

Step 4 - Retract the tool after running the coring procedure;

Step 5 - Using the lamp to light the cross-section from the side, manually extract the osteons from the sample with tweezers;

Step 6 - Examine the produced cylinders using a reflected light microscope at 50x magnification.

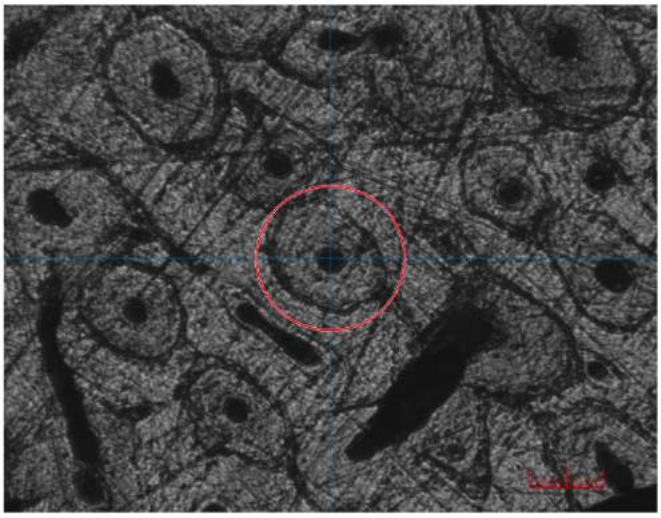

Figure 3.14: A MatLab program window with cross-hairs set at the centre of the osteon image. Scale bar is $100\mu m$

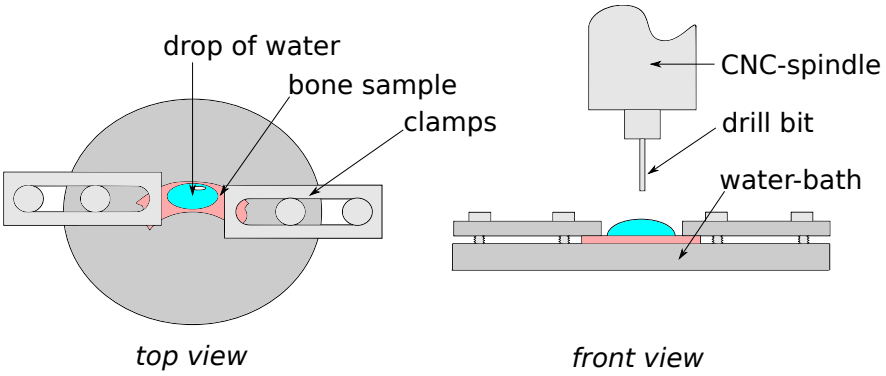

Figure 3.15: Top (left) and side (right) views of the custom water bath showing an applied drop of water on a bone sample before drilling

3.5.3 Calibration procedure for the CNC-system

Calibration of the modified CNC-system was performed in two steps. The first step included callibrating the position of camera body so that the vertical axis of the camera lens was set perpendicular to the cross-section surface. This step ensured that the centre of an osteon would stay in the centre of the live image capture at each magnification level of the optical system (Figure 3.16).

The purpose of the second calibration step was to identify accurate offset values (x_c , y_c) of the camera vertical axis from the vertical drill axis. These values were used in the coring procedure to set the zero-position in the x-y plane of the CNC-machine before initiating the coring procedure (described in Section 3.5.2). To identify the offset, the drill bit was brought into contact with the bone

sample and the x-, y-, and z-axis were zeroed out. Then, one plunge to half the sample depth was performed and the drill-bit was retracted. The position of the milled hole was found and the corresponding x- and y-coordinates were recorded (Figure 3.17).

Due to the presence of backslash in the CNC-system, after 10 plunges an error of up to 40 μm in the positioning was accumulated. Therefore, the "offset" calibration step had to be performed anew with regular frequency in order to avoid the accumulation of positioning errors.

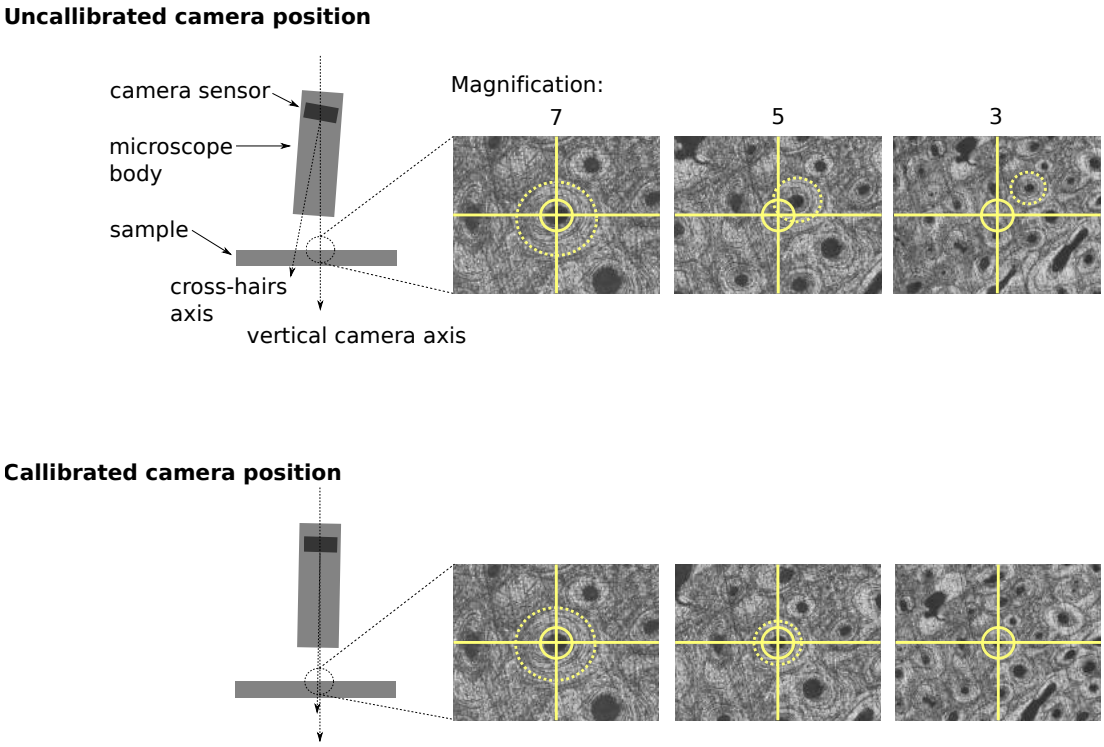

Figure 3.16: Step1. Calibration of the camera position

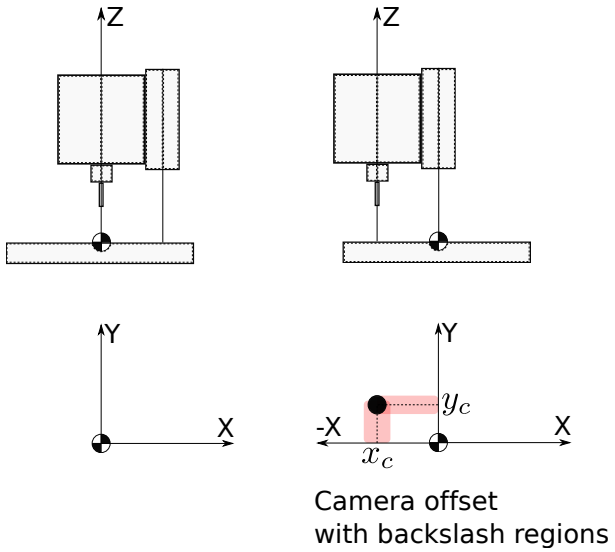

Figure 3.17: Step2. Calibration for camera offset

3.5.4 Evaluation of structural properties of osteons

After coring out the targeted osteons from the bulk material of bone, the osteons were examined with reflected light microscopy at 50x magnification to identify their height and diameter. To identify possible structural and material property predictors of osteon mechanical strength, every osteon was scanned using micro-computed tomography (μCT) prior to mechanical testing. For each set of samples, a certain selection of osteonal properties was evaluated. The specific set of properties evaluated for the sets of bovine osteons and for the sets of human osteons are described in Sections 4 and 5 respectively.

The μCT data was processed using ImageJ and its plug-in BoneJ [63], to asses the following parameters:

- **Diameter of osteon** (D) [μm]. Ferret's diameter was estimated through the height of the osteon and averaged to get D.
- **Height of osteon** (H) [μm]. Height was measured three times and averaged to get H.
- **Percentage of longitudinal Haversian canal** [%] was estimated for the first bovine samples only to ensure that they consisted of mainly osteonal bone (Figure 3.18).

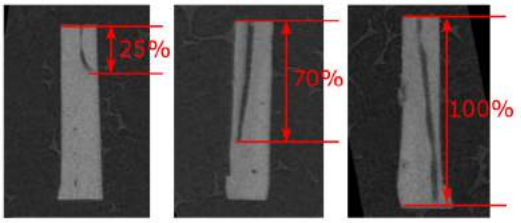

Figure 3.18: The longitudal view of the samples in set-1 (#2, #10, #7) with 25%, 70% and 100% of the Haversian canal present

- **Cross-sectional area** (CSA) [mm^2]. Cross-sectional area was also estimated through the height of the osteon and averaged to get CSA (Figure 3.19).

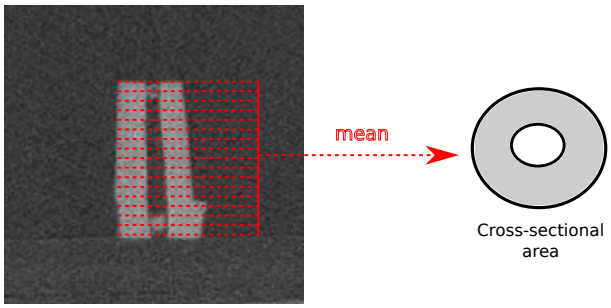

Figure 3.19: Cross-sectonal area evaluation

- BV/TV [%]. BV/TV was calculated from a circular region of interest that included the Haversian canal.

- Inclination angle of Haversian canal $[deg]$. Inclination angle of the Haversian canal from the longitudinal axis of the osteon was estimated following the procedure graphically described in Figure 3.20.

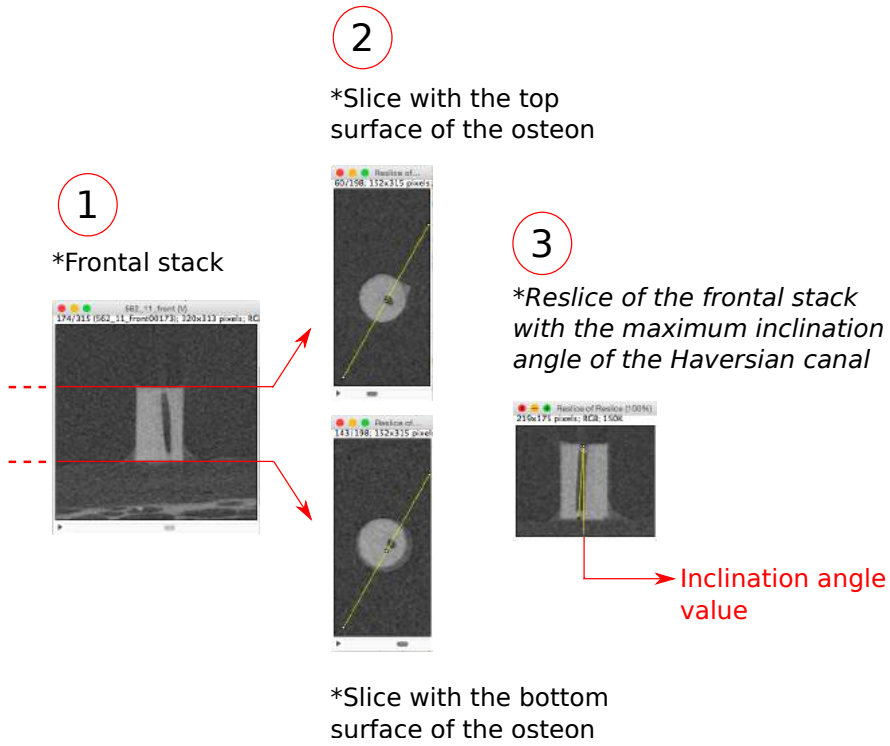

Figure 3.20: Graphical representation of the procedure used to determine inclination angle values

- **Mineral density** (BMD) $[mgHA/ccm]$. BMD values were determined by analysing the μCT images, the mean grey value of the frontal osteonal cross-section was measured and compared with the mean grey values of three μCT phantom samples with a known BMD value. As shown in Figure 3.21, the mean grey values were interpolated to physical density values.

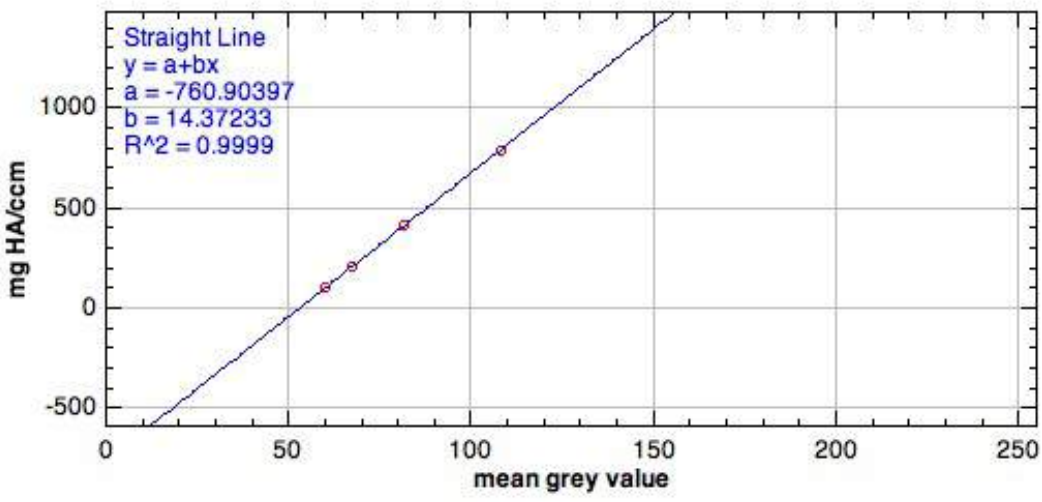

Figure 3.21: BMD evaluation. Physical density vs Grey scale value

In addition to the μCT data, the last four sets of human osteons were scanned with a Second-harmonic Imaging Microscope. In this study, SHG imaging was performed on an upright Zeiss LSM 510 NLO laser scanning multi-photon microscope (Zeiss, Jena, Germany) equipped with a mode-locked femtosecond Ti:Sapphire laser (Coherent Chameleon XR, Coherent Inc, Santa Clara, USA), tunable rom 720 to 980 nm. The method of Second-harmonic Imaging is based on the ability of materials to generate second-harmonic light in response to the applied incident light. Second harmonic generated (SHG) light is exactly half the wave length of the incident light ($\lambda = 800nm$). In order for the generated light to double in frequency, the molecular structure of the scanned material should be specifically oriented. The basic structure of collagen fibril (a triple helix of three protein chains) gives collagen the intrinsic ability to emit SHG. The optical process of SHG is also sensitive to the angular orientation of the scanned fibrils within the focal volume [64], this enables the estimation of the spatial orientation of collagen within the osteon.

Aszensi et. al categorised osteons into dark, grey and light according to their collagen fibre orientation [1], an example of a "light" and a "dark" osteon can be seen in the Figures 3.22 and 3.23, respectively. In SHG images of the dark osteons, a large portion of the osteon surface appears dark (close to 0 grey value); however, the Auto-Fluorescence image shows that collagen is present in that region (Figure 3.23). This phenomenon can be explained by longitudinal orientation of the collagen fibres in this region, relative to the applied incident light. In this study the higher the grey-value intensity of the osteonal cross-section, the more longitudinal fibres were assumed to be present in the cross-section. The SHG intensity (I or SHG intensity) parameter for each image was estimated as follows:

$$I = \frac{MGV}{256} * 100. \tag{3.1}$$

Herein, MGV is the mean grey-value of the region of interest (ROI) in the SHG image. An example-ROI in an SHG image is presented in Figure 3.25. As such, osteons with low I-values were classified as "dark" and those with high I-values were classified as "light".

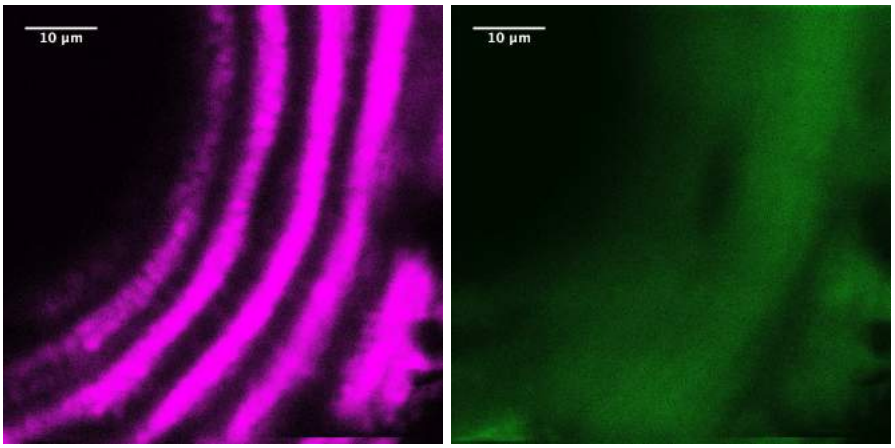

Figure 3.22: SHG (left) and Auto-Fluorescence (right) images of the cross-section of a "light" osteon

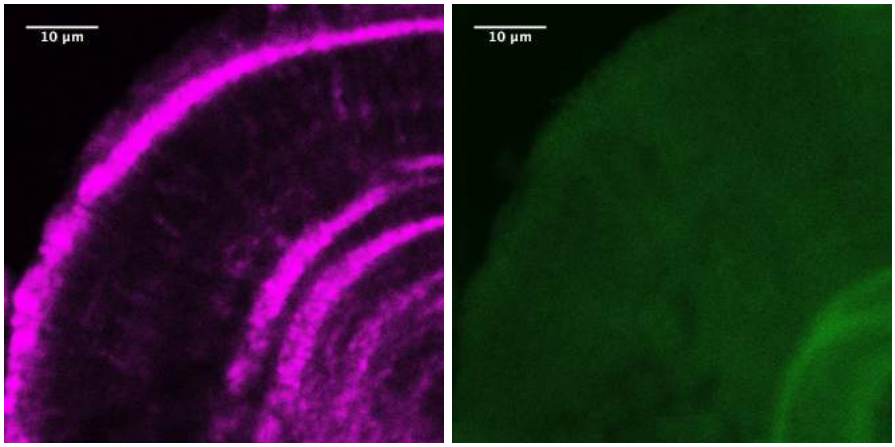

Figure 3.23: SHG (left) and Auto-Fluorescence (right) images of the cross-section of a "dark" osteon

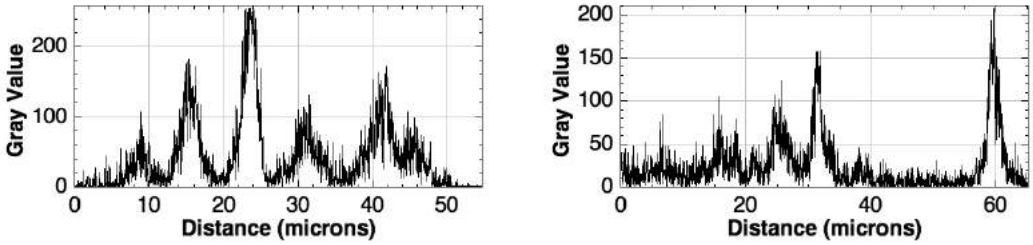

Figure 3.24: Intensity profile plot across the radius of the "light" osteon from Figure 3.22 (left) and the "dark" osteon from Figure 3.23 (right)

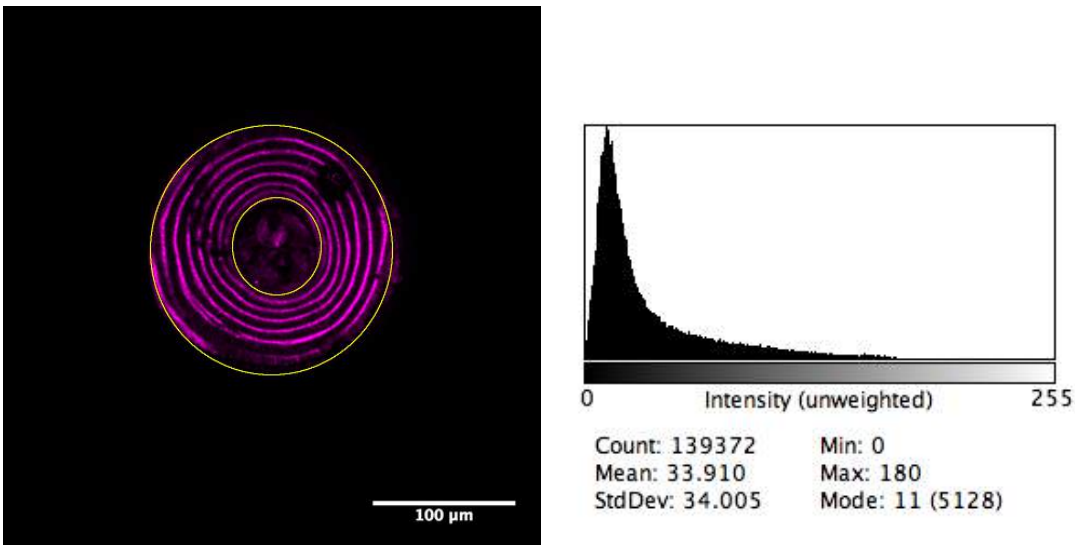

Figure 3.25: ROI and a histogram of intensity

3.6 Compression testing

3.6.1 Compression testing set-up

For this project, two compression testing set-ups were designed and evaluated. Harvested osteons were loaded under uniaxial compression by a servo-electric axial testing system (Thelkin AG, Winterthur, Switzerland). A high resolution video camera allowed for optical documentation of each test.
The "Thelkin" system included a 100 Newton load cell with a cross-head-mounted actuator and a test controller that allowed for displacement controlled tests. In the first version of the compression testing set-up (Figure 3.26), a metallic cylinder was attached to the moving load cell and a water-bath with a second metallic cylinder was firmly fixed to the table of the "Thelkin" system.

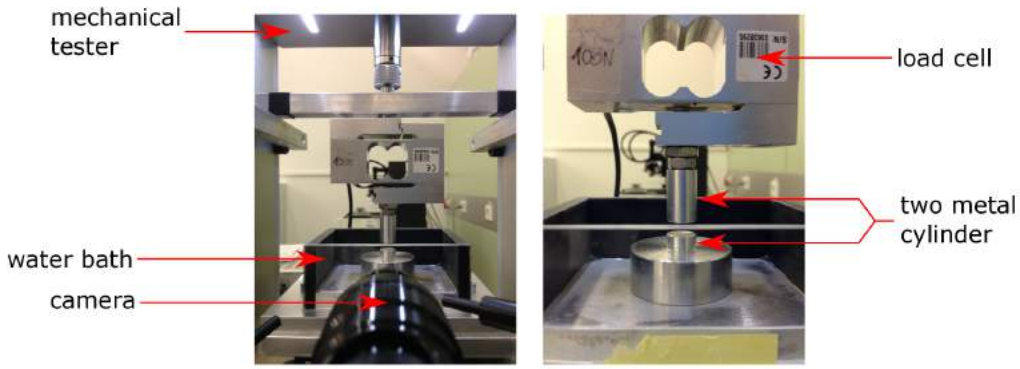

Figure 3.26: The first compression testing set-up

After a number of experiments, reflected light from the metalic surfaces of the cylinders was found to interfere with the optical documentation of the test. The large diameters of cylinders also impeded tracking of the behaviour of the osteons under compression. Therefore, a second version of the compression testing set-up was developed (Figure 3.28). The new fixture was coated with black matte paint coating and the shape of the compression platens were tapered to improve the visibility during testing (Figure 3.27).

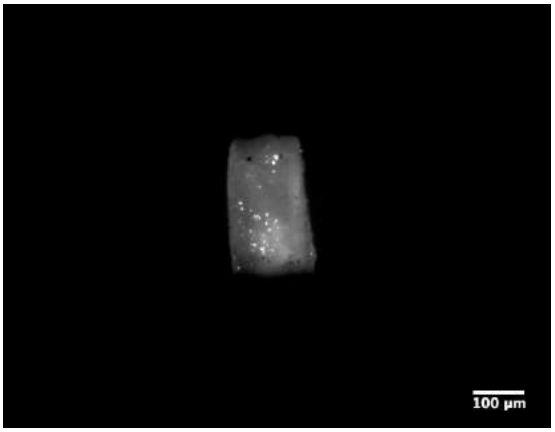

Figure 3.27: An image of the osteon in the second, improved version of the compression testing set-up

Figure 3.28: The second version of the compression testing set-up

3.6.2 Loading profiles

Two principal loading profiles were used in this study: continuous loading and step loading. These are presented in the Figure 3.29. The step-loading profile was developed to include at least two unloading cycles within the elastic region.

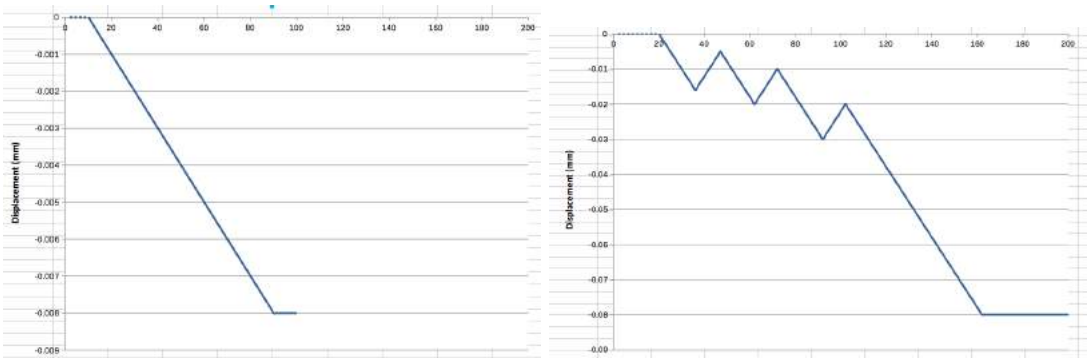

Figure 3.29: A continuous loading profile (left) and a custom step-loading profile (right)

3.6.3 Interpreting results of the compression testing

Results of mechanical testing were analysed using Python and its module TrackPy. The following mechanical properties were calculated:

- Maximum Load (F_{max}) [N],
- Maximum Stress (σ_{max}) [MPa],
- Yield Strain (ε_{yeild}) [-],
- Yield Stress (σ_{yeild}) [MPa],
- Elastic Modulus (E) [GPa].

The measured mechanical properties are graphically represented in Figure 3.30.

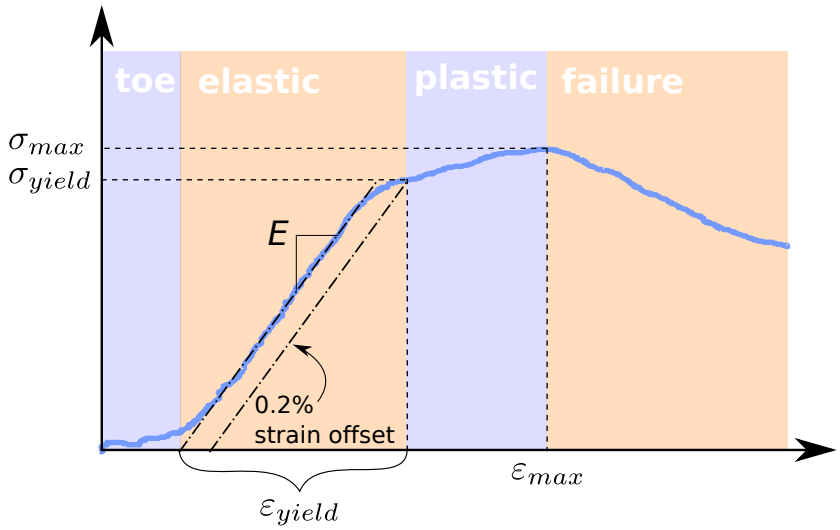

Figure 3.30: Evaluation of mechanical properties

Load data from the "Thelkin" system and displacement data from the video feed analysis (also performed in Python) were filtered (Figure 3.31) and matched. Stress (σ) and strain (ε) values were calculated as follows:

$$\sigma = \frac{F}{CSA} \tag{3.2}$$

$$\varepsilon = \frac{X_y}{H} \tag{3.3}$$

Herein, F is load, CSA - cross-sectional area of osteon, X_y - vertical displacement and H - height of osteon. Then, stress-strain curves were plotted and an elastic region was manually chosen (Figure 3.32 left). A linear function was then fitted to the elastic region of the stress-strain curve and the linear coefficient was calculated to give the elastic modulus. Then, the fitted line was calculated with a 0.2% strain offset. At the point of this line's intersection with the stress-strain curve, the value of yield stress and yield strain were determined (Figure 3.32 right).

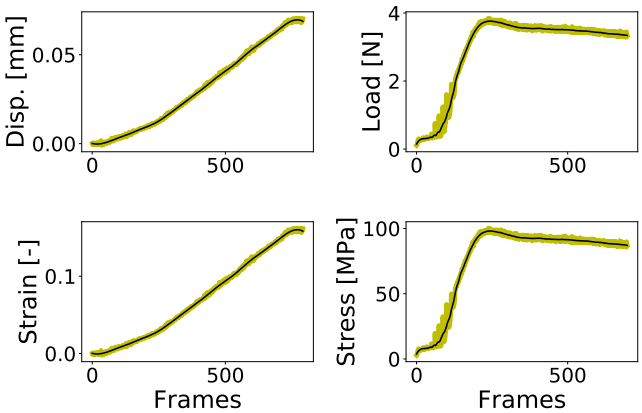

Figure 3.31: Raw (yellow) and filtered (black) displacement (top left), load (top right), strain (bottom left) and stress (bottom right) data of sample number 15 in set 9

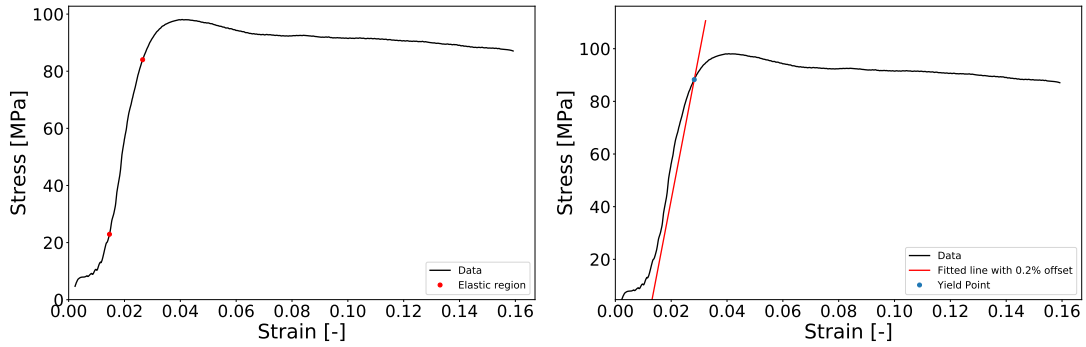

Figure 3.32: The manually chosen elastic region (left) and a fitted line with 0.2% strain offset with the yield point labelled (right)

Statistical analysis

In order to estimate the relationships between the 'structural predictor' data set and the 'mechanical property' data set, a simple linear regression analysis was used. The R-squared of the regression represented the fraction of the variation in a given dependent variable (mechanical property) that was predicted by a given parameter (structural parameter). The p-value was of major importance as it represented the significance of the found correlation. The significance level (p-value) of 0.05 or 95% is assumed for the tests unless stated otherwise.

In order to determine if there was a significant difference in sets of the measured data from mechanical testing, the data was statistically analysed with predefined statistical functions in Python: namely, one-way Analysis of variance (ANOVA), Kruskal Wallis H Test and Mann–Whitney U test.

From the mentioned tests, ANOVA tests are believed to provide the most reliable results. To perform a one-way ANOVA test, the following assumptions for the data should be met:

1. The samples are independent.
2. Each sample is from a normally distributed population.
3. The population standard deviations of the groups are all equal. This property is known as homoscedasticity.

If the assumption of normality was not met a non parametric Mann–Whitney U test was used. The null hypothesis of which states that the samples come from the same distribution, and if the significance value is lower than 0.05, the two groups are assumed to be significantly different.

If the assumption of homoscedasticity was not met, a Kruskal Wallis H Test was used. This test is the non parametric alternative to the one-way ANOVA.

To check for normality, a Shapiro-Wilk test was used. The null hypothesis of the test assumes that the sample data are not significantly different from a normal population. Small values of W are evidence of a departure from normality. The W statistic is calculated as follows:

$$W = \frac{(\sum_{i=1}^{n} a_i x_{(i)})^2}{\sum_{i=1}^{n}(x_i - \bar{x})^2} \tag{3.4}$$

Herein, $x_{(i)}$ are the ordered sample values ($x_{(1)}$ is the smallest) and a_i are the constants generated from the means, variances and covariances of the order statistics of a sample of size n from a normal distribution (see [65]).

Each data set was checked for the presence of statistical outliers with a Grubb's test. The null hypothesis of the Grubb's test assumes that there are no outliers in the data set. Grubb's statistic is defined as:

$$G = \frac{max|Y_i - \bar{Y}|}{s} \tag{3.5}$$

The hypothesis of no outliers is rejected if:

$$G > \frac{n-1}{\sqrt{n}} \sqrt{\frac{t^2_{\alpha/n,n-2}}{n-2+t^2_{\alpha/n,n-2}}} \tag{3.6}$$

Herein, $t^2_{\alpha/n,n-2}$ is the critical value of the t-distribution with $(n-2)$ degrees of freedom and a significance level of α/n.

Bertlett's test was used to check for homoscedasticity of the E, σ_{max}, σ_{yield}, BV/TV, BMD and SHG intensity data sets with normal distribution of data. If the p-value was found to be less than the level of significance for this test (0.05), the variances of the two data sets were not the same. In that case, the groups were assumed to be heteroscedastic. If the p-value was greater than the significance level the test failed to reject the null hypothesis and the groups were assumed to be homoscedastic.

3.7 Summary

Methods for isolation and compression testing of single osteons were developed. In the development process, bovine bone was chosen as a tissue for the trial experiments due to its morphological similarity to the human bone tissue. The CNC-system was modified to house a camera-microscope and then calibrated; a number of eccentric drill-bits were produced; and the approaches used to evaluate the morphology of the osteons and interpret the results of compression testing were chosen.

The research objectives of this chapter have been met. A new procedure to isolate and mechanically test osteons was designed and optimised. Further, the results of compression testing can be directly compared to Ascenzi's work.

The developed methodology allows for a greater automation of osteon isolation procedure. By implementing this procedure in future research, biomechanics of single osteons can be extensively studied.

Chapter 4

Compressive mechanical properties of bovine osteons

4.1 Introduction

In experimental bone research, animal tissue is commonly used for the trial experiments, due to its increased availability and reduced legal regulations. Animal models are, in general, used to provide preliminary understanding of experimental outcomes. Bovine bone is extensively used in bone micro-mechanics research due to its structural similarity to human bone. At a macro-level bovine bone is comprised of cortical and trabecular bone. Bovine cortical bone further consists of three subtypes: osteonal, interstitial and plexifom. The plexiform bone is made up of unorganised lamellae sheets that are perforated by a plexus of blood vessels, this type of bone is not present in humans. However, bovine osteonal bone organisation shows close affinity to human. It is made up of osteons that span throughout the bone in the longitudinal direction.

Besides having a similar structure, the mechanical properties of bovine and human bone also seem to show similarities [47]. At a macro-level, strength and stiffness of bovine bone has been reported to be similar to that of human bone when measured in the transverse direction; however, bovine bone seems to give consistently higher values in the longitudinal direction [51]. At a micrometer-level, the values of bovine osteon elastic modulus have been estimated using a nano-indentation technique. Wang et al. (2006) reported a value of 24.7±2.5 GPa [66], whereas a value of 21.0±5.9 GPa has been reported for human bone [67]. However, compressive testing on individual bovine osteons has not yet been conducted.

As the first objective of this thesis was to establish a reliable procedure to harvest and test individual osteons, bovine cortical bone was chosen as a trial material for the first experiments. With the developed procedure, it was possible to obtain and test 61 bovine osteons. In Appendix A, geometrical parameters and the course of mechanical testing are described in detail. The measured mechanical properties of bovine bone are presented in this chapter. Furthermore, the measured data was statistically evaluated with a regression analysis in order to estimate what structural parameters could be used to predict mechanical properties of bovine bone.

4.2 Research objectives

The following questions were addressed in this chapter:

- What are the compressive properties of individual bovine osteons?
- Are there any structural parameters that correlate with the mechanical properties of individual bovine osteons?

4.3 Mechanical properties of bovine osteons

Before bovine osteons were subjected to mechanical testing, structural parameters were evaluated. This included BV/TV, BMD and the Inclination angle of Haversian canal. The histograms of the bovine structural parameters are shown in Figure 4.1.

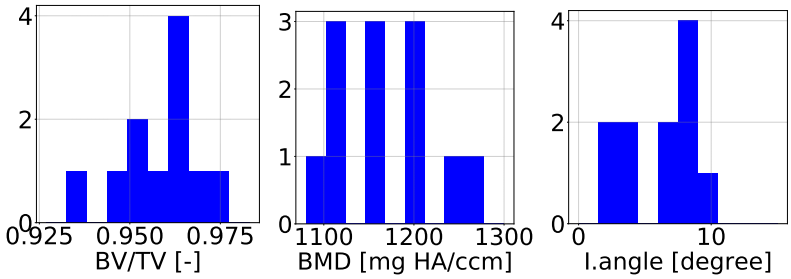

Figure 4.1: Histograms of the measured structural properties for the bovine osteons

As mentioned in section 3, BV/TV is the bone volume over the total tissue volume ratio. As the Haversian canal was included in the tissue volume measurment, BV/TV mainly represents the size of Haversian canal and its branching. For bovine osteons, BV/TV varied from 0.90 to 0.97. The high values of BV/TV show that the Haversian canals in bovine bone were relatively small and μCT images showed that a number of side canals were present within the osteons (Figure 4.2).

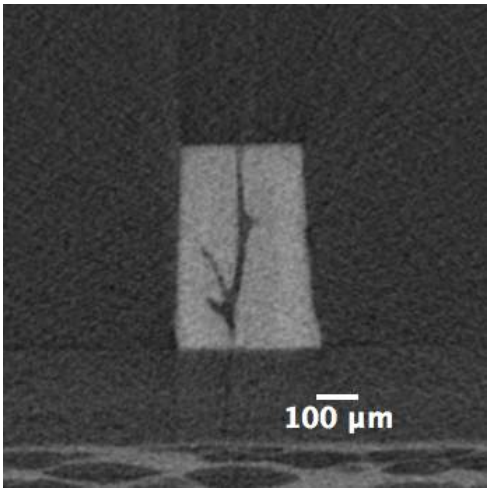

Figure 4.2: μCT scan images of a bovine osteons with branching

The wide range of BMD values and their clear fragmentation in the histogram show that osteons with different levels of mineralisation were present. The large difference in mineral content suggests that the osteon set was comprised of osteons of different age and, therefore, at different stages of mineralisation. Such diversity may be explained by the high rate of bovine bone growth. Human bone reaches its maturity in 16 years, whereas bovine bone is considered fully mature at 2 years [68]. The angle of Haversian canal inclination from the long axis varied from 2 to 10 degrees.

As explained in Appendix A, osteons from set-1 experienced buckling during compression testing and the mechanical properties were not determined. For the

set-2 osteons, no video was recorded. Therefore, displacement data was obtained directly from the "Thelkin" system. The values of the calculated mechanical properties were substantially lower for set-2 than those for set-3, which used a more precise method of video-feed analysis. Therefore, only the values of 13 samples from set-3 were used for determining the mechanical properties of bovine osteons.

The following mechanical properties were calculated for bovine osteons: maximum experienced load (F_{max}) , maximum stress (σ_{max}) , yield strain (ε_{yield}), yield stress (σ_{yield}) and elastic modulus (E). The values of all the calculated mechanical properties are presented in Table 4.1 and the histograms are given in Figure 4.3.

	F_{max} [N]	σ_{max} [MPa]	ε_{yield} [-]	σ_{yield} [MPa]	E [GPa]
set-3	7.92 [1.55]	126.49 [11.09]	0.03 [0.01]	109.17 [12.98]	4.10 [1.06]

Table 4.1: Mechanical properties of bovine osteons

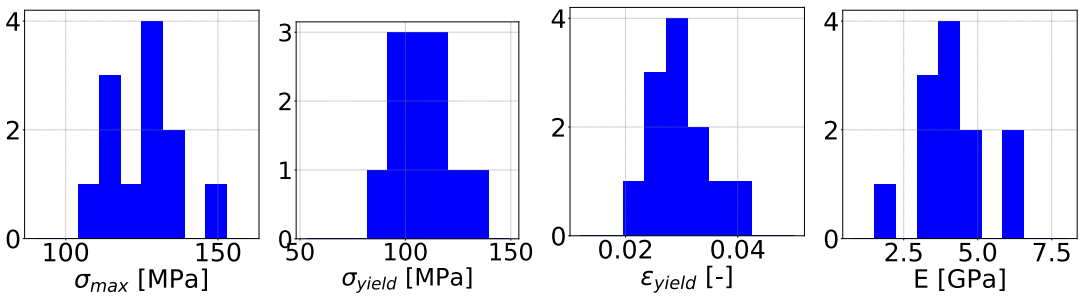

Figure 4.3: Histograms of the calculated mechanical properties for the bovine osteons

Regression analysis was perform to identify if there were significant correlations between structural and mechanical properties of the bovine osteons. Detailed information on all of the regression analyses can be found in Appendix IV.

Of all of the measured structural properties, only BV/TV was found to be a significant predictor of ε_{yield} ($R^2 = 0.34$, $p = 0.02$) (Figure 4.4). No other significant correlations were found between bovine osteon structural and mechanical properties.

As BV/TV represents the Haversian canal size and its branching, the high values of BV/TV would mean a smaller size of the Haversian canal and the side canals. The BV/TV - ε_{yield} correlation suggests that as the Haversian canal reduces so will ε_{yield}. Materials with low values of ε_{yield} are often characterised as brittle materials. Since the $p = 0.04$ for this correlation is close to the 0.05 critical value, the prediction may be ambiguous. Although, the osteons with the smaller Haversian canals appeared to be less ductile, this phenomenon may be due to a number of affecting parameters that were not measured in this study. For example, ductility of osteons might be affected by intralamellar properties, collagen quality or a combination of collagen orientation and mineralisation. Further research must be conducted to draw correct conclusions on the correlation between BV/TV and ε_{yield}.

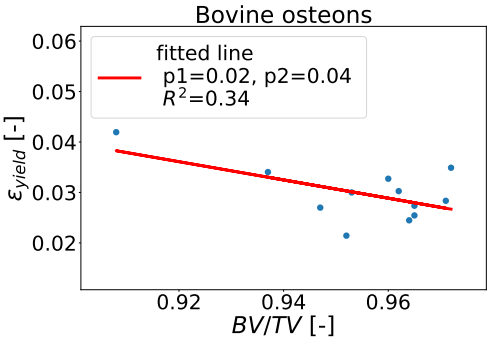

Figure 4.4: Influence of BV/TV on F_{max} and ε_{yield}

4.4 Summary

A set of 13 bovine samples was obtained and successfully mechanically tested. Structurally, bovine osteons had small Haversian canals with several side branches. The only significant predictor of ε_{yield} for bovine osteons was BV/TV, which suggested that osteons with smaller Haversian canals yield at lower strains and are, therefore, less ductile. However, the significance level of p=0.04 shows that this observation might be ambiguous and, therefore, the correlations between structural and mechanical parameters of bovine osteons should be studied with a larger number of samples to obtain a clearer result. The elastic modulus of bovine single osteons was found to be 4.10±1.06 GPa, which is substantially lower than the values reported from nano-indentation tests (24.7±5.9 GPa) [66].

This chapter showed that it was possible to determine compressive properties of bovine osteons. The measured elastic modulus value was comparable but lower than the ones previously measured by nano-indentation. BV/TV was found to be a significant predictor of ε_{yield}. The presence of this correlation showed that there might be a significant dependency between the structure of the osteon and its mechanical properties and, therefore, in further experiments more attention was paid to the structural parameters as possible predictors of osteonal strength and toughness. Furthermore, for a better understanding of failure mechanisms, the mechanical testing setup used for bovine tests was modified as described in section 3.6.1. This allowed for an observation of osteon behaviour under compression.

The experiments with the bovine bone showed that it was possible to test individual osteons in compression and obtain viable data.

Chapter 5

Effects of ageing on human osteon strength

5.1 Introduction

The incidence of pathological and age-related bone fracture increases dramatically with age [5]. To understand pathological mechanisms in bone, one must first understand the natural changes in healthy bone with age. Existing clinical methods for assessment of bone quality are inadequate for predicting bone fracture risks [69], [70]. As bone is a hierarchically organised structure, mechanical properties of the smaller bone components are a missing part in our knowledge of the effects of ageing on bone. At the micrometer-scale, the largest functional units of cortical bone are the osteon, they are believed to provide cortical bone with its strength. The osteon is a complex biomehcanical system, whose biological and mechanical functions are strongly interdependent. However, the information on mechanical properties of osteons is scarce. The existing knowledge is largely based on the work of Acsenzi et al.. Compressive mechanical properties of individual osteons were evaluated by Aszenzi et al. in 1968 [1]. The values of elastic moduli were reported to vary from 1.6 to 9.3 GPa for a 30 year donor. However, the values repored by Ascenzi et al. have not been validated or repeated by any other experimental research.

In the past 25 years, new nano-indentation techniques have been developed to assess bone mechanical properties at the micrometer-level. The elastic modulus of an osteonal structural unit, measured using the micro-indentation tests, was reported to vary from 15.1 to 26.9 GPa [67], diverging from the values measured with compression testing in the 1960s. Modern approaches for the determination of elastic modulus of extracellular bone matrix at the micrometer scale include step-wise compression testing. Step-loading protocols allow for estimation of elastic moduli at the unloading segments of the stress-strain curves. As elastic mechanical energy is considered to be recoverable, the unloading portion of the curve within the elastic region is assumed to reveal the "true" elastic modulus of the material [2], [71].

In this thesis, compressive properties of osteons were assessed with continuous loading compression protocols to validate the values reported by Aszenzi et al.. Then, step-wise compression protocols were applied to investigate if the values reported by Aszenzi et al. represent the "true" elastic modulus of the osteon. Bone from 93 and 64 year old male donors was used to investigate the effects of aging on human osteons. With the established procedure described in section 3,

two sets of osteons were prepared; namely, set-8 for the older donor and set-9 for the younger donor. Detailed information on geometrical parameters and the course of the mechanical testing can be found in Appendix A. The two sets were subjected to equal storage and testing conditions and, therefore, the structural parameters and the measured results of mechanical testing were assumed to be comparable.

5.2 Research objectives

The following research questions were addressed in this chapter:

- Does ageing affect the failure modes or flaw tolerance of individual osteons?
- Do the mechanical properties of individual osteons change with age?
- Are the values reported by Ascenzi representative of the "true" elastic modulus?

5.3 Effects of ageing on human osteon strength

5.3.1 Failure modes

Osteons from set-8 of the older donor and set-9 of the younger donor were tested in uni-axial compression with a continuous loading profile. Similarly for each of the osteons tested, the samples recovered up to 70% of their original height after the load had been removed (Figure 5.1). The hight recovery of the osteons demonstrate elastic behaviour of the osteonal structure. *In vivo* osteons are loaded in compression and their ability to elastically regain their shape meets physiological demands. If overload occurs and plastic damage accumulates inside osteons, they are able to recover their shape and hold the bone structure. Sequential images of the damage accumulation from the uni-axial compression tests for the remaining osteons in set-8 and -9 with the corresponding strains can be found in Appendix E.

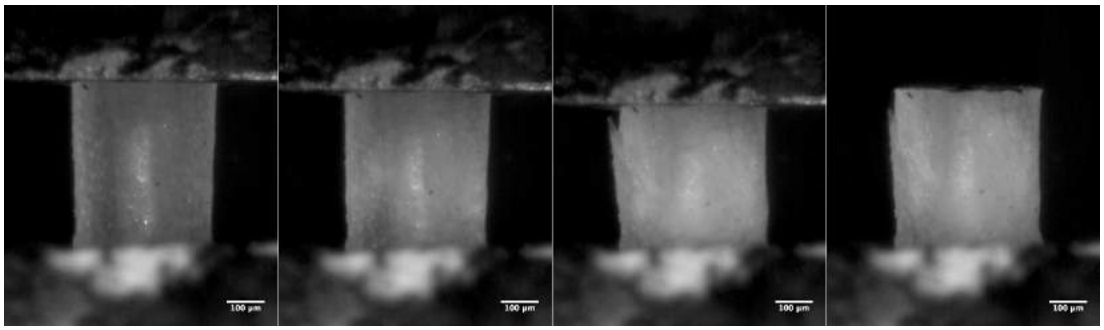

Figure 5.1: Sequential images from the compression test on osteon #8 in set-7 including the height recovery. From left to right are at 0, 0.03, 0.08 mm displacement and after the test with load cell retracted. Scale bar is 100 μm

An optical system was installed on the mechanical tester so that it was possible to observe the process of damage accumulation in the osteons. During the compression testing, osteonal structures failed in three visually distinctive ways:

- Shear failure occurred by development of a single slip plane, as in Figure 5.2a and Figure 5.3,
- Damage accumulated uniformly, as in Figure 5.2b and Figure 5.4,
- During compression osteons bulged locally, as in Figure 5.2c and Figure 5.5.

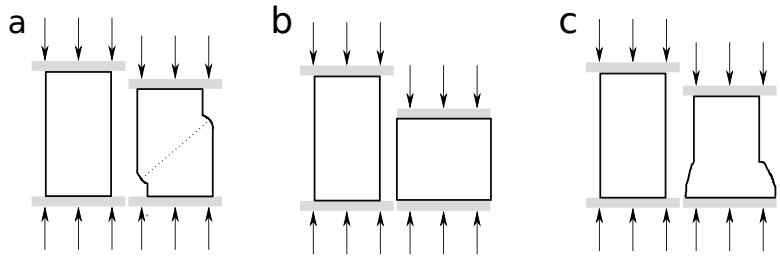

Figure 5.2: Graphical representation of osteon failure modes: (a) single plane shear failure, (b) uniform compressions failure and (c) bulging (occurred at either end of the osteon)

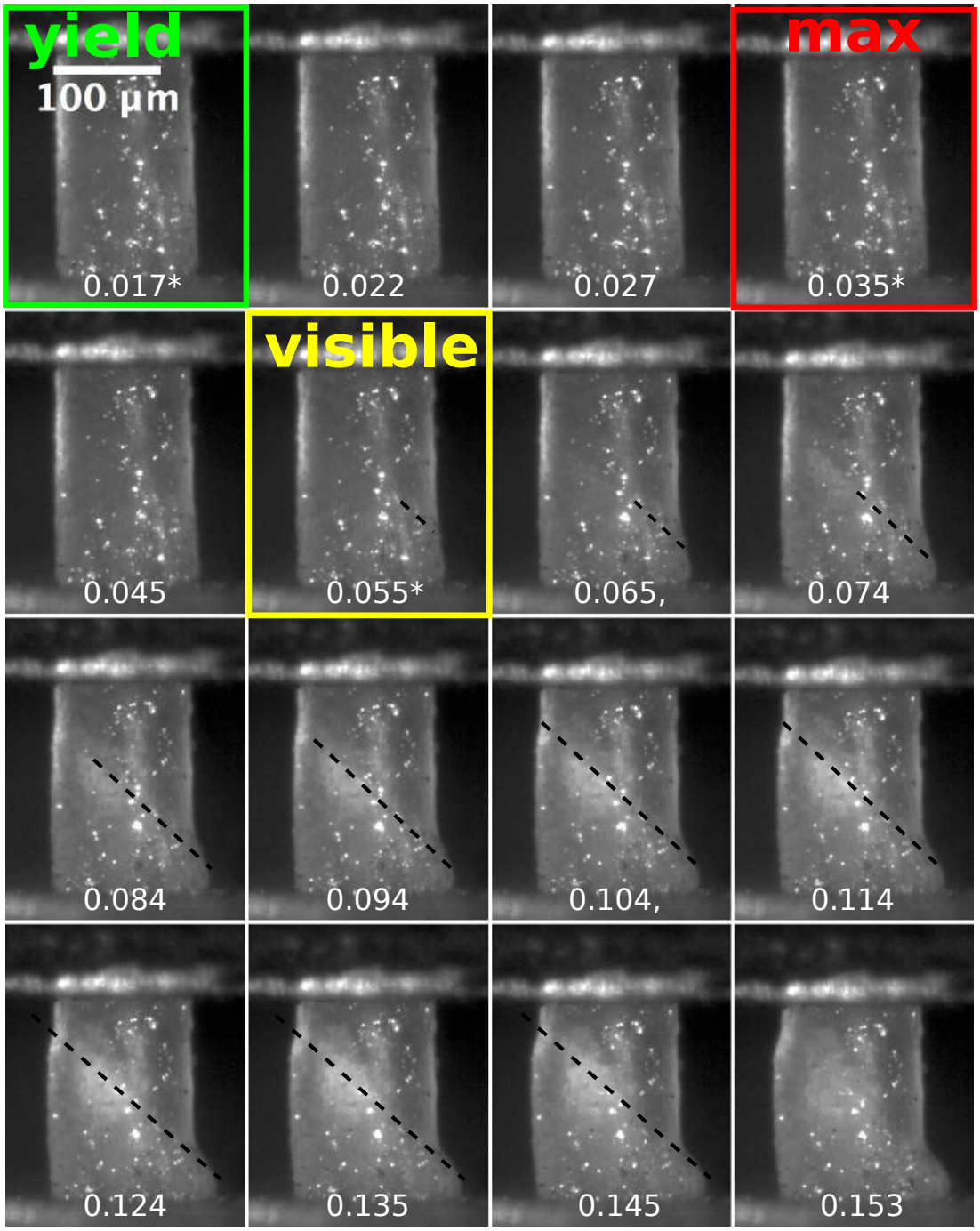

Figure 5.3: Sequential images from the compression test on osteon #06 in set-9. 0.017* strain corresponds to yield, 0.035* strain corresponds to failure and 0.055* strain corresponds to visible damage onset

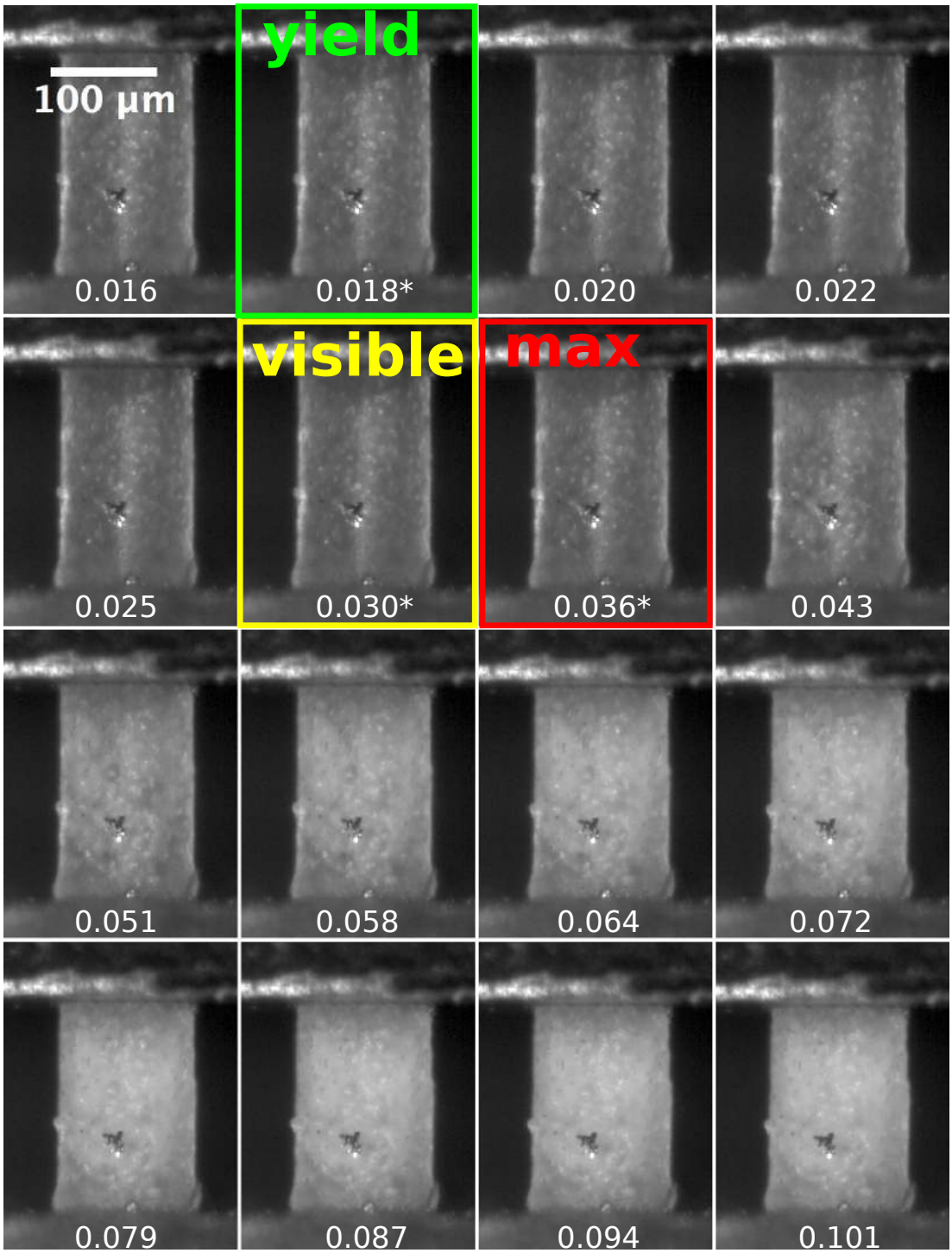

Figure 5.4: Sequential images from the compression test on osteon #10 in set-9. 0.018* strain corresponds to yield, 0.030* strain corresponds to visible damage onset and 0.036* strain corresponds to failure

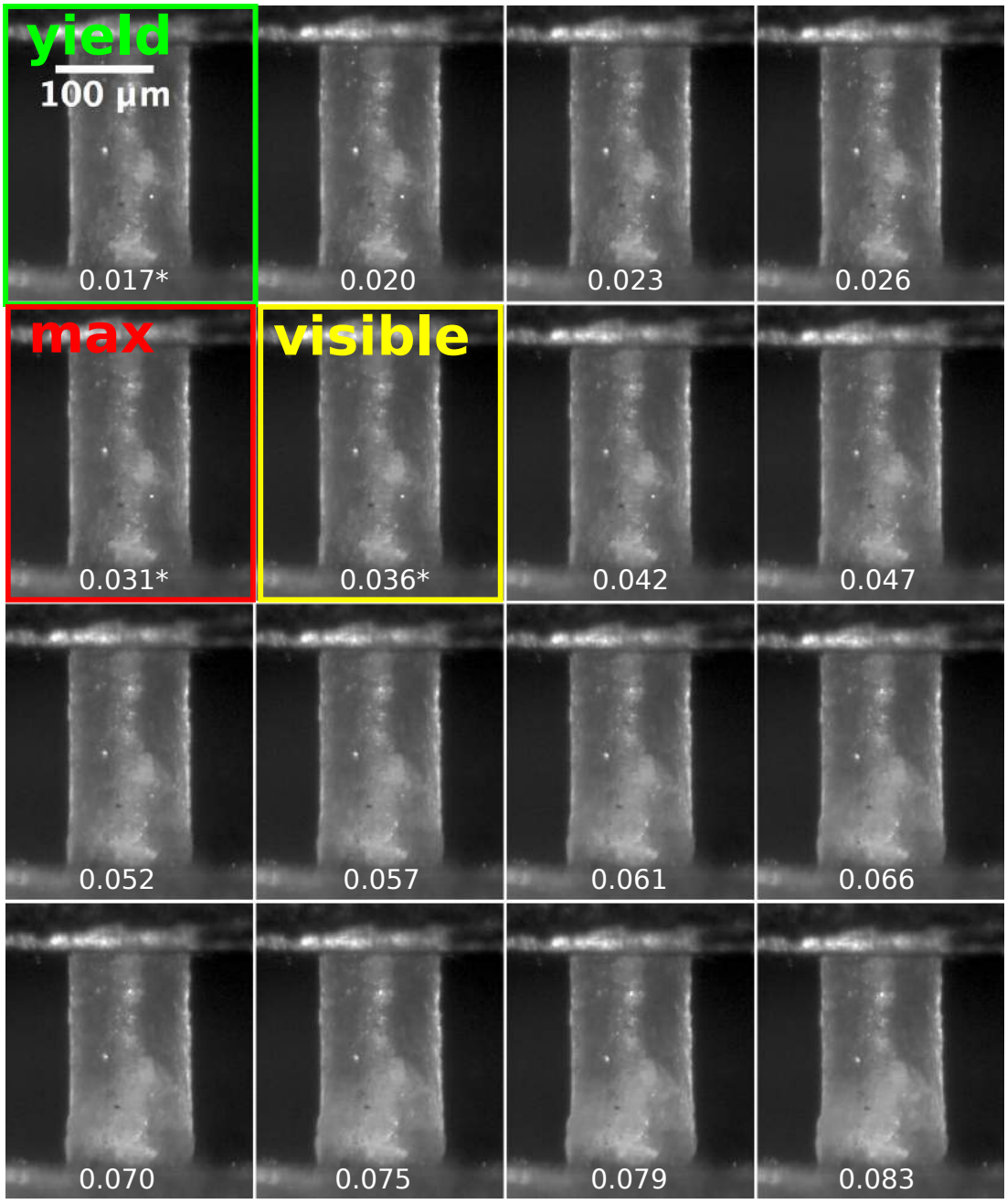

Figure 5.5: Sequential images from the compression test on osteon #08 in set-9. 0.017* strain corresponds to yield, 0.031* strain corresponds to failure and 0.036* strain corresponds to visible damage onset

Single plane shear failure occurred at roughly a 45 degree angle to the longitudinal axis, this may be because applied shear stresses exceeded the maximum shear stress limit of the osteonal structure. As a result, a fracture was induced and propagated through the lamellae sheets. Failure in shear is a characteristic failure type for ductile materials, described by the Maximum Shear Stress Theory (MSST). MSST assumes that failure occurs when a maximum shear stress reaches the value of the shear strength for a given material, leading to failure in the tensile or compression test. The same type of failure is reported to occur in dry bone micropillars tested under compression [71].

For the uniform type of failure, cracks seemingly propagated along the longitudinal axis. Material failure along the principle stress axis can be predicted by the Maximum Normal Stress Theory (MNST). In case of MNST failure, stresses normal to the loading axis within the material reach the ultimate normal stress before reaching the shear stress required for yielding, and the material fractures. The fracture in the uniform failure mode seemed to propagate along the principle stress axis between the layers of lamellae throughout the whole length of the osteon, resulting in a uniform distribution of whitening in the recorded video image. It was confirmed in the recent research that whitening of bone visible in the video image represent the occurrence of damage [72] [73]. MNST correlates well with brittle materials, but, due to heterogeneity and structural effects, uniform osteonal failure may be described as quasi-brittle. The same quasi-brittle behavior applies to the failure of cortical bone at a macro-level where fracture propagates between the lower structural components of bone, such as osteons and interstitial lamellae.

In the case of bulging failure, accumulation of damage was confined to either the top or bottom surface of the compression cylinder, constraining crack propagation to a limited area. This may be explained by the high frictional forces occurring between the osteon and the compression cylinder during testing, leading to a redistribution of forces and accumulation of higher stresses at the corresponding end of the osteon or point to the pre-existing flaws either contained in the osteon from the start or added during the preparation process. The locally induced stresses led to the local accumulation of damage. Not only structural and morphological parameters may have had an effect on bulging occurrence, but also the design of the compression testing experiment and, in particular, the chosen slenderness ratio. With regards to the test setup, surface characteristics of the compression cylinders may have also contributed to the incidence of bulging mode failure. Due to the high number of parameters that could have influenced the mechanical behaviour of the osteons, this type of failure is regarded as a structural instability, rather than a failure mode. However, the present classification was made in accordance to the video images taken only from one side on the osteons, which allows for misinterpretation of the observed failure mode. As such, an osteon failing in bulging, if observed from another side, could have in fact experienced failing in shear. In any case, osteons which failed in bulging were not used for further comparison.

5.3.2 Age vs Failure modes

No single predominant type of failure was observed for any of the two age osteon sets. However, as it can be seen in Figure 5.6, the 94 year old donor osteons mostly failed in either uniform compression or bulging, and osteons of the

64 year old donor exhibited each type of failure, where up to 35 % of samples failed in shear. Thus, osteons of the older donor experienced mostly brittle fracture, whereas the younger donor had osteons with both brittle and ductile failure modes.

Although the observations made were based on the data from two donors only, the comparison study of the osteonal behaviour from the two sample groups can provide valuable insights and ideas for the directions of future research. Despite the limited number of donors, the observation that older osteons fail in a more brittle manner than younger osteons agrees well with the common knowledge that human bone becomes more brittle with age.

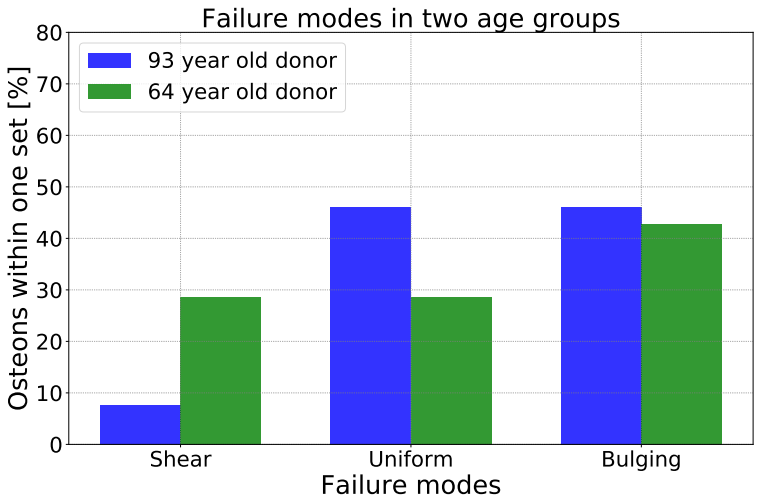

Figure 5.6: Failure modes per age set of osteons

Morphology and structural parameters vs failure modes

The structural parameters, or internal morphological flows, of osteons may have effected what type of failure occurred in osteons of both sets. To potentially predict what causes osteons to fail in a certain mode, structural and morphological parameters were evaluated.

Although statistical analysis of the data showed that there is no significant difference between the data sets (ANOVA, $p>0.5$) described in sections 5.3.2 and 5.3.2, the differences in variation and ranges of the data are further discussed. Due to a small number of samples in each data set and the high number of parameters that could have influenced the obtained data, the discussion on the variation in data ranges can give a better representation of occurring trends in behaviour of the osteons under compression.

The following structural parameters were measured for the osteons using the detailed procedure as described in section 3.5.4:

- BV/TV is the bone volume over the total tissue volume ratio. Low BV/TV values represent a high non-mineral volume fracture of the osteon (porosity). In this study BV/TV predominantly represents the morphological parameter of Haversian canal size. Potentially, the size of lacunar spaces and the space between individual lamellae also account for the non-mineral volume of the osteon and may have had an effect on the failure modes and mechanical properties of osteons. However, the limitations in sensitivity of

the μ-CT-scanner used in this study did not allow for such effects to be to evaluated.

- *BMD* represents the amount per unit volume of the mineral part of the osteon. This is a parameter similar to the one that is clinically used to access the quality of bone.

- *SHG intensity* represents the orientation of the collagen fibres in osteonal lamellae. High values of *SHG intensity* represent high angle of collagen fibre orientation relative to the principle stress axis. Osteons with a high *SHG intensity* were assumed to be bright, whereas dark osteons had a low *SHG intensity*.

To assess morphology of the osteons, μCT data were evaluated. Osteons from both sets were divided into the intact osteons (Figure 5.7a) and the osteons containing a certain imperfection, such as branching of the Haversian canal (Figure 5.7b) or the Haversian canal inclined to the side of the osteon (Figure 5.7c).

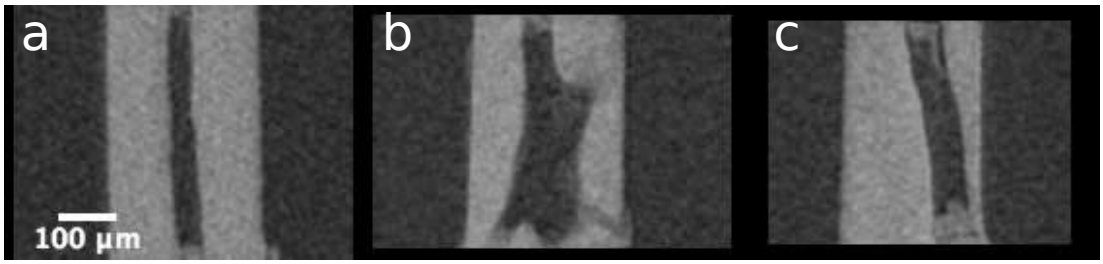

Figure 5.7: (a) Intact osteon #10 in set-9, (b) osteon #19 in set-8 with branching and (c) osteon #12 in set-8 with Haversian canal inclined to the side

From Figure 5.8, it can be seen that osteons with branching and Haversian canal inclination are present for the all three modes of failure. Intact osteons, however, failed either uniformly or in bulging; this may mean that osteons without branching tend to transmit the loading predominantly along the longitudinal axis, resulting in delamination of lamellae. In this case, propagation of a crack between the lamellae would create movement in the lacunar spaces and directly stimulate the osteocytes residing there.

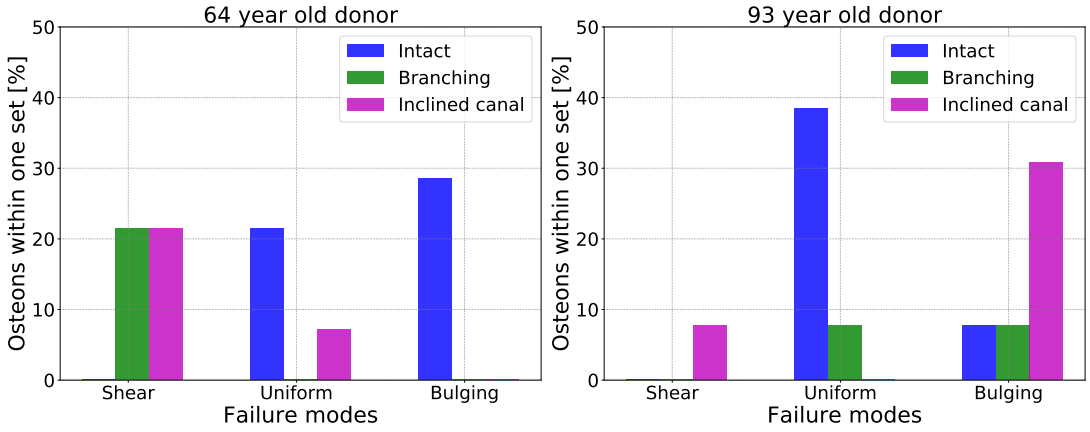

Figure 5.8: Morphological parameters of osteons as predictors of failure mode occurrence

The presence of morphological imperfections in the structure of the osteon may have caused the concentration of stresses at the site of the discontinuity. As such, either a redistribution of the local stress field or initiation of crack propagation through lamellae occurred, resulting in either bulging or shear failure, respectively. However, a small number of osteons with morphological imperfections failed in uniform compression, which means that there were additional parameters influencing the osteon failure.

According to the measured data, morphological imperfections do not directly predefine the mode of failure. The same testing procedure applied to different osteons provoked the occurrence of different failure modes due to the influence of the structural properties of osteons. Additionally, other factors, such as intralamellar properties, may have contributed to the variance in the observed failure modes.

The correlations between the structural parameters and morphology of the osteons are shown in Figure 5.9.

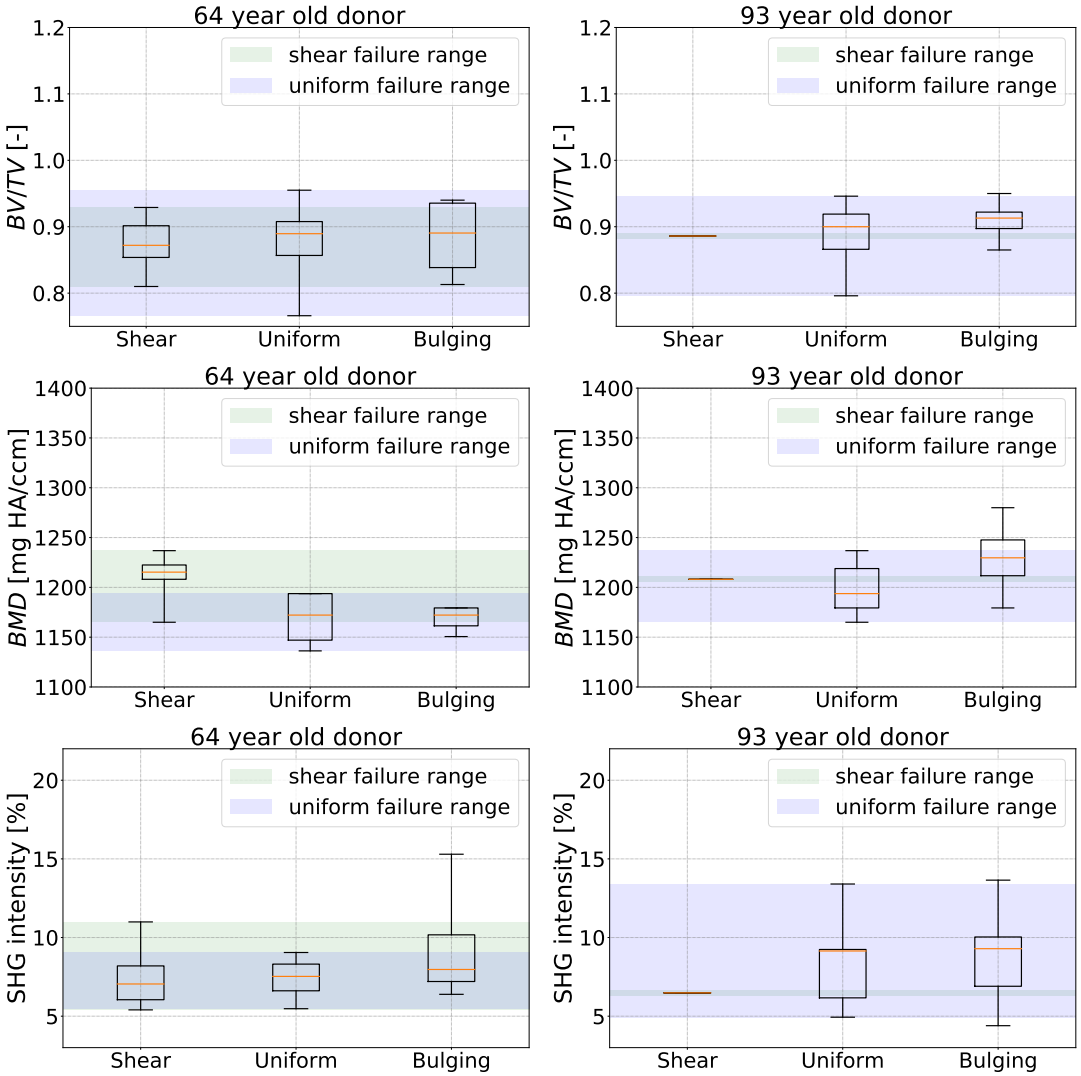

Figure 5.9: Structural parameters of osteons as predictors of failure mode occurance

BV/TV appeared to have no effect on the failure mode incidence for either donor. Interestingly, young osteons were more likely to fail in shear whereas old osteons mostly fail uniformly over the same range of BMD (1175 to 1230 mg HA/ccm). This could be due to an effect of collagen fibre orientation, since the older osteons that failed uniformly had higher values of SHG intensity, up to 13%. The combination of mostly transverse mineralised collagen fibre orientation with more mineral content may have induced a brittle fracture. The brittle type of failure occurred in younger osteons with a lower mineral content (1130-1190 mg HA/ccm) in combination with a mostly longitudinal mineralised fibre orientation. The question then arises, whether the differences in failure mechanisms imply a difference in mechanical performance of the osteons?

Failure modes vs mechanical properties

Figures 5.10, 5.11 amd 5.12 show how the mechanical properties of osteons differed between the failure modes. Osteons that failed in shear had a lower range of elastic modulus (2.4-6.5 GPa) for both donors, as presented in Figure 5.10. Osteons with elastic modulus of more than 6.5 GPa failed uniformly for the both donors or in bulging in case of the older donor.

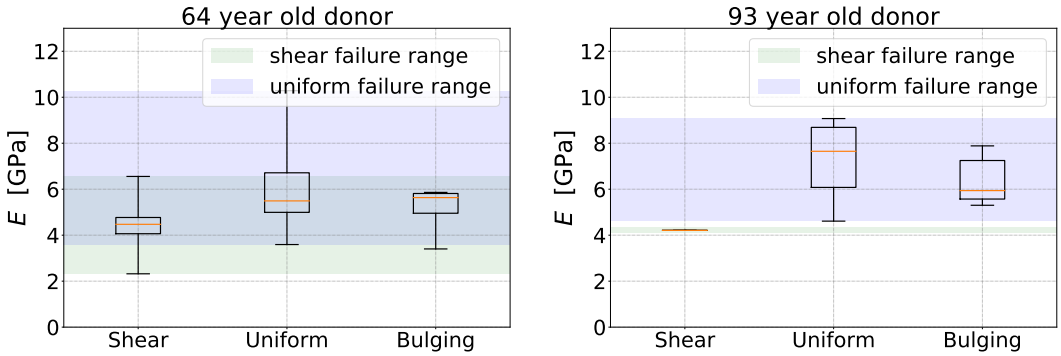

Figure 5.10: Elastic moduli of osteons in failure mode groups

Stiffer osteons were more likely to fail in a quasi-brittle manner and, in the case of the younger donor, could withstand maximum load of 50 to 160 MPa (Figure 5.11). Less stiff osteons experienced mostly ductile shear failure, and the maximum stresses of the younger donor ranged from 45 to 130 MPa. For the older donor, no osteon failed under a stress value of 100 MPa. The behavior was found for σ_{yield}, the younger donor had a higher variation in σ_{yield}, while the older donor did not experience yield under the stress value of 90 MPa.

For both donors, the aforementioned compliant osteons, that failed in shear under the lower stresses, experienced yield at higher strains as opposed to stiffer osteons that failed uniformly. Visible damage started to accumulate at higher strains and the maximum strains were higher for the compliant osteons.

Similarly for every mechanical parameter, variation of E, σ_{max}, σ_{yield}, ε_{yield}, $\varepsilon_{DamageOnset}$ and ε_{max} was higher for the younger donor than for the older donor. Osteons that failed in shear rendered features of higher toughness, such as yielding and failure occurring at lower stresses but greater strains, as compared to osteons with the uniform mode of failure. Visible damage accumulation occurred after all osteons had yielded.

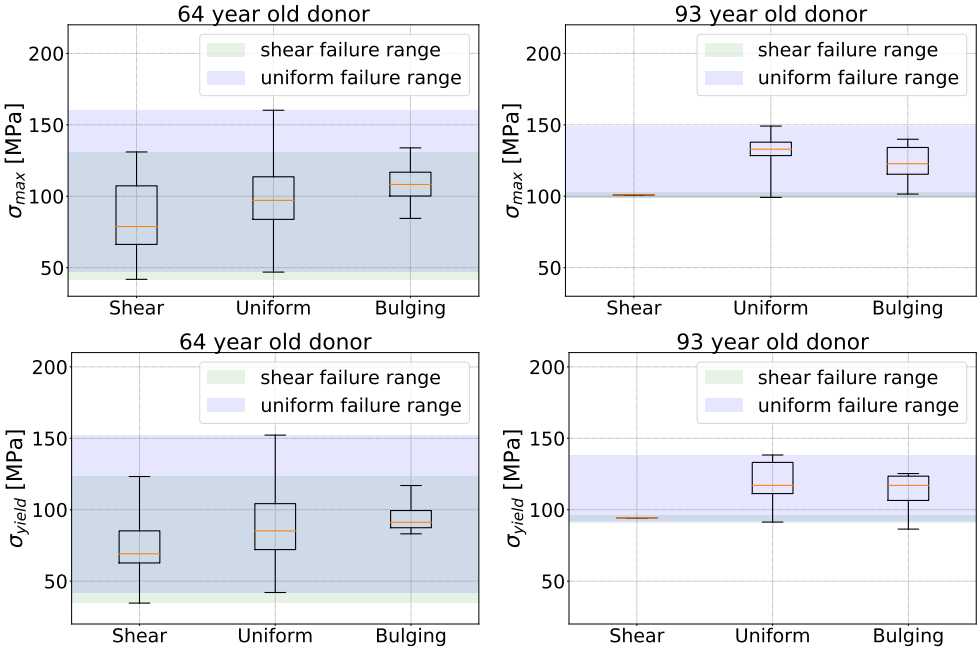

Figure 5.11: Stresses of osteons in failure mode groups

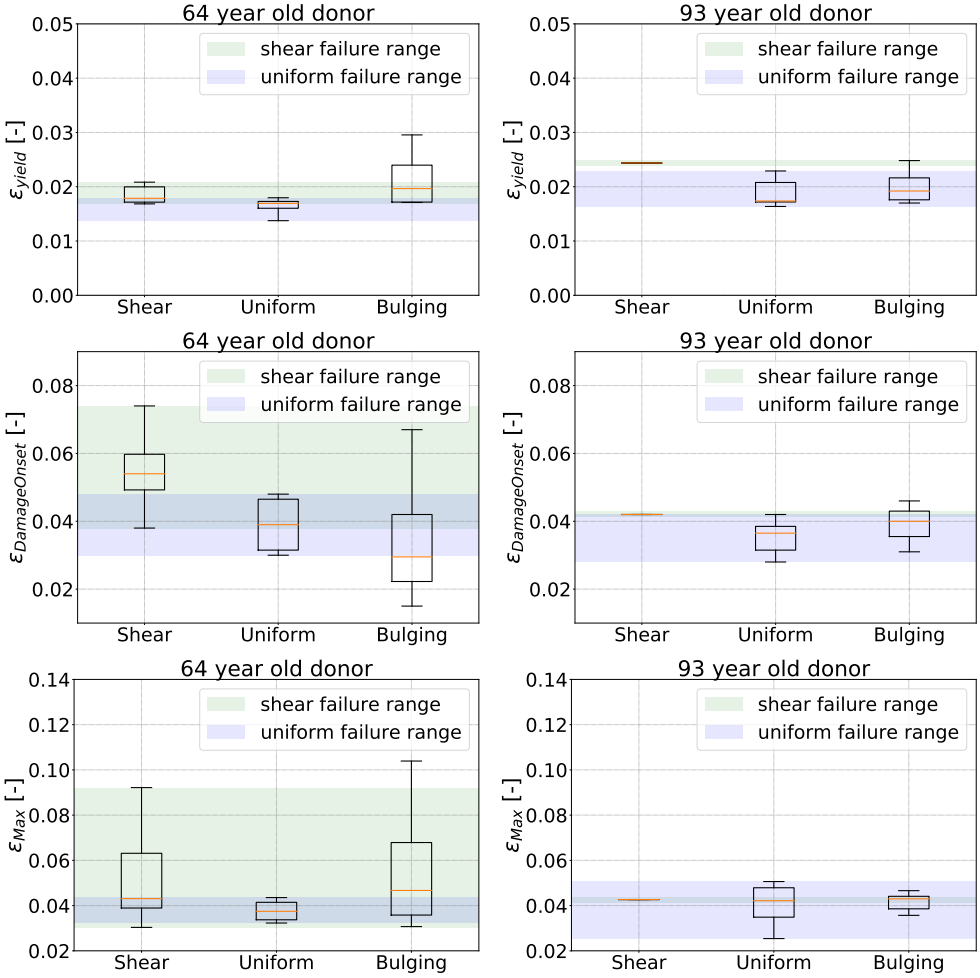

Figure 5.12: Strains of osteons in failure mode groups

5.3.3 Age vs structural and mechanical properties

In order to determine if there was a significant difference in mechanical and structural properties of osteons from two human donors aged 64 and 93 the measured data was statistically analysed. The histograms of the E, σ_{max}, σ_{yield}, ε_{yield}, BV/TV, BMD and *SHG intensity* data for the both human donors are presented in Figures 5.13, 5.14 and 5.15.

Either a one-way ANOVA test or a Kruskal Wallis H Test (KWHT) were used to determine if the mean value of a certain parameter from one donor was significantly different from the mean value of the same parameter from the other donor. The principle difference of the statistical analyses is that an ANOVA test compares two sets of normally distributed data with the same variance, whereas a Kruskal Wallis H Test can be used with heteroscedastic data since it compares the ranks of the data values and, therefore, is less accurate than ANOVA. A detailed information on the results of each step of the statistical analysis can be found in Appendix B and the results summary is given in Table 5.1.

One-way ANOVAs confirmed that the mean value of E and BMD of the older donor was higher than that of the younger donor with p values of 0.003 and 0.037, respectively. This correlated well with the previous observation that older osteons could withstand higher stresses. This observation was also confirmed by the KWHT since mean values of σ_{yield} and σ_{max} were found to be higher for the older donor (p=0.01 and 0.006, respectively). However, as seen from the histograms of the data, stress values of the younger donor may have appeared lower due to the higher variation of data. In the younger osteon set, there were osteons that experienced high stresses of over 100 MPa in addition to weaker osteons which failed at stresses as low as 20 MPa. This wide range of σ_{max} was not observed in the osteons of the older donor.

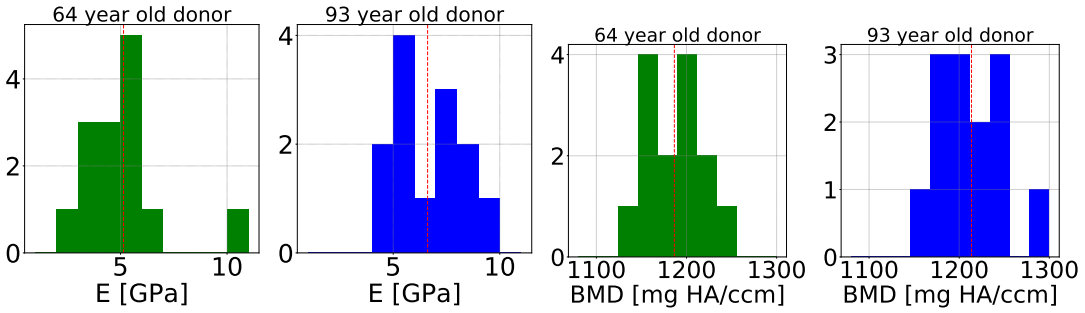

Figure 5.13: E and BMD values differ significantly for two donors 93 and 64 year old

Although the strain data sets were found to be not statistically different (p=0.286 for ε_{yield} and p=1.068 for ε_{max}), more osteons from the older donor seemed to yield at higher strains (greater than 0.02). This might be because of the accumulation of damage in the osteon during the loading in the elastic region. Remarkably, the histogram of the maximum strains shows that a number of osteons of the younger donor failed at a strain almost twice as high as the highest ε_{max} value of the older donor. This means that these young osteons had a distinctly high ductility.

The measured structural parameters did not show a significant difference between the age groups (KWHT, p>0.05). Bone volume and the Haversian canal size did not seem to significantly change with age, as represented by BV/TV. *SHG intensity* results implied that both bright and dark osteons were present in

both age groups. However, the higher mineralisation level of the dark osteons of the old donor may have caused them to fail in a brittle manner and not in the ductile manner as observed in the younger ones.

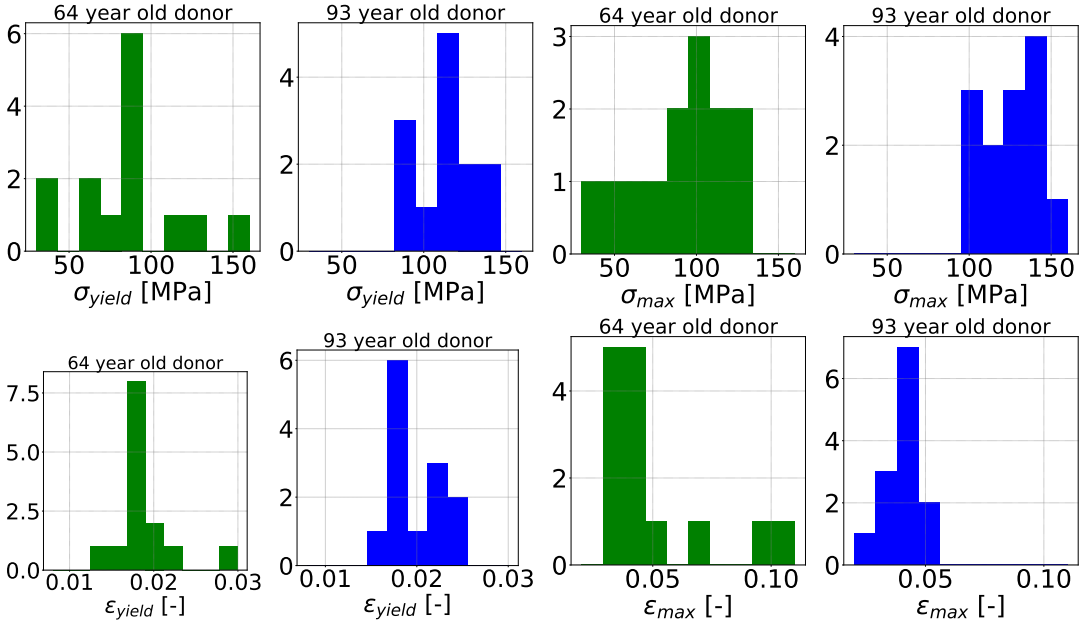

Figure 5.14: Histograms of stresses and strains for two donors 93 and 64 year old

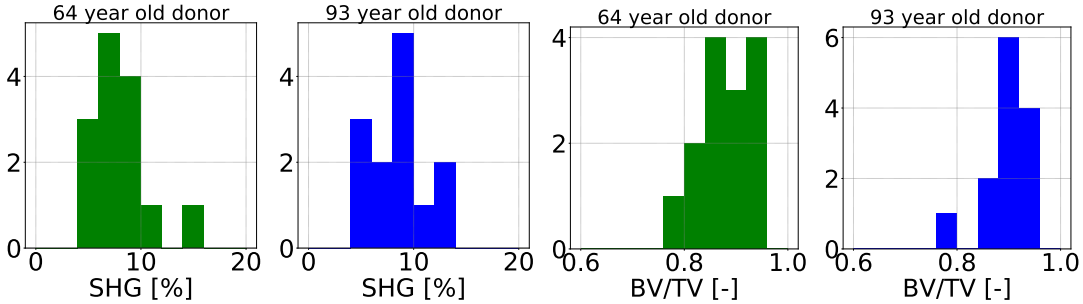

Figure 5.15: Histograms of osteonal structural parameters for two donors 93 and 64 year old

Mechanical property	donor - 64	donor - 93	p
E	**4.7** (1.1)	**6.6** (1.5)	0.003
σ_{yield}	**85.3** (29.9)	**113.9** (15.8)	0.006
σ_{max}	**96.1** (32.3)	**124.5** (15.7)	0.01
ε_{yield}	0.017 (0.0005)	0.017 (0.0020)	0.286
ε_{max}	0.040 (0.0097)	0.042 (0.0065)	1.068
Structural property			
BMD	**1186** (30)	**1214** (32)	0.037
BV/TV	0.88 (0.05)	0.89 (0.04)	0.217
$SHGintensity$	7.4 (1.5)	8.5 (2.8)	0.293

Table 5.1: Summary of the comparative statistical analysis

Further, a comparative statistical analysis was performed using only the data from the intact osteons to ensure that no internal flaws influenced the results of the comparison. As shown in Table 5.2, the p values of each parameter were lower than the significance level, suggesting that no significant difference could be detected between the donors. However, the small sample size of intact osteons from each donor (n=5) resulted in a low statistical power for the comparison (F). Thus, the differences observed between the groups were not detected by the statistical analysis. The F values were calculated for the data with the use of Altman's nomogram. For ε_{yield}, the non parametric Mann–Whitney U test was used, and the remaining data was analysed with the one-way ANOVA.

Nonetheless, the same trends of higher values of E, σ_{yield}, σ_{max} and BMD for the older donor found in the complete dataset were observed in the intact osteon subset.

Mechanical property	donor - 64 - intact osteons	donor - 93 - intact osteons	p	F
E	6.2 (2.5)	7.3 (1.6)	0.492	0.10
σ_{yield}	91.2 (39.5)	118.6 (16.3)	0.211	0.25
σ_{max}	100.3 (40.2)	130.1 (15.4)	0.180	0.30
ε_{yield}	0.017 (0.0008)	0.017 (0.0008)	0.201	0.25
ε_{max}	0.037 (0.005)	0.040 (0.009)	0.629	0.08
Structural property				
BMD	1169 (26)	1199 (26)	0.146	0.35
BV/TV	0.88 (0.07)	0.89 (0.05)	0.780	0.05
$SHGintensity$	7.4 (1.3)	8.5 (2.8)	0.532	0.10

Table 5.2: Summary of the comparative statistical analysis of intact osteons

5.3.4 Predictors of osteonal mechanical properties

As described in the previous section, osteons from two age groups only significantly differed in the level of mineralisation. In order to identify if any of the measured structural parameters could predict the mechanical behaviour of the osteons, regression analyses were conducted on the continuous loading data from the two age groups. Out of the measured parameters, BV/TV and *SHG intensity* were found to correlate significantly with mechanical properties of osteons. BMD, notably, did not have an direct effect on the mechanical properties of the osteons.

Despite the low values of goodness of fit ($R^2 = 0.39 - 0.75$), p values of no greater than 0.02 speak for the high significance of the results. As shown in Figure 5.16, orientation of mineralised collagen fibres significantly correlated with yield strain ($R^2 = 0.39$, $p1 < 0.05$, $p2 < 0.05$) for the younger donor, which may mean that transverse (bright) osteons tend to be more ductile than longitudinal (dark). BV/TV predicted E, σ_{yield} and σ_{max} ($R^2 = 0.53$, $R^2 = 0.68$, $R^2 = 0.75$, respectively, $p1_{all} < 0.05, p2_{all} < 0.05$). This may mean that collagen volume, size of the haversian canal, lacunar spaces or spaces between lamellae sheets have a significant effect on the stresses experienced by the osteon as well as on its elastic modulus, which is a critically important parameter for engineering. Knowing what particular parameter or the combination of them, reflected in this study by BV/TV, effects the elastic moduli of the osteons has the potential to increase the accuracy of computational modelling of cortical bone. Currently, cortical bone is treated as homogeneous material, whereas the results of this study suggest that

it should be treated as a heterogeneous material.

For the older donor, however, mechanical properties were predicted by collagen fibre orientation only, as shown in Figure 5.17. σ_{yield} and σ_{max} were effected by BV/TV in the younger donor, these properties correlated better with the *SHG intensity* in the older donor ($R^2 = 0.43$, $R^2 = 0.54$, $p1_{all} < 0.05, p2_{all} < 0.05$). The absence of the BV/TV effect may be explained by the overall increased level of mineralisation of the older osteons. It can be speculated that overly mineralised collagen fibres could have impaired the structure of collagen molecules and therefore lower the effect of collagen on mechanical properties of osteons. Inter-lamellar spaces may have also contributed or been a consequence of the impaired collagen function. A change in lacunar size would lead to redistribution of bio-mechanical signals to Osteocytes within lacunae and, therefore, retarded or inhibited remodelling processes.

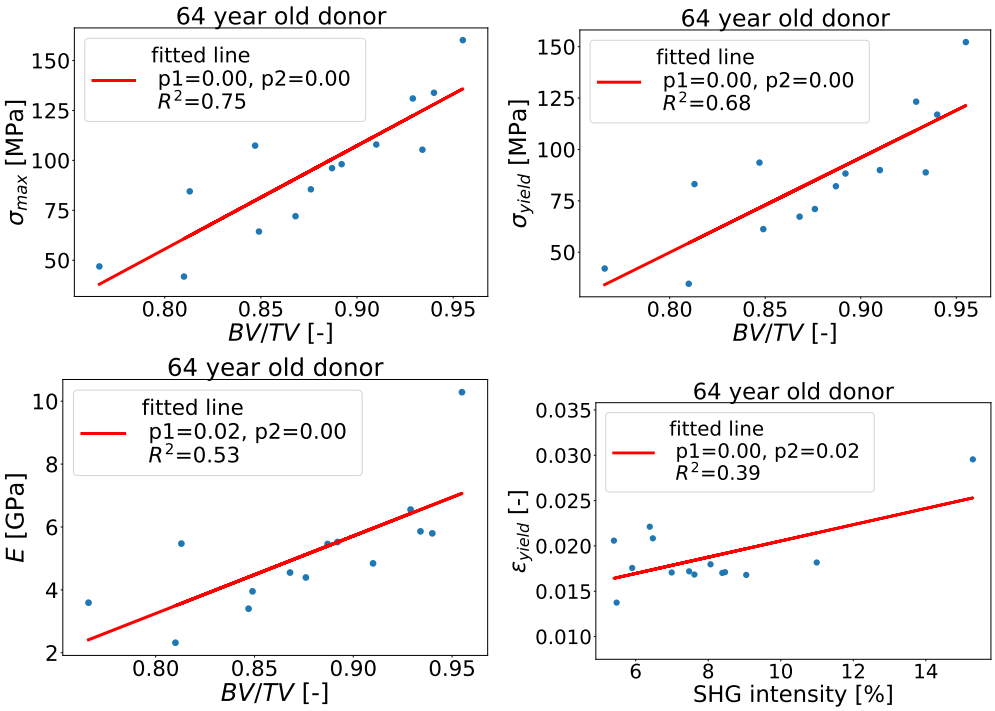

Figure 5.16: For the younger donor BV/TV was a significant predictor of σ_{max} ,σ_{yield} and E and SHG intensity was a significant predictor of ε_{yield}

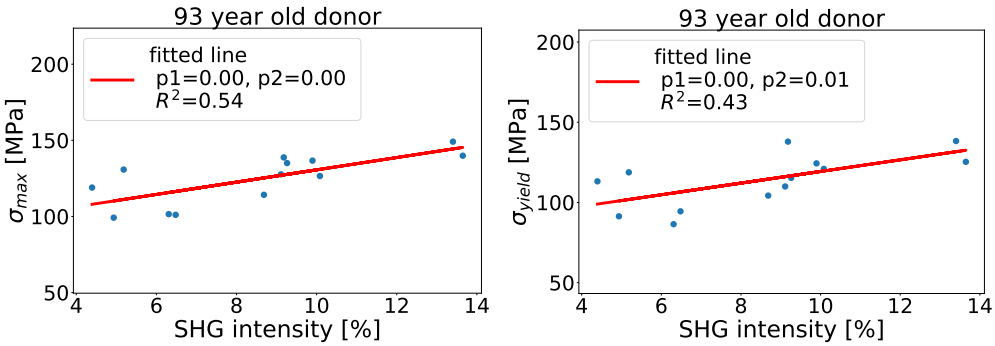

Figure 5.17: For the older donor SHG intensity was a significant predictor of σ_{max} and σ_{yield}

5.3.5 Outliers profiles

Outliers in the data represent osteons in the set with the values of a certain property that deviate significantly from the median value within the group. Outlier values were not used for the comparative statistical analysis of the age groups, however attention to these osteons should be paid to understand what could cause such distinct mechanical behaviour. Older donor data did not contain outliers. For the younger donor, two such specific osteons were detected, #5 and #10.

Osteon #10 (Figure 5.18 left) had a notably high E of 10.3 GPa , whereas the group mean was 4.7 GPa, and BV/TV, BMD, *SHG intensity* values were all higher than the corresponding mean values. This means that the orientation of the collagen fibres was mostly transverse. The high value of mineralisation of 1193 mg HA/ccm for the younger donor was still lower than the mean BMD value of the older group. High BV/TV values correspond to a smaller size of Haversian canal and a lower proportion between mineral and non-mineral volume fractions of the osteon.

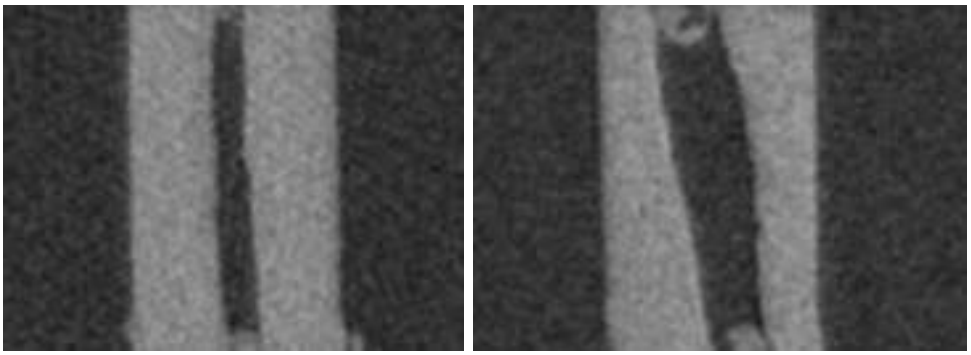

Figure 5.18: Osteon #10 (left) and #5 (right): CT scans of the frontal plane

Osteon #5 in set-9 (Figure 5.18 right) had three distinct properties. This osteon had the highest values of ε_{yield}, ε_{max} and *SHG intensity* in the younger osteon group. As the "brightest" osteon in the set with a rather wide Haversian canal and low mineralisation level of 1179 mg HA/ccm, this osteon yielded at 3%, whereas the stiffest osteon, #10, yielded at 1.7%. This implies that already within the apparent elastic region damage accumulated differently for both outlier osteons. Predictably, osteon #10 accumulated visible damage and failed at substantially lower strains.

The following questions arise: Do these two osteons have different damage accumulation mechanisms that lead to the differences in yield and maximum strains? Since both osteons are bright osteons, are these different mechanisms effected by mineralisation? Does size of Haversian canal play a role?

Osteon #5, bright and with lower mineral content showed characteristically ductile behaviour with failure occurring at a relatively high strain and lower stress (Figure 5.19 left). In contrast, stiff osteon #10, bright but with high mineral content, withstood higher stresses and failed in a uniform mode at lower strains (Figure 5.19 right). It is very likely that the presence of such ductile osteons as osteon #5 in the younger bone contributes to its higher toughness, whereas the absence of such in the older bone leads to its increased fragility.

Structural and mechanical properties of the two outlier osteons are summarised in Table 5.3.

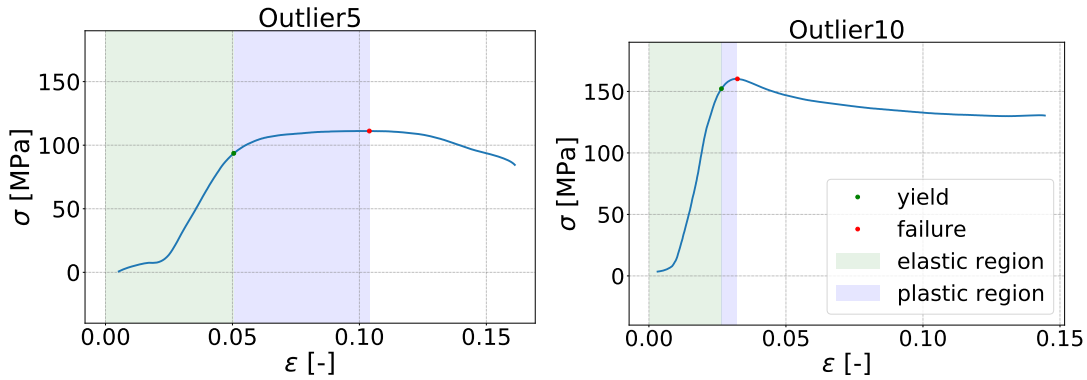

Figure 5.19: Stress-strain curves of outlier osteons

Property	Mean value	Osteon #5	Osteon #10
E	4.7	3.4	10.3*
ε_{yield}	0.018	0.030*	0.017
$\varepsilon_{DamageOnset}$	0.041	0.067	0.030
ε_{max}	0.049	0.104*	0.032
failure mode	-	bulging	uniform
σ_{max}	95.4	107.4	160.2
σ_{yield}	85.3	93.6	152.2
BV/TV	0.88	0.85	0.95
BMD	1186.5	1179.4	1193.7
SHG intensity	7.4	15.3*	9.0

Table 5.3: Mechanical and structural properties of outliers. (*) indicates the greatest value of a certain parameter within the age group

5.3.6 Geometry effects

Regression analyses (Figure 5.20) suggest that there was a correlation between aspect ratio of the tested osteons and the σ_{max} ($R^2 = 0.37$ p=0.00). The osteons with the lower aspect ratio tended to withstand higher stresses. σ_{yield} and E had less significant correlation with the aspect ratio of osteons ($R^2 = 0.33$ p=0.00 and $R^2 = 0.19$ p=0.02), and ε_{yield} did not correlate with aspect ratio ($R^2 = 0.07$ p=0.19).

Low values of p suggest that the chosen aspect ratios for the samples may influence the results of compression testing. Further, end effects of compression testing might influence osteons with a low aspect ratio. As mentioned in Appendix A, osteons with a high aspect ratio of 4 were influenced by structural instability resulting in buckling. To evaluate how the micro-geometry of the samples effect their mechanical properties further studies should be conducted.

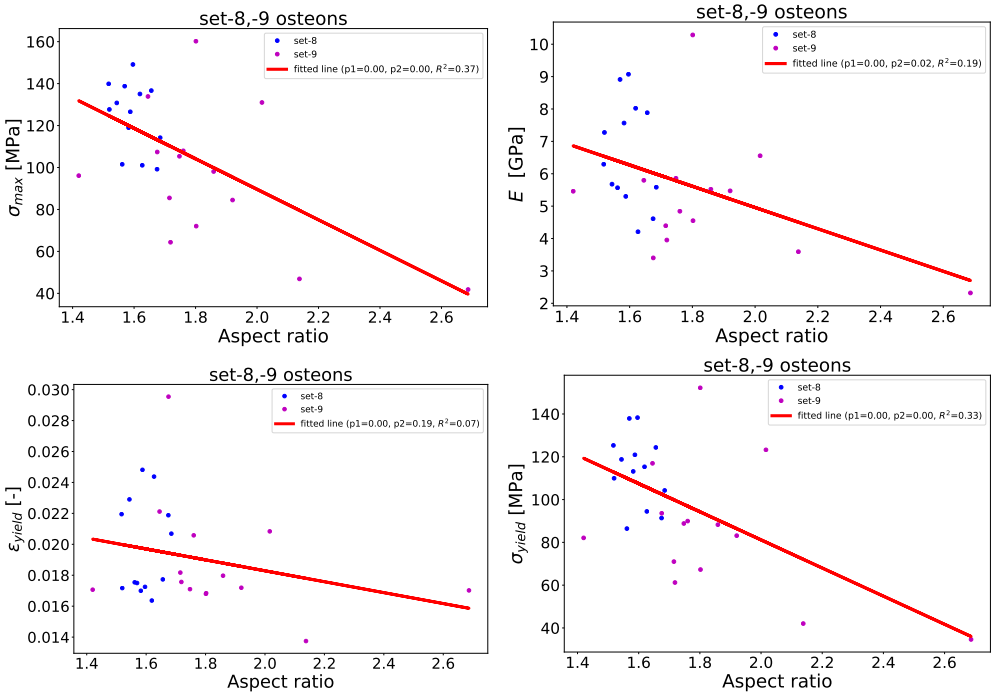

Figure 5.20: Correlation of σ_{max}, σ_{yield}, ε_{yield}, E with the aspect ratio of the osteons

5.4 Step-wise compression of osteons

Six osteons from both human donors were tested in compression with a step-loading profile. As was mentioned in the introduction, step-loading protocols are used to assess the "true" elastic modulus of bone. At least two loading-unloading cycles were fitted within the elastic region of the stress-strain curve.

The results of the step-loading tests are presented in Figure 5.21; from the graph it is evident that the elastic modulus of the "unloading" segment of the curve is consistently greater than of the "loading" segment. This may be due to accumulation of damage in the osteonal structure within the apparent elastic loading region. As the visible damage accumulated after the osteons had yielded, the "invisible" damage in the elastic region must have happened at a lower level of the hierarchical structure. Stresses experienced by bone in its elastic mode are physiological loads, and accumulation of damage in osteons may be the initiator of the remodelling processes in bone. Since osteons can act as a type of diffuse damage collection zone, the loss of an osteon's ability to accumulate such damage may result in initiation of microcracks within interstitial bone when subjected to higher strains and lead to increased fragility of bone overall. Older bone has been reported to accumulate less diffuse damage when compared to younger bone [74].

Higher values of elastic modulus in the unloading mode indicate that the values reported by Ascenzi et al. (1968) are underestimated. In fact, the elastic moduli of osteons were found to be from 15 to 167% higher than what had previously been reported. This observation shows an important trend, but exact conclusions can not currently be drawn due to the limited number of samples tested.

The comparison between the elastic modulus values from the loading and unloading curves are presentaed in Table 5.4.

Osteon	E^{load}_{mean}	E^{relax}_{mean}	% increase
set8, 1	9.01	16.97	88.34
set8, 3	23.71	27.44	15.72
set8, 7	9.56	16.41	71.54
set8, 10	12.14	19.77	62.74
set8, 14	9.78	14.88	52.13
set9, 1	3.93	10.52	167.68

Table 5.4: Elastic modulus values from the loading and unloading curves of compression testing

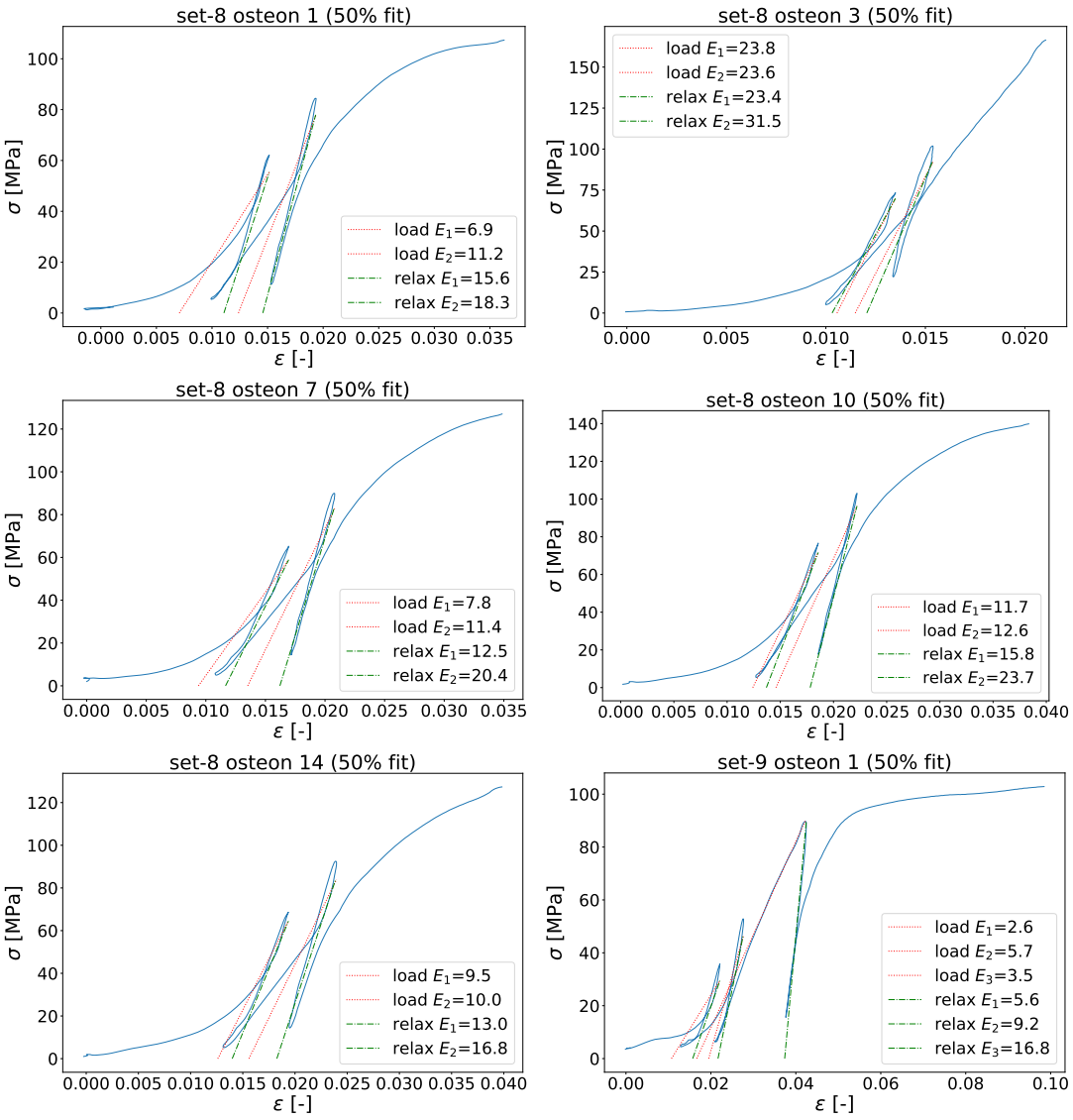

Figure 5.21: Stress-strain curves of a step-loading compression tests on osteons in set-8 and -9

5.5 Summary

The effect of age on human osteonal mechanical properties was investigated. For this purpose, a number of individual osteons were obtained from two male donors of different ages. Harvested and stored in the same conditions, the osteons were subjected to continuous and step-wise compression testing. Under compression, osteons were observed with a camera-microscope.

Three types of osteon failure were identified. Samples failed in shear, uniformly or in bulging. Osteons that fail in shear were characterized as ductile and the crack propagated through the lamellae sheets. For the uniform failure, cracks seemed to propagate along the principal stress axis between the lamellae sheets, this type of failure was characterised as quasi brittle. Bulging was treated mostly as a structural instability, rather than a failure mode, due to a high number of external influencing factors that could have resulted in redistribution of stresses and thus localisation of damage. Older osteons failed mostly in a brittle manner. The younger osteons showed higher variation in failure modes, and a number of osteons failed in a ductile manner.

Morphology of osteons was found to have an effect on the failure mechanism, but did not predefine it. Further, BV/TV, BMD, *SHG Intensity* did not show significant correlations with failure mode. This indicates that a number of intrinsic factors not investigated in this study influence osteon failure.

Mechanical properties of osteons that failed in shear differed from the mechanical properties of osteons that failed uniformly. Shear failure osteons were found to be more ductile with a lower elastic modulus, whereas uniform failure osteons had higher values of elastic modulus and were more brittle. Similarly for both age groups, shear failure happened in a lower range of stresses of up to 120 MPa at higher strains. Uniform failure had a wider range of stresses reaching 150 MPa, but lower strains. Osteons of the older donor predominantly experienced uniform failure, whereas osteons of the younger donor failed uniformly and in shear. Thus, it can be concluded, that mechanical properties of the older osteon set diverged from the younger osteon set. E, σ_{yeild} and σ_{max} of the older osteon set were found to be higher than those of the younger osteon set ($p<0.05$), which might be explained by the presence of the stiffer more mineralised osteons ($p<0.05$) and the absence of the weaker and more ductile osteons in the older set.

Despite the fact that the two age groups structurally differed in mineral content only, BMD was not found to be a predictor of any osteonal mechanical property (regression analysis, $p>0.05$). For the younger donor, BV/TV significantly predicted E, σ_{yeild} and σ_{max}. *SHG intensity* was a significant predictor of yield strain. For the older donor, however, the *SHG intensity* had a greater effect on σ_{yeild} and σ_{max}, while the effect of BV/TV may have been impeded by the higher mineralisation.

The step-wise compression testing data was evaluated and it was concluded that damage accumulates in osteons during compression testing prior to yielding, i.e. within the elastic region. Elastic moduli measured during loading and relaxing were compared and it was found that the values differed by up to 167%. This shows that the values reported by Ascenzi et al. for the osteonal elastic modulus are greatly underestimated.

Two osteons from the young donor were described as characteristic examples of ductile and brittle behaviour. The bright, lower mineralised, "ductile" osteon had a 43% higher ε_{yeild}, 55% higher $\varepsilon_{DamageOnset}$ and 69% higher ε_{max}. The bright,

higher mineralised, "brittle" osteon withstood a 38% higher σ_{yield} and 33% higher σ_{max}.

The impact of geometry effects was discussed. Low aspect ratios of samples may lead to end effects and high aspect ratios may lead to buckling. However, to establish exact correlations further experiments should be done.

The main limitation of this study was that data from only two donors were compared. To obtain more accurate information on the effects of age further research with a larger number of donors must be conducted. A number of improvements can be made to obtain more precise data, including increasing the number of samples per donor, using multiple cameras to track osteonal failure, optimizing the surface coating on the test-setup to reduce the incidence of end effects, using a higher resolution uCT scanner and reducing noise in the measured data. However, the observations made in this study may be used as valuable insights into the biomechanics of individual osteon and, can provide the directions for future research.

Traditionally, cortical bone, in an analogy to engineering materials, was regarded as a fibre reinforced material. Osteons were viewed as stiff rods providing the strength to the material. This study suggests that the stiff rod phenomenological model is only part of the truth. There are not only stiff osteons providing strength but also "weak" osteons proving ductility and, therefore, overall toughness. The absence of the weaker osteons in older bone may lead to fragility. If there are no ductile osteons to dissipate energy of impact, cracks may more easily propagate, resulting in bone fractures.

In conclusion, it was confirmed that age affects the fracture mechanisms and mechanical properties of osteons. Osteon set from the older bone had a higher elastic modulus and experienced more brittle type of failure due to the lack of "ductile" osteons, that were present in the younger bone osteon set. Weak, more ductile osteons may act as stress accumulators in younger bone. By accumulating damage within them, they may prevent the formation of larger cracks in interstitial bone and, therefore, contribute to the higher toughness of younger bone. It was also confirmed that the elastic modulus values reported by Ascenzi are underestimated. Elastic moduli of osteons in relaxation was 5-167% higher than in compressive loading. This shows that internal sub-micro damage accumulates in osteons within elastic region.

Overall, osteons were identified be to mechanically and structurally diverse. Investigating their differences may be the key to a better understanding of bone ageing and pathological processes.

Chapter 6

Conclusion

In this thesis, a procedure to harvest single osteons from the bulk material of bone was developed. A CNC-system was modified to house an optical system, which enabled the accurate positioning of the spindle above the targeted osteon. To mill the targeted osteon out of the bone tissue, custom-made eccentric drill-bits were designed and fabricated.

A total number of 128 osteons with diameters of 180-350 μm were milled out. The total number of osteons included 51 bovine and 77 human osteons. The human osteons were obtained from two male donors aged 64 (n=18) and 93 (n=59). The bovine osteons were primarily used for establishing and refining a compression testing procedure. A compression testing set-up was designed and effectively used to measure mechanical properties of the harvested osteons, both bovine and human. Structural properties of the harvested osteons were evaluated using μCT and an SHG microscope.

For the osteons in uni-axial continuous compression testing, three modes of failure were observed. These modes included shear failure with a single slip plane, uniform compression failure and bulging failure.

In order to identify if any of the measured structural properties could be a potential predictor of osteonal mechanical strength, regression analyses were conducted on the measured bovine and human data. On the human osteon data, ANOVA was used to determine if age had an effect on mechanical and structural properties.

These objectives were put forward due to the need to fundamentally understand bone structure, how it changes with age, and to possibly identify a structural parameter of osteonal bone that may correlate with mechanical properties of osteonal bone. Over the recent decades it became clear that the existing clinical methods fail to adequately diagnose patients with risk of pathological fractures. Currently, BMD is the predominant clinical metric used to determine bone quality. Annually increasing numbers of pathological fracture incidence underlines the urgent need for development of new methods to asses bone quality. The osteon, as a functional unit of cortical bone, plays a major role in the load bearing capacity of the skeleton. Importantly, the osteon is the structural element forming during bone remodelling. Therefore, changes in osteonal mechanical properties may potentially reflect the changes in bone occurring with ageing. From the engineering point of view, osteons can be regarded as fibre reinforcement for bone at the tissue level. However, the mechanical and structural properties of individual osteons are underinvestigated. An understanding of mechanical behaviour and fracture mechanisms of osteons could provide essential insights into fracture

at the whole bone level and the mechanism of bone ageing. In this context, probing the mechanics of individual osteons could help to develop new effective approaches for diagnosis and treatment of bone diseases.

In this thesis, BV/TV and *SHG intensity* were the only structural parameters to significantly correlate with the mechanical properties of osteons. The results of this analysis suggest that, on the osteonal level, collagen fibre orientation and the osteonal geometry and porosity correlate stronger with mechanical bone strength than BMD. E, σ_{max} and σ_{yield} were found to differ between two sets of osteons from the 93 and 64 year old donors. The E, σ_{max} and σ_{yield} of osteons from the 64 year old donor was significantly lower than the those of the osteons from the 93 year old donor. However, comparative statistical analysis of the osteons without morphological imperfections did not detect significant differences between the donors, most likely, due to the low number of samples and, therefore, low power of the statistical analysis. Nevertheless, higher variation of osteonal structural and mechanical parameters was clearly present for the younger donor. Three modes of osteonal failure were identified in this thesis. For the older donor, osteons failed less in shear and more uniformly, whereas, for the younger donor, all three types of failure occurred. Osteons that failed in shear tended to have higher range of strains and lower range of stresses that those that failed uniformly. Further, the results of the step-wise compressions testing suggested that the values of elastic modulus found from the uni-axial compression testing are likely to be up to 1.7 times underestimated.

During this master's project, a few limitations of the test setup and testing procedure were identified. A more precise system for machining the drill-bits would decrease the time spent on production of a single drill-bit, as well as enable the operator to produced drill-bits of desired geometry with less effort. To improve the durability of a single produced drill-bit, a new material that is less prone to becoming blunt should be used. Concerning the mechanical testing system, the compression-cylinders should be tapered to a diameter comparable to that of a single osteon and an optical system for the manual placement of osteons on the compression platens should be incorporated into the "Thelkin" system. This would improve the visibility of osteons, as well as allow for an accurate placement of osteons along the axis of compression. The developed procedure for harvesting and compression testing of osteons has proven to be effective and, with a few minor improvements, can be used in future micro-mechanical research.

In summary, bone is a highly complex material and this project provided a number of insights into its structure. Age was found to correlate with mechanical properties of osteons. Mineralised collagen bundle orientation and bone volume to tissue volume ratio were found to significantly predict the mechanical properties of osteons. These two findings suggest that future research into determinants of bone quality should pay equal attention to collagen and mineral at the osteonal level in bone and, in particular, to the orientation of the mineralised collagen bundles. It may be, that the function of the osteonal structure is to accumulate damage and dissipate the fracture energy, hence contributing to the overall toughness of bone. Investigating osteonal fracture mechanisms within an apparent elastic region might give us a better understanding of the function that osteons fulfil in bone under physiological loading.

Appendix A

Optimization of uniaxial compression testing of individual osteons

A.1 Introduction

With the procedure described in section 3, osteons were produced and grouped in "sets". Osteons within one set were cored out from one bone cross-section, with one drill-bit of a certain diameter, on one day and were stored and tested in the same conditions. Throughout the project, the procedure had to be adjusted and improved and therefore each set of osteons was produced, stored and tested differently. Since bone is a living tissue, storage and testing conditions can have a strong effect on the measured mechanical properties of bone. Therefore, osteons from different sets were assumed to possibly have different mechancial properties and are referred to in this thesis separately. Produced sets of osteons and the mechanical tests are chronologically described in this chapter. The given information is then summarised in sections A.3.2 and A.3.4.

A.2 Research objectives

The research objective described in this chapter was the optimization of manufacturing, storage, and testing protocols.

A.3 Chronological description of osteon sets and compression testing

A.3.1 Description of compression tests on bovine osteon sets

A total number of 61 bovine cylinders were produced, 10 of which had diameter exceeding $400\mu m$ and were therefore excluded from mechanical testing. The remaining osteons (n=51) were divided into three sets with aspect ratios of 5, 1.7 and 1.8.

Compression tests on bovine SET-1

Bovine set-1 had a total number of 14 osteons, 7 of which were tested in compression. The osteons in bovine set-1 had an aspect ratio of 5 (height H_{set-1}

of 1034.55 μm [stdev 53.55], diameter D_{set-1} of 205.45 μm [stdev 16.47]) and BV/TV ranged from 80.6% to 97.4 % with a mean value of 91.9 % [stdev 5.2]. Strain rate for the compression test was set to 0.005 [1/s]. During mechanical testing 4 out of 7 samples experienced buckling. In Figure A.1, sequential images captured during a compression test in which no buckling occurred are presented. Figure A.2 presents sequential images of an osteon which experienced buckling during compression testing. No mechanical properties of osteons in set-1 were calculated because of the observed buckling. It was, therefore, established that the aspect ratio of 5 was too high, as compression tests had resulted in buckling. For the future tests the reduced aspect ratio was planned in order to prevent bucking.

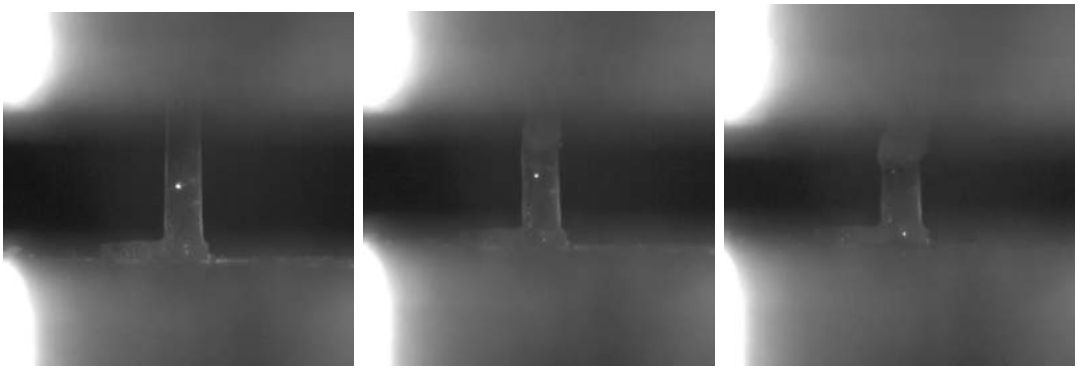

Figure A.1: Images captured during the compression test on sample # 5 in set-1 without buckling

Figure A.2: Images captured during the compression test on osteon # 7 in set-1 with buckling

Compression tests on bovine SET-2 and SET-3

Of the 31 cylinders sorted into set-2 and set-3, 3 were discarded; one cylinder did not contain a centred osteon and two cylinders were lost during placement in the compression test setup. Aspect ratios of osteons in sets-2 and set-3 were 1.7 and 1.8 respectively. Dimensions of the set-2 and set-3 osteons subjected to mechanical testing are summarized in Table A.1. Osteons in these sets were divided into three principal groups based on their geometry: group B without a base-plate, *bp*, (n=13), group C with a centred *bp* (n=12) and group D with the off-centred *bp* (3 samples) (Figure A.3). The thickness of the bp ranged from 56 μm to 113 μm and, in some cases, took up to 23% of the height of the set-2 and set3 osteons.

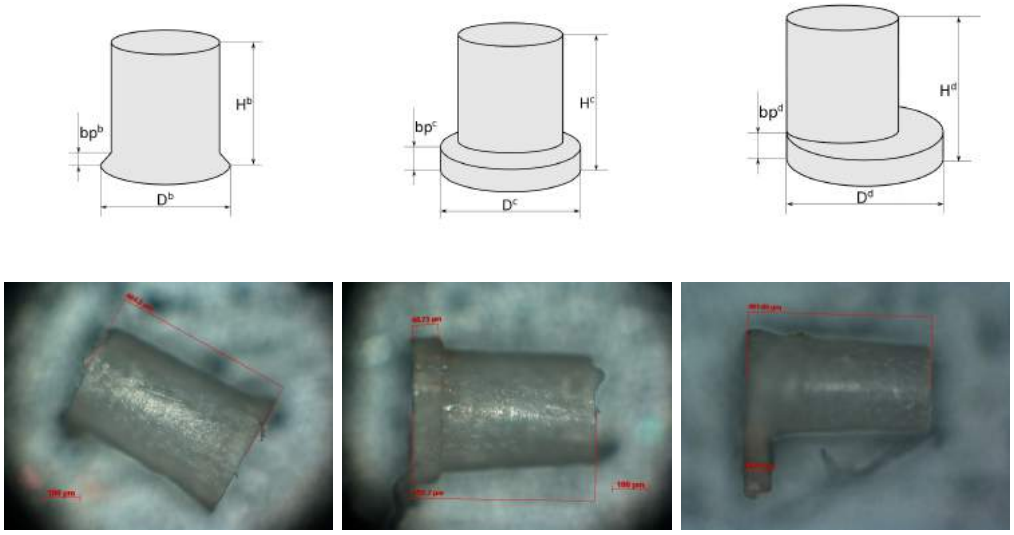

Figure A.3: Diagrams (top) and images (bottom) of osteons from the three principal groups A (left), B (center), and C (right) in set-2 and set-3

Compression testing of the set-2 osteons was performed in distilled water with a strain rate of 0.01 $[s^{-1}]$. It was determined that using the cross-head displacements of the Thelkin machine resulted in overly compliant osteons. Therefore, a video tracking method was implemented to measure the "true" displacement of the osteon during testing.

For set-3, evaluation of the μCT data revealed highly-branching osteonal structures (Figure A.4). The following structural parameters were measured:

- BV/TV values for set-3 ranged from 89.1% to 97.2 % with a mean value of 95.0 % [stdev 2.5 %],
- BMD ranged from 1136.24 to 1236.85 $mgHA/ccm$ with a mean value of 1186.55 $mgHA/ccm$ [stdev 29.63],
- Inclination angle ranged from 1.00 *degree* to 21.15 *degrees* with a mean value of 11.26 *degrees* [stdev 6.47].

Set-3 osteons were tested in HBSS (pH 7.4) with a strain rate of 0.005 $[s^{-1}]$ (Figure A.5). HBSS was chosen rather than water to better reflect conditions in

vivo. The values for displacement were deducted from the video feed. With a regression analysis with the structural parameters as predictors and mechanical properties as dependent variables. It was possible to predict osteon mechanical properties using BV/TV, as described in chapter 4. It was, further, determined that the compression setup needed to be redesigned for better optical documentation.

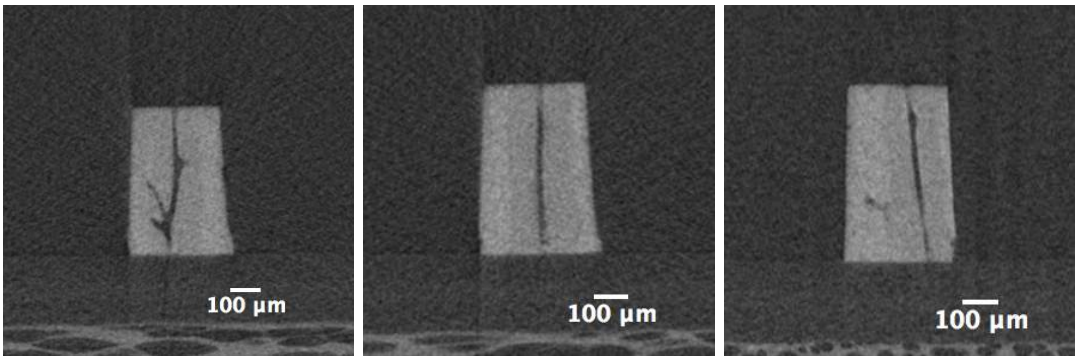

Figure A.4: μCT scan images of the osteons #4 (left), # 6 (centre) and #12 (right) in set-3

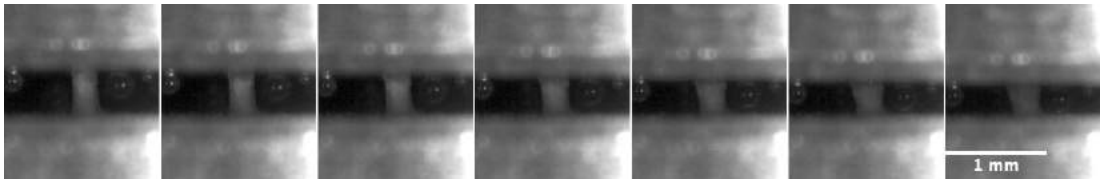

Figure A.5: Sequential images from the compression test of osteon # 8 in set-3, frames from the left to the right correspond to displacements from 0.028 to 0.2 mm with increments of 0.028 mm

A.3.2 Summary of the experiments on bovine samples

Bovine bone was primarily used for the trial experiments, it was possible to successfully extract osteons from the bovine bone cross-sections and test them in uni-axial compression. To obtain the true values of strains visual documentation of the compression tests was introduced. It was established that the aspect ratio of osteons did not have to be 5 or higher, otherwise during compression buckling occurred. However for the further tests on human osteons the existing compression setup had to be modified to make the osteons visible under compression and observe the occurring damage process. Also an approach to eliminate the thin plate at the base of the osteons had to be found.

Geometric and structural parameters of bovine osteons are summarised in Table A.1. Compression testing conditions for each bovine set are detailed in Table A.2.

	H [μm]	D [μm]	aspect ratio	BV/TV [%]	BMD [mg HA/ccm]	Storage
set-1	1034.55 [53.55]	205.45 [16.47]	5	80-97	-	in water (0C)
set-2	484.83 [5.68]	288.89 [5.45]	1.7	-	-	in water (0C)
set-3	499.42 [6.21]	286.83 [25.79]	1.8	91-97	1168.58 [50.86]	in water (0C)

Table A.1: Bovine osteon description

	tested in	strain rate
set-1	water	0.005
set-2	water	0.01
set-3	HBSS	0.005

Table A.2: Description of compression testing conducted on bovine osteons

A.3.3 Description of compression tests on human osteons

A total number of 77 human osteons was produced and divided into 6 sets. Sets-4, -5, -6, -7, and -8 were obtained from the 93 year old human donor and set-9 was obtained from the 64 year old donor.

Compression tests on human SET-4

The osteon aspect ratio, testing protocol, and new fixture were optimized with bovine experiments. The set-4 was the first human osteon set, that was produced and tested with the developed procedure. The human set-4 consisted of 20 osteons, two of which were lost during placement in the testing set-up. Osteons were stored in water at 0 C before testing. The osteons in set-4 had an aspect ratio of 2.3, H_{set-4} of 534.05 μm [stdev 18.66] and D_{set-4} of 240.84 μm

[stdev 10.65]. As in the bovine set-3, osteons in set-4 had a thin *bp* (Figure A.6) and were divided in the same principal geometry groups A, B and C.

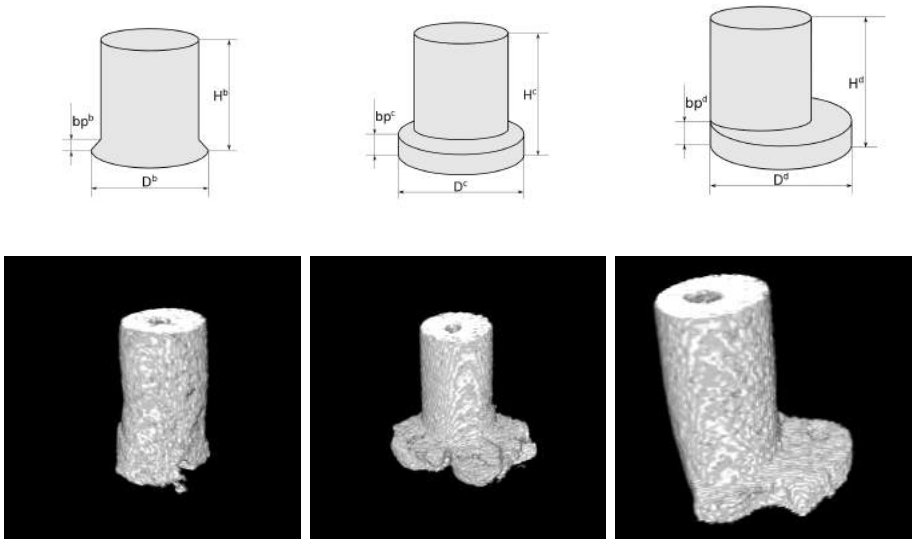

Figure A.6: Diagrams (top) and reconstructed μCT images (bottom) of human osteons in set-4 from the three principal groups A (left), B (centre) and C (left).

The μCT data was used to verify that all of the cylinders contained a centred osteon. Additionally, the human osteons were observed to contain little to no branching compared to the bovine osteons. The following structural parameters were measured:

- BV/TV ranged from 72 to 95% with a mean value of 87% [stdev 6],
- Inclination angle ranged from 0.00 to 26.00 *degrees* with a mean value of 7.31 *degrees* [stdev 6.69],
- BMD ranged from 1222.48 to 1380.57 $mgHA/ccm$ with a mean value of 1276.18 $mgHA/ccm$ [stdev 40.34].

The new compression testing fixture was installed and tuned. Compression testing on set-4 was performed in HBSS with the strain rate of 0.0025 s^{-1}.

Compression tests on human SET-5

Consisting of 6 osteons, set-5 was stored in water at 0 C and used for trial step-loading tests. The step-loading curve was developed such that 2-3 loading-unloading cycles occurred within the linear portion of the force-deflection curve. The step-loading profile is described in section 3. The osteons in set-5 had an aspect ratio of 1.6, H_{set-5} of 341.50 μm [stdev 11.50] and D_{set-5} of 215.44 μm [stdev 3.49]. The following structural parameters were measured:

- BV/TV ranged from 92 to 95% with a mean value of 94% [stdev 1],
- Inclination angle ranged from 7.13 to 18.13 *degrees* with a mean value of 12.63 *degrees* [stdev 5.50],

- BMD ranged from 1193.73 to 1251.22 $mgHA/ccm$ with a mean value of 1222.48 $mgHA/ccm$ [stdev 28.74],

During compression testing significant dulling of the drill bits was noticed. A sharpening procedure was developed which resulted in elimination of the base. plate.

Compression tests on human SET-6 and SET-7

For production of set-6 through set-9, the sharpening procedure, described in section 3.4.1, was implemented. As a result, the *bp* on osteons in sets -6,-7,-8 and -9 was eliminated (figure A.7).

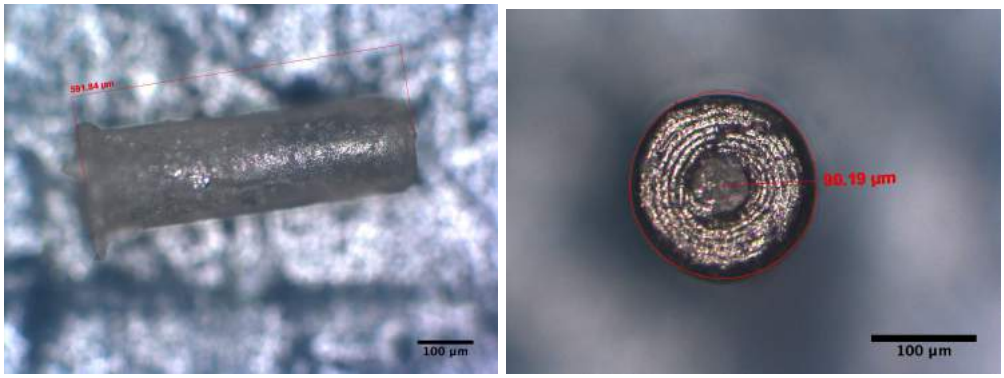

Figure A.7: An osteon from set-7, longitudinal (left) and transverse (right) planes

Set-6 included 20 osteons. They were stored in water at 0 C before testing. The osteons in set-6 had an aspect ratio of 1.8, H_{set-6} of 507.83 μm [stdev 10.30] and D_{set-6} of 291.59 μm [stdev 56.31]. The following structural parameters were measured:

- BV/TV ranged from 83 to 97% with a mean value of 91% [stdev 5],
- Inclination angle ranged from 0.04 to 11.95 *degrees* with a mean value of 7.12 *degrees* [stdev 4.12],
- BMD ranged from 1179.36 to 1351.83 $mgHA/ccm$ with a mean value of 1239.25 $mgHA/ccm$ [stdev 59.50],
- SHG intensity ranging from 5% to 7% with a mean value of 6% [stdev 1],

For set-7 storage conditions were changed to a -80 freezer in order to prevent tissue degradation. Set-7 included 18 osteons. They were stored in water at -80 C before testing. The osteons in set-7 had an aspect ratio of 3.0, H_{set-7} of 569.23 μm [stdev 35.72] and D_{set-7} of 192.44 μm [stdev 6.92]. The following structural parameters were measured:

- BV/TV ranged from 86 to 99% with a mean value of 93% [stdev 4],
- Inclination angle ranged from 3.92 to 11.73 *degrees* with a mean value of 8.02 *degrees* [stdev 1.85],
- BMD ranged from 1164.99 to 1394.95 $mgHA/ccm$ with a mean value of 1228.01 $mgHA/ccm$ [stdev 63.16],

- SHG intensity ranging from 6% to 13% with a mean value of 10% [stdev 2],

Eight osteons in set-6 and four osteons in set-7 were tested with a step-loading profile (detailed in section 3.6.2) and the remaining osteons were tested with a continuous loading profile at a strain rate of 0.0025 s^{-1}. All osteons were tested in HBSS (pH 7.4).

It was possible to measure continuous and loading-unloading mechanical properties. Die to the acidity of DI water, it was decided to change storage protocol to -80 in HBSS for the future sets, to avoid tissue degradation and decalcification.

Compression tests on human SET-8 and SET-9

Osteons in set-8 (n=20) and set-9 (n=18) were obtained from bone of two human donors, males aged 93 and 64. They were cored out within a one day interval and stored in HBSS (pH 7.4) at -80 C. No water came in contact with the sets to ensure the minimum influence of environmental factors on the mechanical properties of the osteons.

The osteons in set-8 had an aspect ratio of 1.6, H_{set-8} of 409.67 μm [stdev 15.80] and D_{set-8} of 256.66 μm [stdev 6.46]. The following structural parameters were measured:

- BV/TV ranged from 80 to 95% with a mean value of 90% [stdev 4],
- Inclination angle ranged from 1.14 to 15.70 *degrees* with a mean value of 8.41 *degrees* [stdev 4.03],
- BMD ranged from 1164.99 to 1251.22 $mgHA/ccm$ with a mean value of 1208.11 $mgHA/ccm$ [stdev 26.24],
- SHG intensity ranging from 5% to 14% with a mean value of 9% [stdev 3],

The osteons in set-9 had an aspect ratio of 1.9, H_{set-9} of 456.43 μm [stdev 29.62] and D_{set-9} of 250.03 μm [stdev 24.01]. The following structural parameters were measured:

- BV/TV ranged from 77 to 96% with a mean value of 88% [stdev 5],
- Inclination angle ranged from 1.00 to 21.15 *degrees* with a mean value of 11.26 *degrees* [stdev 6.47],
- BMD ranged from 1136.24 to 1236.85 $mgHA/ccm$ with a mean value of 1186.55 $mgHA/ccm$ [stdev 29.63],
- SHG intensity ranging from 5% to 15% with a mean value of 8% [stdev 3],

Five osteons in set-8 and four osteons in set-9 were tested with a step-loading profile (detailed in section 3.6.2) and the remaining osteons were tested with a continuous loading profile at a strain rate of 0.0025 s^{-1}. All osteons were tested in HBSS (pH 7.4).

A.3.4 Summary of the experiments on human osteons

For the human bone experiments the issue with the vase-plate was resolved by introducing the sharpening procedure of the drill bits. The storing conditions

were improved for the human set-8 and -9, produced osteons were stored in HBSS at -80 C to prevent collagen degradation and minimise demineralisation.

Geometric and structural parameters of human osteons are summarised in Table A.3. Storage and compression testing conditions are given in Table A.4.

Table A.3: Human osteon description

	H [μm]	D [μm]	aspect ratio	BV/TV [%]	BMD [mg HA/ccm]	SHG [%]
set-4	534.05 [18.66]	240.84 [10.65]	2.3	87 [6]	1276.18 [40.34]	-
set-6	507.83 [10.30]	291.59 [56.31]	1.8	91 [5]	1239.25 [59.50]	6 [1]
set-7	569.23 [35.72]	192.44 [6.92]	3.0	93 [4]	1228.01 [63.16]	10 [2]
set-8	409.67 [15.80]	256.66 [6.46]	1.6	90 [4]	1214.11 [26.24]	9 [3]
set-9	456.43 [29.62]	250.03 [24.01]	1.9	88 [5]	1186.5 [29.63]	8 [3]

Table A.4: Description of storage and compression testing on human osteons

	storage	testing	strain rate
set-4	in water (0 C)	in HBSS	0.0025
set-5	in water (0 C)	in HBSS	-
set-6	in water (0 C)	in HBSS	0.0025
set-7	in water (-80 C)	in HBSS	0.0025
set-8	in HBSS (-80 C)	in HBSS	0.0025
set-9	in HBSS (-80 C)	in HBSS	0.0025

Measured mechanical properties

The following mechanical properties were calculated for the osteons with continuous loading profile in bovine set-2, -3, -4 and in human set-6, -7, -8, and -9: F_{max}, σ_{max}, ε_{yield}, σ_{yield} and E. The values for all of the calculated mechanical properties are presented in Table A.6.

Table A.5: Mechanical properties of bovine osteons

	F_{max} [N]	σ_{max} [MPa]	ε_{yield} [-]	σ_{yield} [MPa]	E [GPa]
set-1	-	-	-	-	-
set-2	-	-	-	57.055 [45.92]	1.630 [0.26]
set-3	7.92 [1.55]	126.49 [11.09]	0.03 [0.01]	109.17 [12.98]	4.10 [1.06]

Table A.6: Mechanical properties of human osteons

	F_{max} [N]	σ_{max} [MPa]	ε_{yield} [-]	σ_{yield} [MPa]	E [GPa]
set-4	6.22 [1.43]	132.21 [25.44]	0.03 [0.01]	123.28 [30.13]	5.43 [2.74]
set-6	7.78 [3.16]	123.87 [19.39]	0.01 [0.00]	115.64 [18.71]	13.92 [8.00]
set-7	2.09 [0.50]	78.82 [17.23]	0.02 [0.01]	73.44 [17.43]	4.14 [1.06]
set-8	5.75 [1.01]	125.04 [16.28]	0.02 [0.00]	113.95 [16.42]	6.53 [1.58]
set-9	4.38 [1.77]	95.37 [31.96]	0.02 [0.00]	85.32 [29.99]	5.14 [1.80]

Appendix B

Results of the statistical analysis

B.1 Regression analysis results

Table B.1: Regression results for set-3

	Coef	R^2	p-value
set3 BVTV vs Load Max	59.66 , -49.04	0.44	0.04 , 0.02
set3 Inclination Angle vs Load Max	0.08 , 7.32	0.06	0.00 , 0.46
set3 BMD vs Load Max	0.01 , -2.58	0.09	0.81 , 0.35
set3 BVTV vs Stress Max	232.98 , -95.93	0.13	0.61 , 0.25
set3 Inclination Angle vs Stress Max	0.49 , 122.79	0.04	0.00 , 0.52
set3 BMD vs Stress Max	0.09 , 15.81	0.19	0.83 , 0.16
set3 BVTV vs Yield Strain	-0.18 , 0.20	0.34	0.02 , 0.04
set3 Inclination Angle vs Yield Strain	0.00 , 0.03	0.12	0.00 , 0.27
set3 BMD vs Yield Strain	0.00 , 0.02	0.01	0.67 , 0.74
set3 BVTV vs Yield Stress	396.37 , -269.23	0.27	0.20 , 0.08
set3 Inclination Angle vs Yield Stress	0.40 , 106.16	0.02	0.00 , 0.66
set3 BMD vs Yield Stress	0.07 , 25.73	0.08	0.78 , 0.38
set3 BVTV vs Elastic Modulus	29.91 , -24.45	0.23	0.17 , 0.11
set3 Inclination Angle vs Elastic Modulus	-0.04 , 4.44	0.04	0.00 , 0.54
set3 BMD vs Elastic Modulus	-0.00 , 5.77	0.00	0.47 , 0.83

Table B.2: Regression results for set-8

	Coef	R^2	p-value
set8 BVTV vs Load Max	11.09 , -4.19	0.20	0.50 , 0.12
set8 Inclination Angle vs Load Max	0.05 , 5.38	0.03	0.00 , 0.54
set8 BMD vs Load Max	-0.01 , 17.45	0.10	0.13 , 0.30
set8 SHG Intensity vs Load Max	0.24 , 3.70	0.51	0.00 , 0.01
set8 BVTV vs Stress Max	94.64 , 39.65	0.06	0.71 , 0.43
set8 Inclination Angle vs Stress Max	-0.17 , 125.96	0.00	0.00 , 0.89
set8 BMD vs Stress Max	-0.21 , 383.53	0.18	0.04 , 0.14
set8 SHG Intensity vs Stress Max	4.04 , 90.22	0.54	0.00 , 0.00
set8 BVTV vs Yield Strain	0.01 , 0.01	0.01	0.54 , 0.73
set8 Inclination Angle vs Yield Strain	0.00 , 0.02	0.00	0.00 , 0.87
set8 BMD vs Yield Strain	-0.00 , 0.05	0.10	0.12 , 0.30
set8 SHG Intensity vs Yield Strain	-0.00 , 0.02	0.01	0.00 , 0.71
set8 BVTV vs Yield Stress	99.53 , 24.58	0.06	0.82 , 0.41
set8 Inclination Angle vs Yield Stress	-0.52 , 118.20	0.02	0.00 , 0.68
set8 BMD vs Yield Stress	-0.19 , 345.54	0.15	0.06 , 0.20
set8 SHG Intensity vs Yield Stress	3.63 , 83.04	0.43	0.00 , 0.01
set8 BVTV vs Elastic Modulus	1.77 , 5.03	0.00	0.64 , 0.88
set8 Inclination Angle vs Elastic Modulus	-0.06 , 7.08	0.02	0.00 , 0.65
set8 BMD vs Elastic Modulus	-0.00 , 7.80	0.00	0.67 , 0.95
set8 SHG Intensity vs Elastic Modulus	0.25 , 4.49	0.21	0.01 , 0.11
set8 BVTV vs Max Strain	-0.03 , 0.06	0.02	0.19 , 0.63
set8 Inclination Angle vs Max Strain	0.00 , 0.04	0.00	0.00 , 0.84
set8 BMD vs Max Strain	-0.00 , 0.05	0.00	0.52 , 0.90
set8 SHG Intensity vs Max Strain	-0.00 , 0.05	0.16	0.00 , 0.18

Table B.3: Regression results for set-9

	Coef	R^2	p-value
set9 BVTV vs Load Max	29.41 , -21.41	0.79	0.00 , 0.00
set9 Inclination Angle vs Load Max	-0.08 , 5.29	0.09	0.00 , 0.30
set9 BMD vs Load Max	-0.00 , 4.44	0.00	0.83 , 1.00
set9 SHG Intensity vs Load Max	0.12 , 3.42	0.03	0.07 , 0.56
set9 BVTV vs Stress Max	520.43 , -360.23	0.74	0.00 , 0.00
set9 Inclination Angle vs Stress Max	-1.26 , 110.24	0.06	0.00 , 0.39
set9 BMD vs Stress Max	-0.03 , 128.80	0.00	0.74 , 0.93
set9 SHG Intensity vs Stress Max	1.97 , 80.34	0.02	0.02 , 0.60
set9 BVTV vs Yield Strain	0.02 , 0.01	0.05	0.75 , 0.44
set9 Inclination Angle vs Yield Strain	0.00 , 0.02	0.03	0.00 , 0.59
set9 BMD vs Yield Strain	0.00 , 0.01	0.00	0.78 , 0.87
set9 SHG Intensity vs Yield Strain	0.00 , 0.01	0.39	0.00 , 0.02
set9 BVTV vs Yield Stress	461.17 , -319.06	0.68	0.00 , 0.00
set9 Inclination Angle vs Yield Stress	-1.55 , 102.81	0.11	0.00 , 0.24
set9 BMD vs Yield Stress	-0.02 , 111.14	0.00	0.75 , 0.94
set9 SHG Intensity vs Yield Stress	1.37 , 74.36	0.01	0.02 , 0.70
set9 BVTV vs Elastic Modulus	24.63 , -16.46	0.53	0.02 , 0.00
set9 Inclination Angle vs Elastic Modulus	-0.13 , 6.60	0.22	0.00 , 0.09
set9 BMD vs Elastic Modulus	-0.00 , 8.15	0.00	0.70 , 0.89
set9 SHG Intensity vs Elastic Modulus	-0.08 , 5.74	0.01	0.01 , 0.72
set9 BVTV vs Max Strain	0.01 , 0.04	0.00	0.71 , 0.92
set9 Inclination Angle vs Max Strain	0.00 , 0.03	0.17	0.01 , 0.14
set9 BMD vs Max Strain	0.00 , -0.07	0.02	0.78 , 0.64
set9 SHG Intensity vs Max Strain	0.00 , 0.01	0.28	0.53 , 0.05

B.2 Normality test

The results of the Shaprio-Wilk test for the E, σ_{max}, σ_{yield}, ε_{yield}, BV/TV, BMD and SHG intensity data of the 93 and 64 year old human donors are given in Table B.4, B.5, B.6, B.7, B.8, B.9 and B.10 respectively.

Since the p-values for the E, σ_{max}, σ_{yield}, BV/TV and BMD data are higher than the 0.05 significance level, and the W-values are higher than 0.85 for both the 93 and 64 year old data sets, the null hypothesis is confirmed and the data sets can be considered normally distributed.

The p-values for the ε_{yield} data for both donors and SHG intensity data for the 64 year old donor are lower than the 0.05 significance level, and the W-values are lower than 0.85, the null hypothesis is rejected and the data sets can not be considered normally distributed.

Table B.4: The Shapiro-Wilk normality test for E data

Elastic Modulus Data	size n	W statistic	P value
93 yo donor	13	0.940	0.463
64 yo donor	14	0.882	0.063

Table B.5: The Shapiro-Wilk normality test for σ_{max}

σ_{max} Data	size n	W statistic	P value
93 yo donor	13	0.923	0.278
64 yo donor	14	0.977	0.952

Table B.6: The Shapiro-Wilk normality test for σ_{yield}

σ_{yield} Data	size n	W statistic	P value
93 yo donor	13	0.957	0.709
64 yo donor	14	0.962	0.762

Table B.7: The Shapiro-Wilk normality test for ε_{yield}

ε_{yield} Data	size n	W statistic	P value
93 yo donor	13	0.852	0.030
64 yo donor	14	0.780	0.003

Table B.8: The Shapiro-Wilk normality test for BV/TV data

BV/TV Data	size n	W statistic	P value
93 yo donor	13	0.914	0.209
64 yo donor	14	0.963	0.770

Table B.9: The Shapiro-Wilk normality test for BMD data

BMD Data	size n	W statistic	P value
93 yo donor	13	0.955	0.674
64 yo donor	14	0.964	0.787

Table B.10: The Shapiro-Wilk normality test for SHG intensity data

SHG Data	size n	W statistic	P value
93 yo donor	13	0.926	0.300
64 yo donor	14	0.824	0.010

B.3 Grubb's test for outliers

The results of the Grubb's test for the E, σ_{max}, σ_{yield}, ε_{yield}, BV/TV, BMD and SHG intensity data of the 93 and 64 year old human donors are given in Tables B.11, B.12, B.13, B.14, B.15, B.16 and **??**.

The null hypothesis of no outliers was rejected for the E, ε_{yield}, SHG intensity data of the 64 year old human donor, indicating that the datasets contained an outlier. This outlier was identified using an IQR method and found to be osteon #10 for E with an elastic modulus of 10.286 GPa and osteon #5 for ε_{yield} and SHG intensity with a $\varepsilon_{yield} = 0.03$ and $I = 15.296\%$ (Figure B.1).

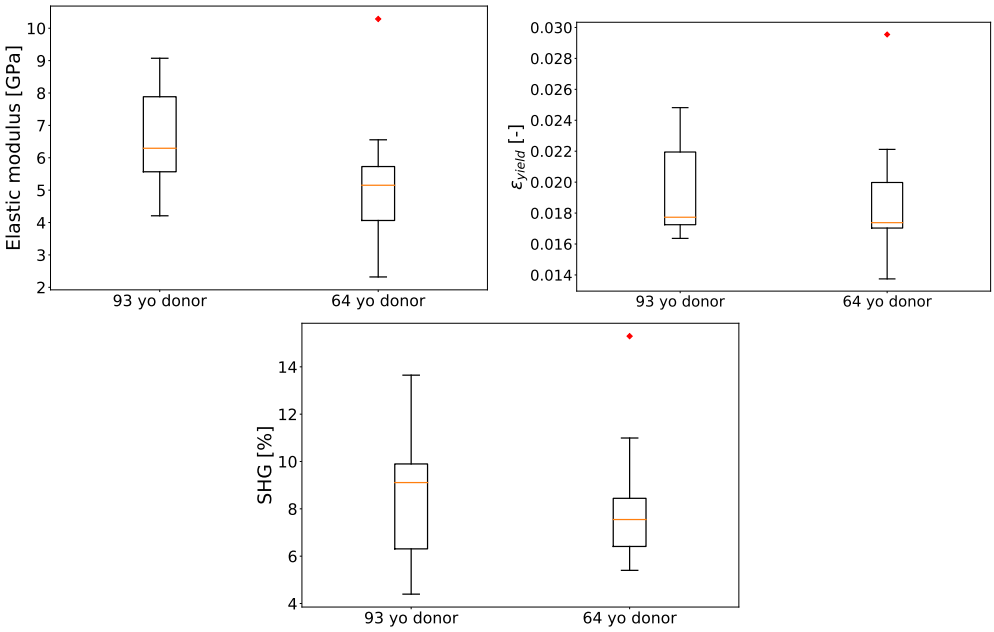

Figure B.1: Box plots for the E, ε_{yield}, SHG intensity data of the first and second donor

Table B.11: The Grubb's test for outliers for E

Data	N	Min	Mean	Max	Stdev	G	Critical G	Conclusion
93 yo donor	13	4.209	6.614	9.073	1.542	1.594	2.331	There are no outliers in the data set
64 yo donor	14	2.320	5.144	10.286	1.804	2.851	2.372	There is at least one outlier in the data set

Table B.12: The Grubb's test for outliers for σ_{max}

Data	N	Min	Mean	Max	Stdev	G	Critical G	Conclusion
93 yo donor	13	99.193	124.577	149.121	15.724	1.561	2.331	There are no outliers in the data set
64 yo donor	14	41.832	95.366	160.207	31.962	2.029	2.372	There are no outliers in the data set

Table B.13: The Grubb's test for outliers for σ_{yield}

Data	N	Min	Mean	Max	Stdev	G	Critical G	Conclusion
93 yo donor	13	86.434	113.891	138.303	15.777	1.547	2.331	There are no outliers in the data set
64 yo donor	14	34.627	85.319	152.231	29.992	2.231	2.372	There are no outliers in the data set

Table B.14: The Grubb's test for outliers for ε_{yield}

Data	N	Min	Mean	Max	Stdev	G	Critical G	Conclusion
93 yo donor	13	0.016	0.020	0.025	0.003	1.706	2.331	There are no outliers in the data set
64 yo donor	13	0.014	0.018	0.022	0.002	2.021	2.331	There are no outliers in the data set

Table B.15: The Grubb's test for outliers for BV/TV

Data	N	Min	Mean	Max	Stdev	G	Critical G	Conclusion
93 yo donor	13	0.796	0.897	0.950	0.039	1.333	2.331	There are no outliers in the data set
64 yo donor	14	0.766	0.877	0.955	0.054	1.460	2.372	There are no outliers in the data set

Table B.16: The Grubb's test for outliers for BMD

Data	N	Min	Mean	Max	Stdev	G	Critical G	Conclusion
93 yo donor	13	1164.988	1213.633	1279.967	31.658	2.095	2.331	There are no outliers in the data set
64 yo donor	14	1136.244	1186.547	1236.850	29.629	1.698	2.372	There are no outliers in the data set

Table B.17: The Grubb's test for outliers for SHG intensity

Data	N	Min	Mean	Max	Stdev	G	Critical G	Conclusion
93 yo donor	13	4.395	8.505	13.648	2.854	1.802	2.331	There are no outliers in the data set
64 yo donor	14	5.401	7.999	15.296	2.501	2.918	2.372	There is at least one outlier in the data set

After removing the outlier from the E, ε_{yield}, SHG intensity data sets, the Shapiro-Wilk test for normality was repeated for these data sets. The results are summarised in Tables B.18, B.19, B.20.

Since the p-values for E and SHG intensity data from the updated Shapiro-Wilk test are higher than the 0.05 significance level, and the W-values were higher than 0.85 for both the 93 and 64 year old data sets, the null hypothesis is confirmed and the data can be assumed to be normally distributed. However the p-value for ε_{yield} of the 93 year old donor is lower than 0.05 significance level, the null hypothesis is rejected and the data can not be assumed to be normally distributed.

Probability plot of the E, ε_{yield}, SHG intensity data spread can be seen in figure **??**.

Table B.18: The updated Shapiro-Wilk normality test for the E data set with the outlier removed

Elastic Modulus Data	size n	W statistic	P value
93 yo donor	13	0.940	0.463
64 yo donor	13	0.962	0.786

Table B.19: The updated Shapiro-Wilk normality test for the ε_{yield} data set with the outlier removed

ε_{yield} Data	size n	W statistic	P value
93 yo donor	13	0.852	0.030
64 yo donor	13	0.888	0.092

Table B.20: The updated Shapiro-Wilk normality test for the SHG intensity data set with the outlier removed

SHG Data	size n	W statistic	P value
93 yo donor	13	0.926	0.300
64 yo donor	13	0.949	0.578

B.4 Test for homoscedasticity

The results of the test for homoscedasticity for the E, σ_{max}, σ_{yield}, BV/TV, BMD and SHG intensity data of the 93 and 64 year old human donors are given in Tables B.21, B.22, B.23, B.24, B.25 and B.26.

Table B.21: The Bartlett's test for homoscedasticity for E

Variation of the first set	Variation of the second set	Bartlett's statistic	p value	Conclusion
2.379	1.314	0.999	0.317	sets are homoscedastic

Table B.22: The Bartlett's test for homoscedasticity for σ_{max}

Variation of the first set	Variation of the second set	Bartlett's statistic	p value	Conclusion
247.252	1021.577	5.455	0.020	sets are heteroscedastic

Table B.23: The Bartlett's test for homoscedasticity for σ_{yield}

Variation of the first set	Variation of the second set	Bartlett's statistic	p value	Conclusion
248.907	899.525	4.533	0.033	sets are heteroscedastic

Table B.24: The Bartlett's test for homoscedasticity for BV/TV

Variation of the first set	Variation of the second set	Bartlett's statistic	p value	Conclusion
0.001	0.003	4.470	0.034	sets are heteroscedastic

Table B.25: The Bartlett's test for homoscedasticity for BMD

Variation of the first set	Variation of the second set	Bartlett's statistic	p value	Conclusion
1002.260	877.897	0.058	0.810	sets are homoscedastic

Table B.26: The Bartlett's test for homoscedasticity for SHG intensity

Variation of the first set	Variation of the second set	Bartlett's statistic	p value	Conclusion
8.144	2.322	4.264	0.039	sets are heteroscedastic

B.5 One-Factor ANOVA test and Kruskal Wallis H tests

Normally distributed, homoscedatic E and BMD data sets were subjected to an ANOVA test. Not normally distributed ε_{yield} data set and heteroscedatic σ_{max}, σ_{yield}, BV/TV and SHG intensity data sets were subjected to a Kruskal Wallis H Test. The null hypothesis of the ANOVA and Kruskal Wallis H tests is that two groups have the same population mean. The results of these two tests for the E, σ_{max}, σ_{yield}, ε_{yield}, BV/TV, BMD and SHG intensity data from the 93 and 64 year old human donors are given in Table B.27. The box plots for the data subjected to ANOVA and Kruskal Wallis H tests is presented in Figures **??** and **??**.

Table B.27: The one-Factor ANOVA test for E

Mean E [GPa] of the 93year old donor	Mean E [GPa] of the 64 year old donor	F-statistic	p value	Conclusion
6.614	4.748	11.311	0.003	group means are not equal

Table B.28: The Kruskal-Wallis H-test for σ_{max}

Mean σ_{max} [MPa] of the 93year old donor	Mean σ_{max} [MPa] of the 64 year old donor	F-statistic	p value	Conclusion
124.577	95.366	6.615	0.010	group means are not equal

Table B.29: The Kruskal-Wallis H-test for ε_{yield}

Mean ε_{yield} [-] of the 93 year old donor	Mean ε_{yield} [-] of the 64 year old donor	F-statistic	p value	Conclusion
0.020	0.018	2.136	0.144	group means are not significantly different

Table B.30: The Kruskal-Wallis H-test for σ_{yield}

Mean σ_{yield} [MPa] of the 93 year old donor	Mean σ_{yield} [MPa] of the 64 year old donor	F-statistic	p value	Conclusion
113.891	85.319	7.651	0.006	group means are not equal

Table B.31: The Kruskal-Wallis H-test for BV/TV

Mean BV/TV [-] of the 92year old donor	Mean BV/TV [-] of the 76 year old donor	F-statistic	p value	Conclusion
0.906	0.877	1.524	0.217	group means are not significantly different

Table B.32: The one-Factor ANOVA test for BMD

Mean BMD [mg HA/ccm] of the 93year old donor	Mean BMD [mg HA/ccm] of the 64 year old donor	F-statistic	p value	Conclusion
1213.633	1186.547	4.883	0.037	group means are not equal

Table B.33: The Kruskal-Wallis H-test for SHG intensity

Mean SHG [%] of the 93year old donor	Mean SHG [%] of the 64 year old donor	F-statistic	p value	Conclusion
8.505	7.438	1.105	0.293	group means are not significantly different

Appendix C

Mechanical property values

Table C.1: Mechanical properties of osteons in set3

Sample	Max Load [N]	Max Stress [MPa]	Yield Strain [-]	Yield Stress [MPa]	Elastic Modulus [Gpa]
1	9.234	131.910	0.024	131.185	5.841
2	8.862	124.812	0.025	110.418	4.698
3	9.544	130.738	0.034	109.204	3.415
4	8.771	128.986	0.021	119.339	6.144
5	9.120	132.177	0.028	112.924	4.291
6	7.844	115.352	0.030	96.945	3.434
8	4.100	110.811	0.042	85.443	2.130
9	7.170	137.881	0.027	114.007	4.568
10	7.139	127.478	0.030	106.152	3.780
11	6.476	113.619	0.033	99.954	3.256
12	7.173	113.860	0.027	95.347	3.753
13	9.613	150.208	0.035	129.085	3.917

Table C.2: Mechanical properties of osteons in set4

Sample	Max Load [N]	Max Stress [MPa]	Yield Strain [-]	Yield Stress [MPa]	Elastic Modulus [Gpa]
1	5.531	120.237	0.049	119.322	2.557
2	8.389	167.771	0.018	158.358	9.647
3	6.812	148.095	0.017	143.617	9.365
5	5.694	116.205	0.019	85.411	5.115
6	4.519	129.117	0.046	130.994	3.005
7	7.148	148.912	0.021	142.506	7.406
8	6.123	139.158	0.024	126.096	5.805
9	7.763	152.209	0.021	143.357	7.553
10	6.952	154.483	0.023	148.525	6.989
11	8.234	161.447	0.037	158.234	4.575
12	5.642	137.608	0.033	114.655	3.703
13	2.528	58.781	0.034	45.737	1.420
14	7.668	159.750	0.016	155.724	11.512
15	5.948	116.626	0.015	73.771	5.771
16	4.963	107.901	0.038	92.936	2.615
17	5.582	111.639	0.048	101.502	2.185
18	6.273	125.457	0.048	124.610	2.702
19	7.703	148.142	0.024	139.965	6.413
20	4.775	108.522	0.031	136.961	4.773

Table C.3: Mechanical properties of osteons in set5

Sample	Max Load [N]	Max Stress [MPa]	Yield Strain [-]	Yield Stress [MPa]	Elastic Modulus [Gpa]
5	4.438	131.402	0.007	131.357	26.854
6	8.125	255.412	0.015	297.789	22.111

Table C.4: Mechanical properties of osteons in set6

Sample	Max Load [N]	Max Stress [MPa]	Yield Strain [-]	Yield Stress [MPa]	Elastic Modulus [Gpa]
10	10.663	142.042	0.014	127.274	8.728
11	12.386	109.813	0.011	109.813	11.858
12	4.497	113.883	0.021	107.300	5.640
13	3.642	93.410	0.005	80.099	27.634
14	8.792	136.184	0.017	125.462	8.620
15	6.685	148.039	0.008	119.926	18.886

Table C.5: Mechanical properties of osteons in set7

Sample	Max Load [N]	Max Stress [MPa]	Yield Strain [-]	Yield Stress [MPa]	Elastic Modulus [Gpa]
1	1.954	73.005	0.014	71.366	3.819
2	1.707	64.444	0.010	52.523	2.896
3	1.564	64.182	0.011	62.118	5.269
4	3.215	117.444	0.028	115.031	4.386
5	2.092	74.707	0.031	69.359	2.429
6	2.972	110.291	0.024	104.054	4.778
7	2.155	84.258	0.015	82.943	6.264
9	1.736	67.103	0.017	64.847	4.212
10	1.798	68.380	0.017	60.913	3.525
11	2.371	89.340	0.029	70.117	2.634
12	2.080	81.797	0.019	77.637	4.631
13	2.118	72.691	0.016	68.352	5.043
14	1.445	57.070	0.016	55.522	3.975

Table C.6: Mechanical properties of osteons in set8

Sample	Max Load [N]	Max Stress [MPa]	Yield Strain [-]	Yield Stress [MPa]	Elastic Modulus [Gpa]
2	6.865	149.121	0.017	138.303	9.073
4	5.733	135.055	0.016	115.327	8.023
5	7.191	139.89	0.022	125.322	6.294
6	6.293	127.677	0.017	109.959	7.275
8	6.255	138.773	0.017	137.915	8.912
9	3.895	99.193	0.022	91.366	4.611
11	5.91	130.793	0.023	118.776	5.678
12	5.665	126.563	0.025	120.919	5.301
15	4.303	101.06	0.024	94.467	4.209
16	6.87	136.664	0.018	124.362	7.885
17	4.58	101.521	0.018	86.434	5.568
18	5.413	114.211	0.021	104.27	5.584
19	5.949	118.98	0.017	113.161	7.566

Table C.7: Mechanical properties of osteons in set9

Sample	Max Load [N]	Max Stress [MPa]	Yield Strain [-]	Yield Stress [MPa]	Elastic Modulus [Gpa]
2	4.284	85.503	0.018	71.002	4.394
3	4.35	96.116	0.017	82.102	5.46
4	2.991	64.368	0.018	61.23	3.953
5	5.045	107.392	0.03	93.596	3.402
6	3.455	72.047	0.017	67.287	4.55
7	5.636	107.951	0.021	89.942	4.843
8	3.492	84.489	0.017	83.133	5.472
9	5.4	105.357	0.017	88.821	5.861
10	8.038	160.207	0.017	152.231	10.286
11	6.478	133.866	0.022	116.938	5.798
12	1.383	41.832	0.017	34.627	2.32
14	5.523	131	0.021	123.242	6.555
15	3.763	98.093	0.018	88.27	5.522
16	1.435	46.902	0.014	42.05	3.592

Appendix D

Stress-strain curves

Continuous loading

SET3

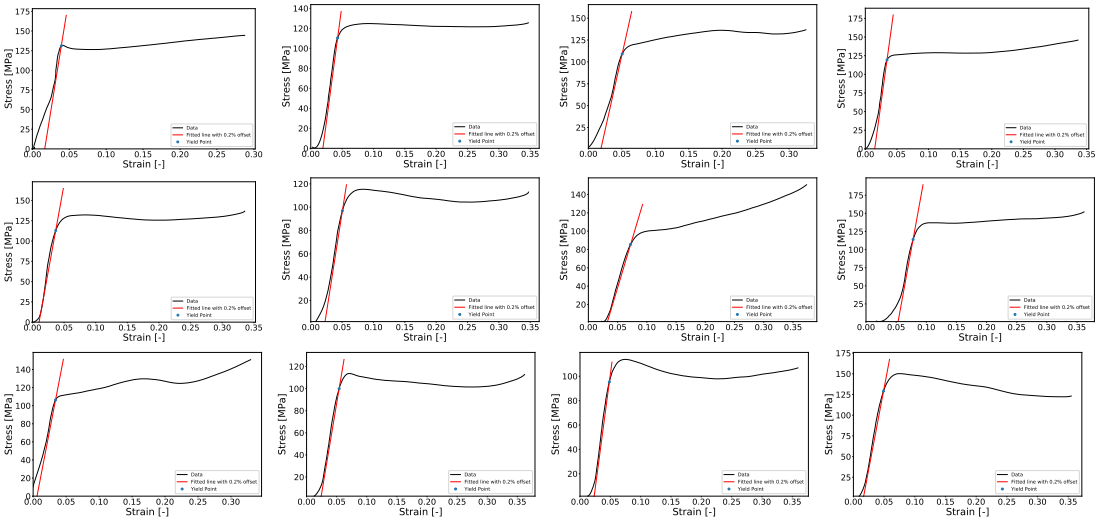

SET4

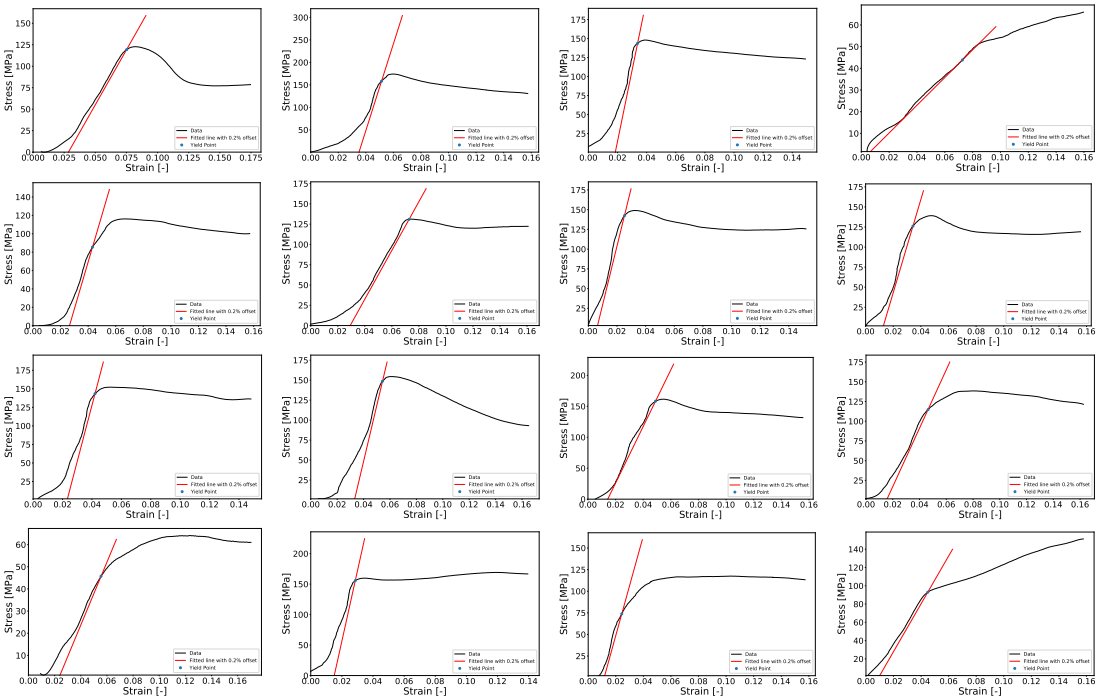

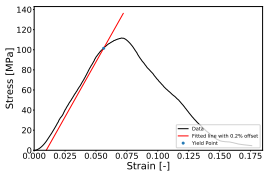

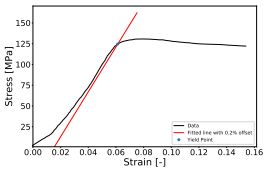

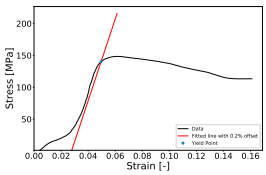

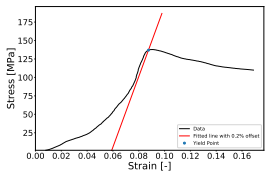

SET5

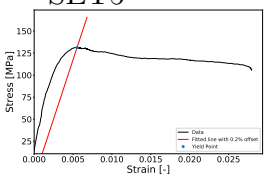

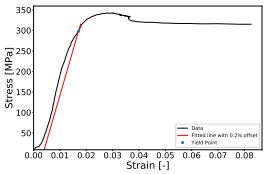

SET6

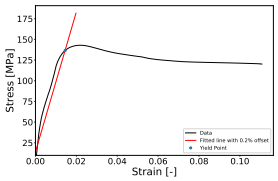

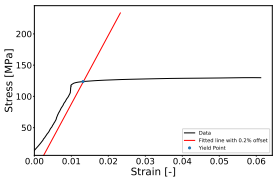

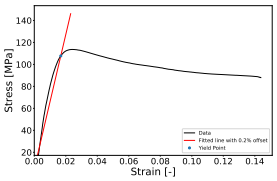

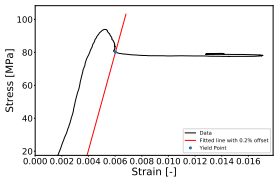

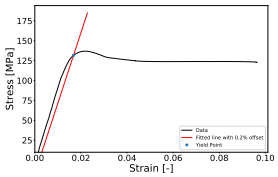

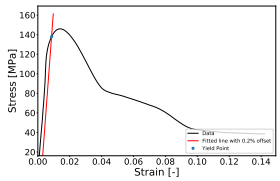

SET7

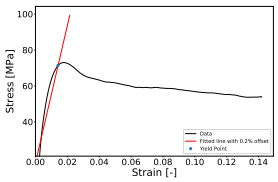

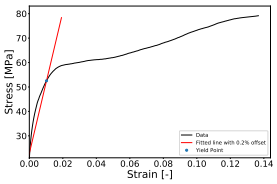

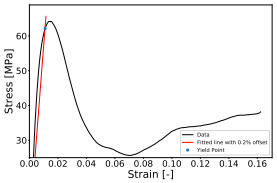

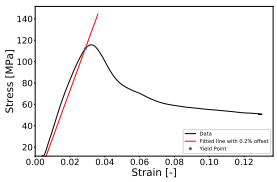

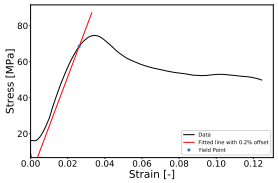

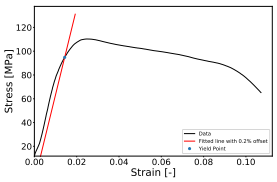

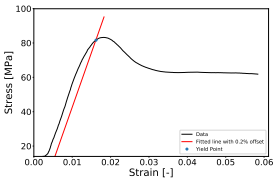

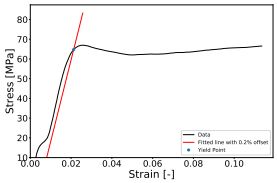

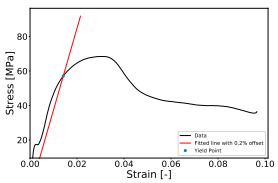

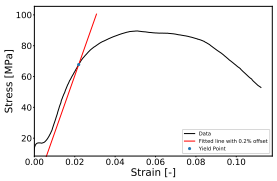

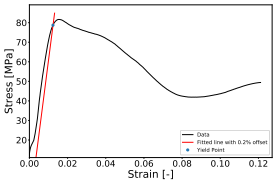

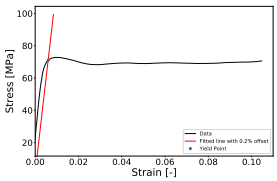

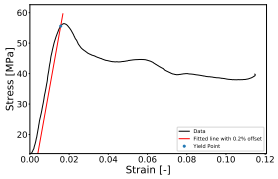

SET8

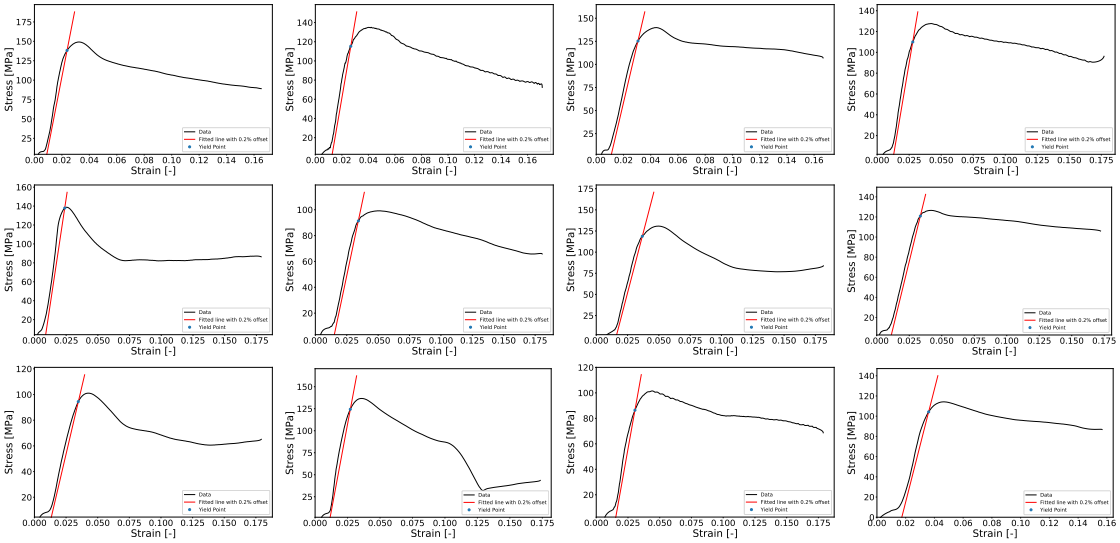
Stress [MPa]
Strain [-]
Data
Fitted line with 0.2% offset
Yield Point

SET9

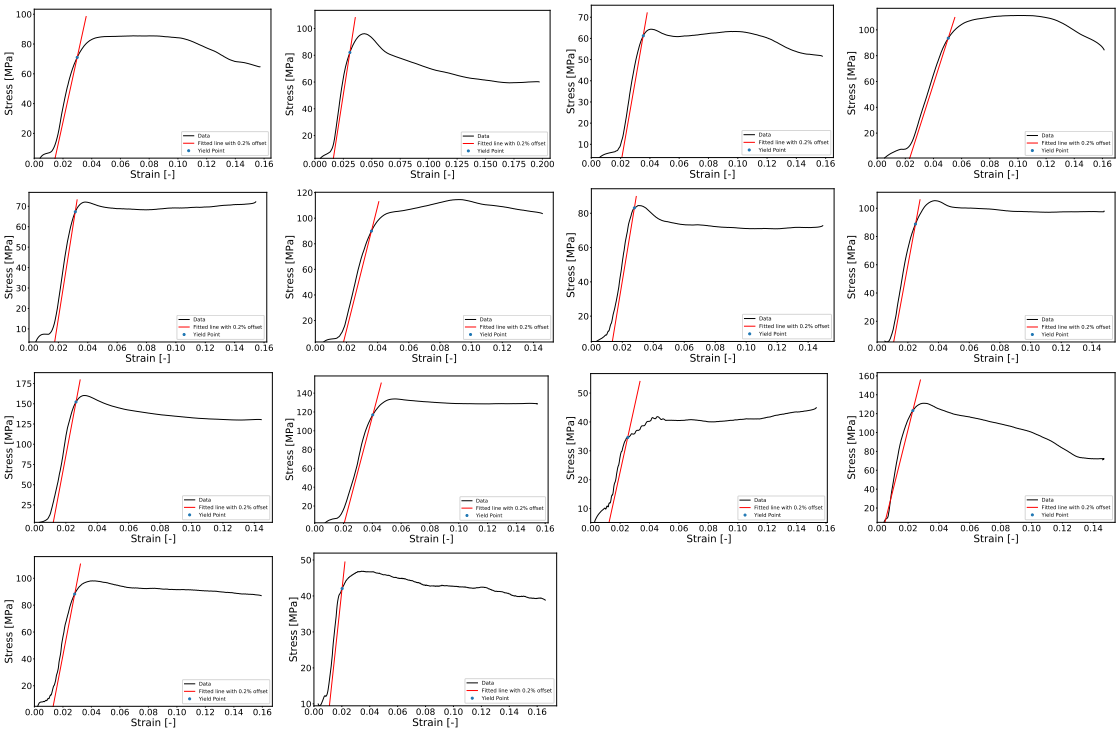
Stress [MPa]
Strain [-]
Data
Fitted line with 0.2% offset
Yield Point

Step loading

SET5

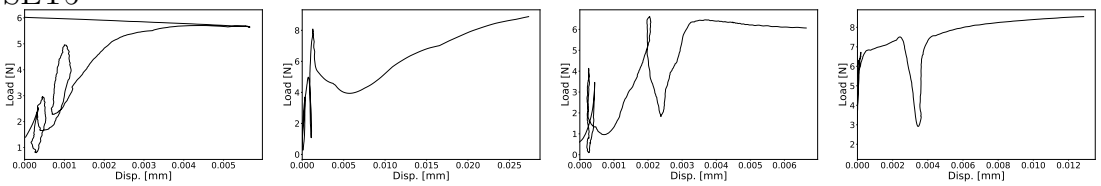

SET6

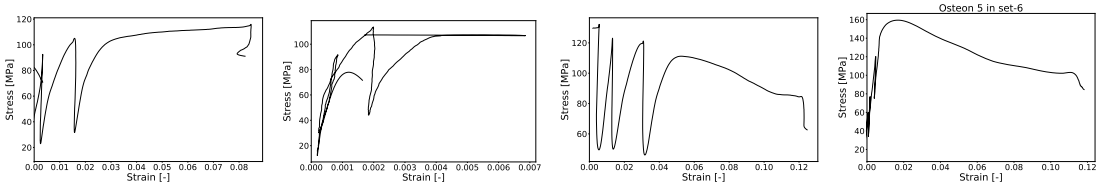

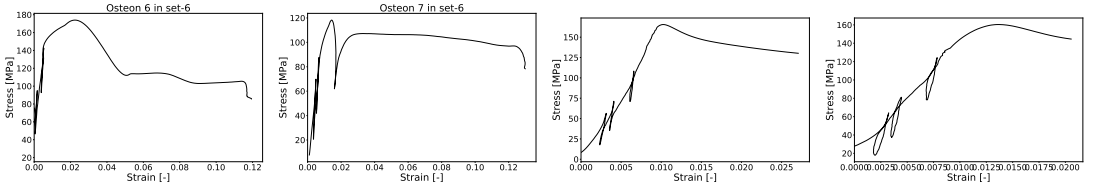

SET7

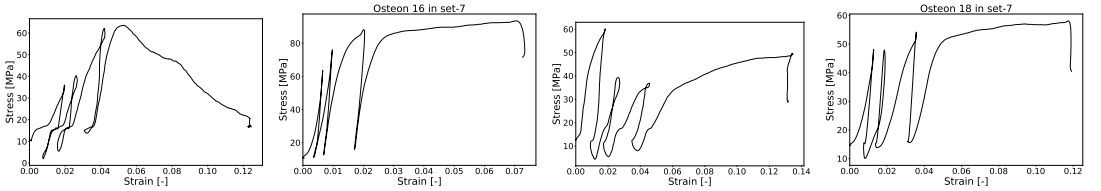

SET8

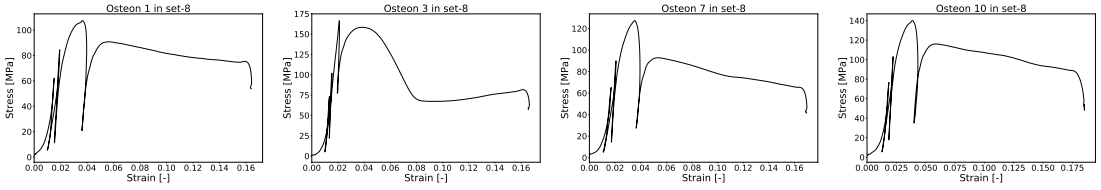

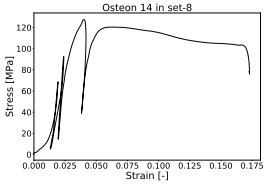

SET9

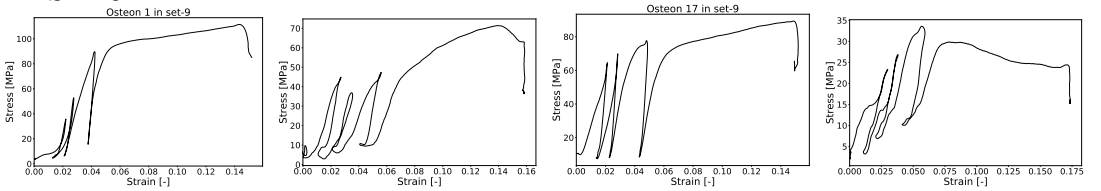

Appendix E

Sequential images of damage accumulation

Set8O02

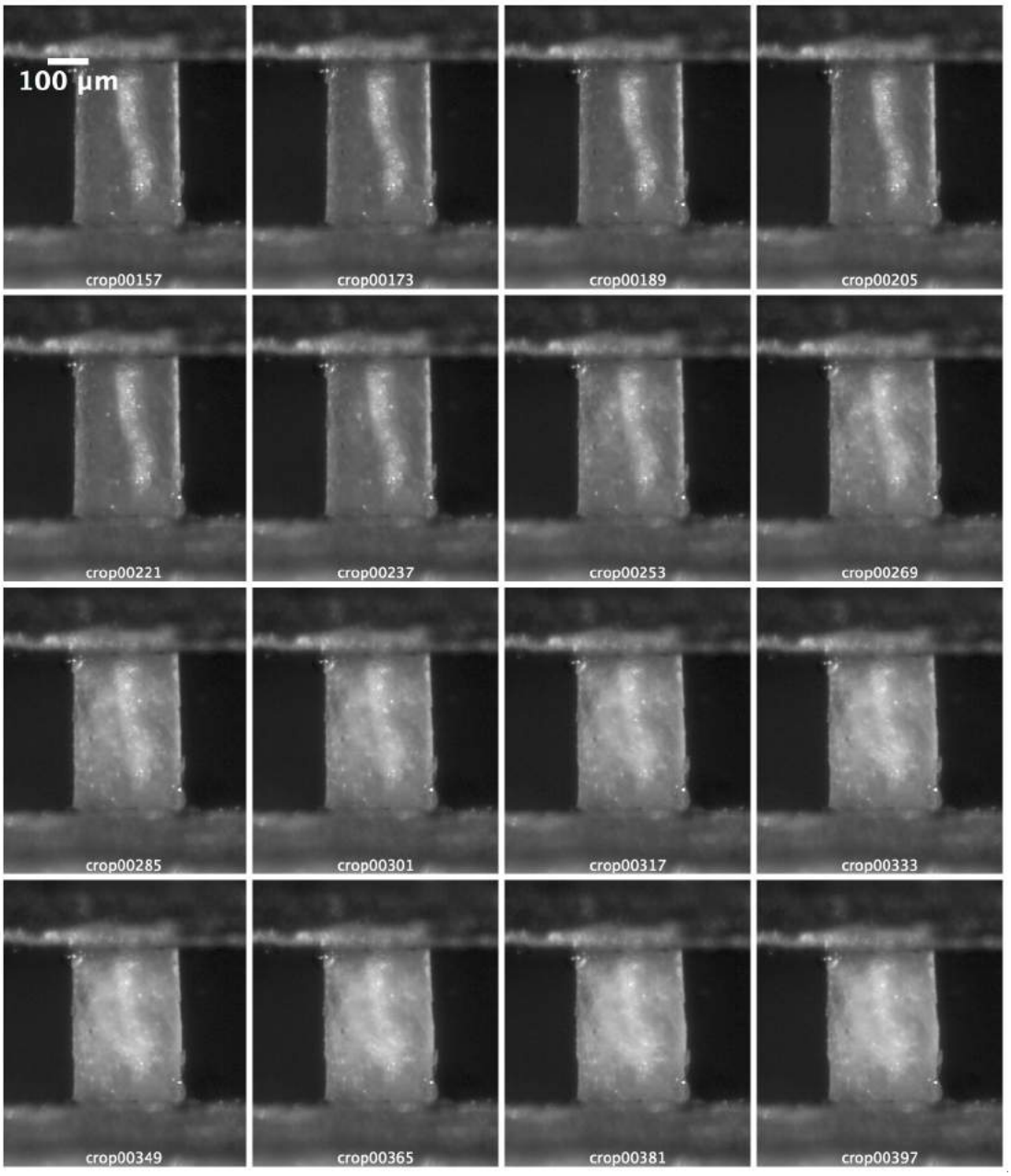

Set8O04

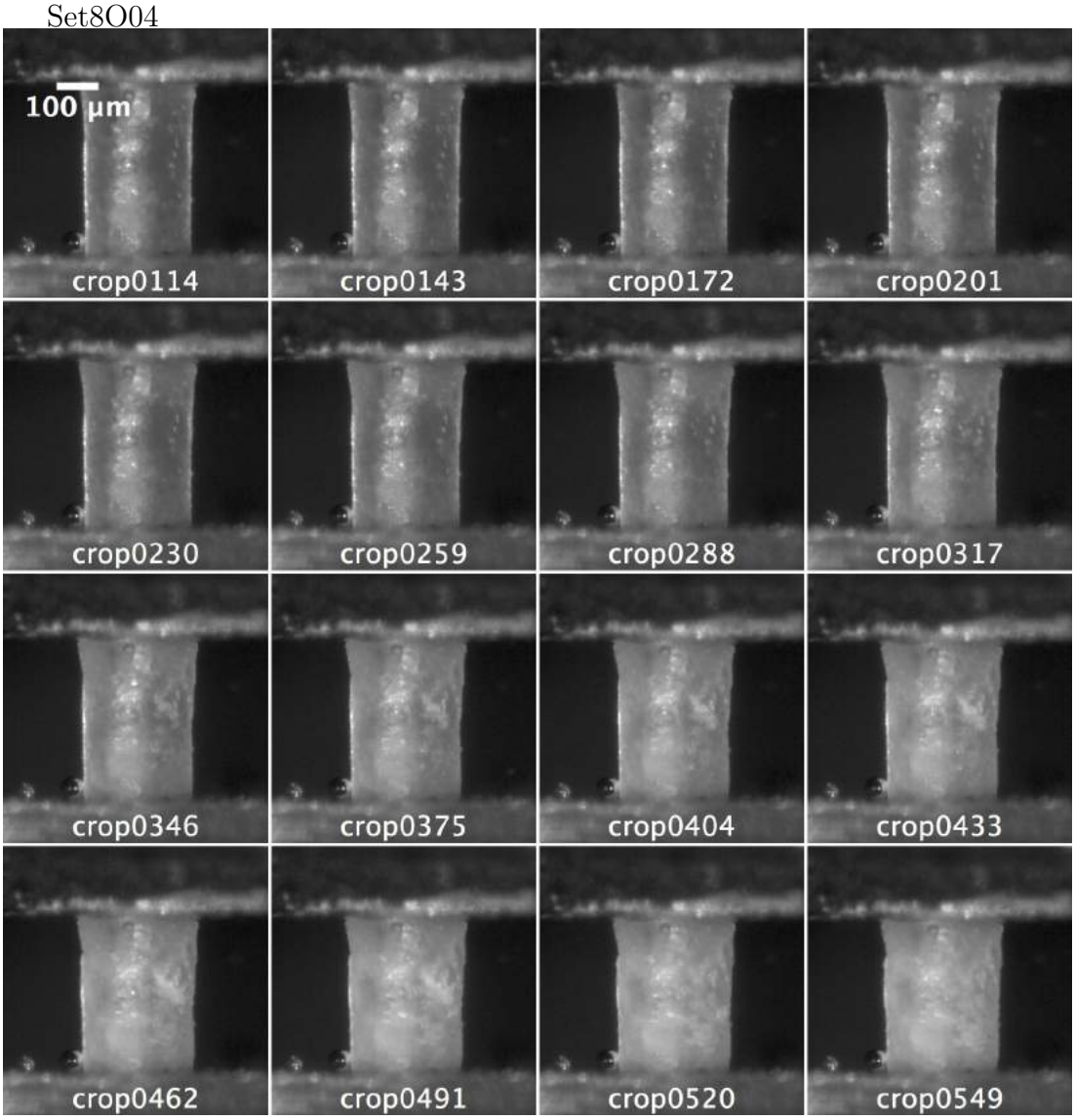
100 µm
crop0114
crop0143
crop0172
crop0201
crop0230
crop0259
crop0288
crop0317
crop0346
crop0375
crop0404
crop0433
crop0462
crop0491
crop0520
crop0549

Set8O05

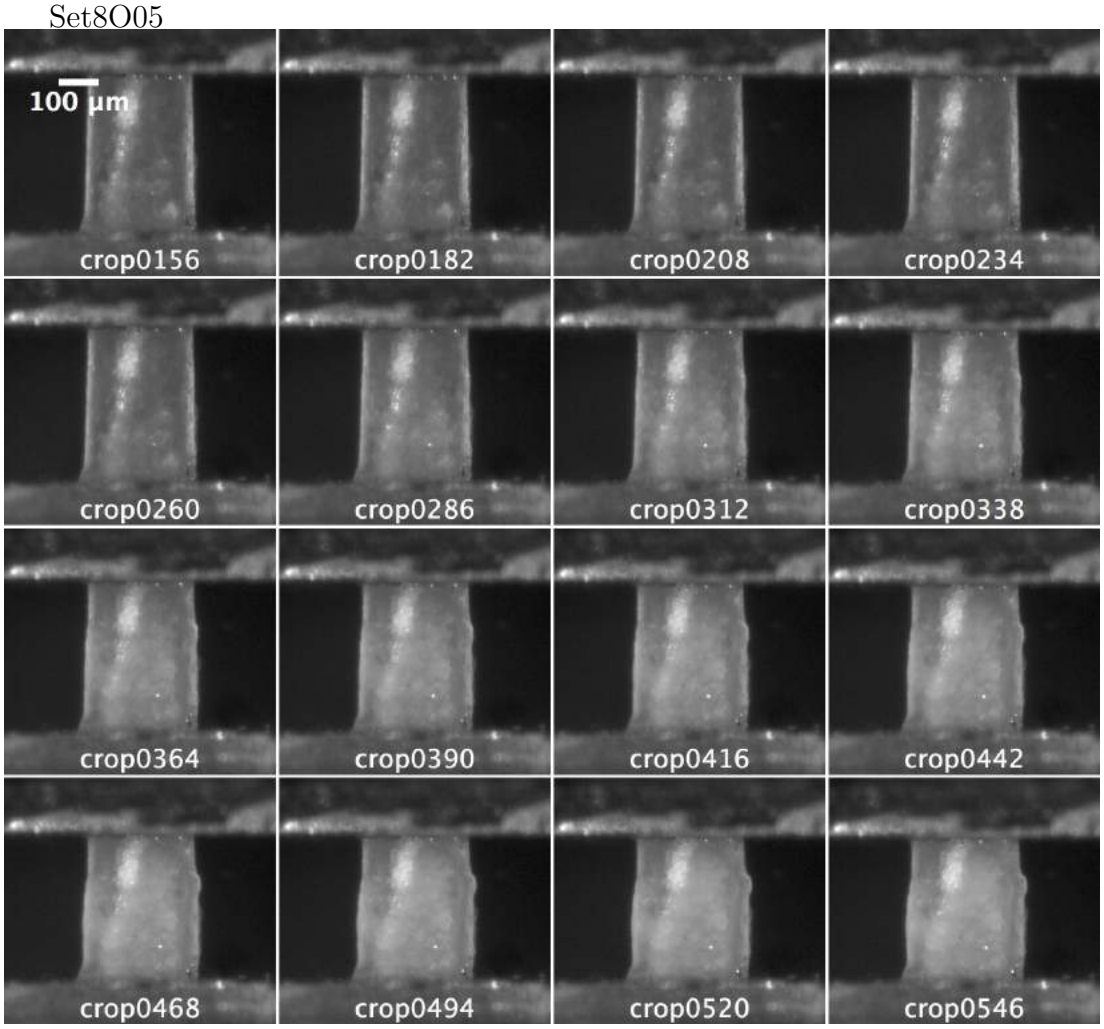
100 µm
crop0156
crop0182
crop0208
crop0234
crop0260
crop0286
crop0312
crop0338
crop0364
crop0390
crop0416
crop0442
crop0468
crop0494
crop0520
crop0546

Set8O06

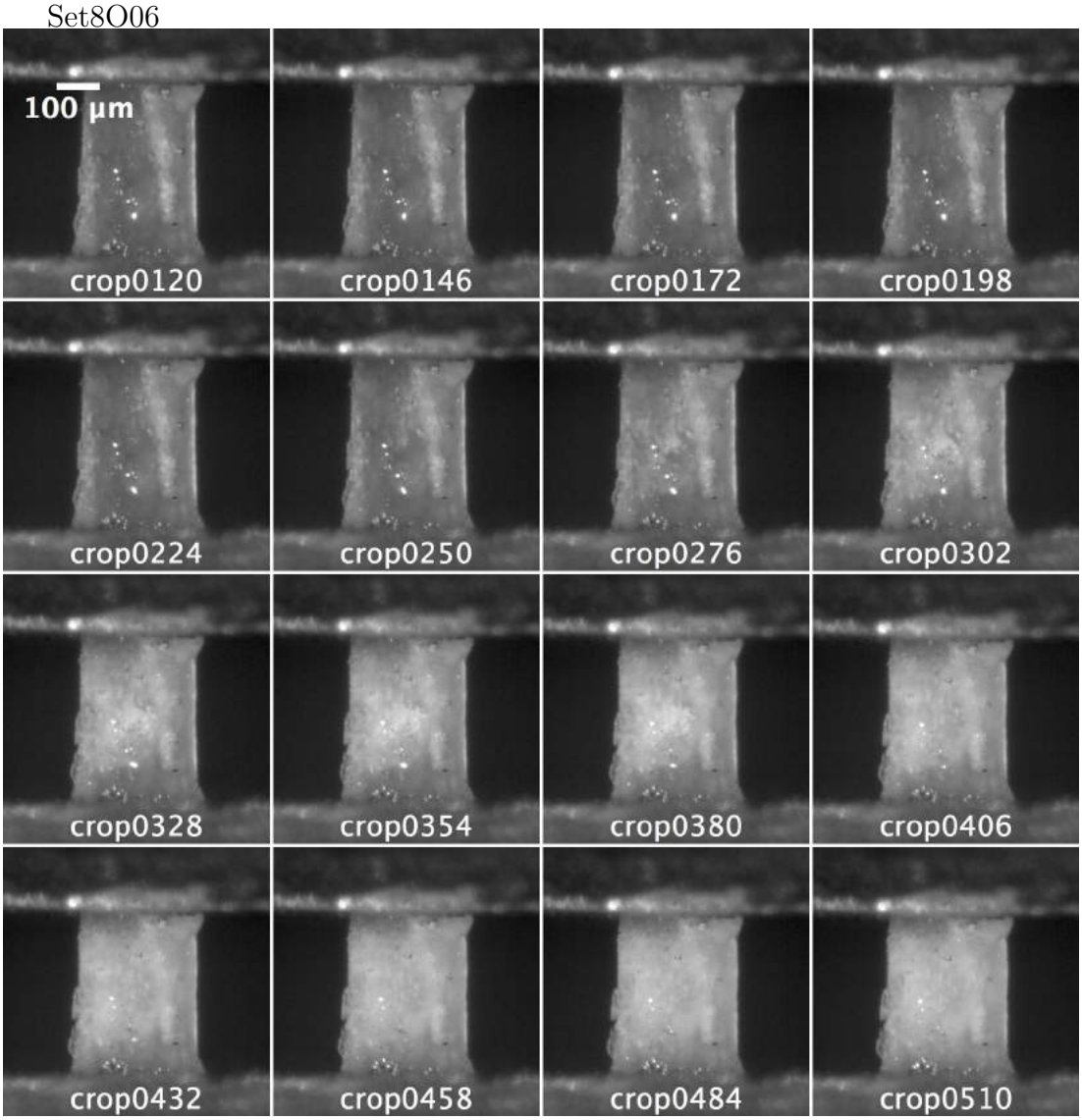
100 µm
crop0120
crop0146
crop0172
crop0198
crop0224
crop0250
crop0276
crop0302
crop0328
crop0354
crop0380
crop0406
crop0432
crop0458
crop0484
crop0510

Set8O08

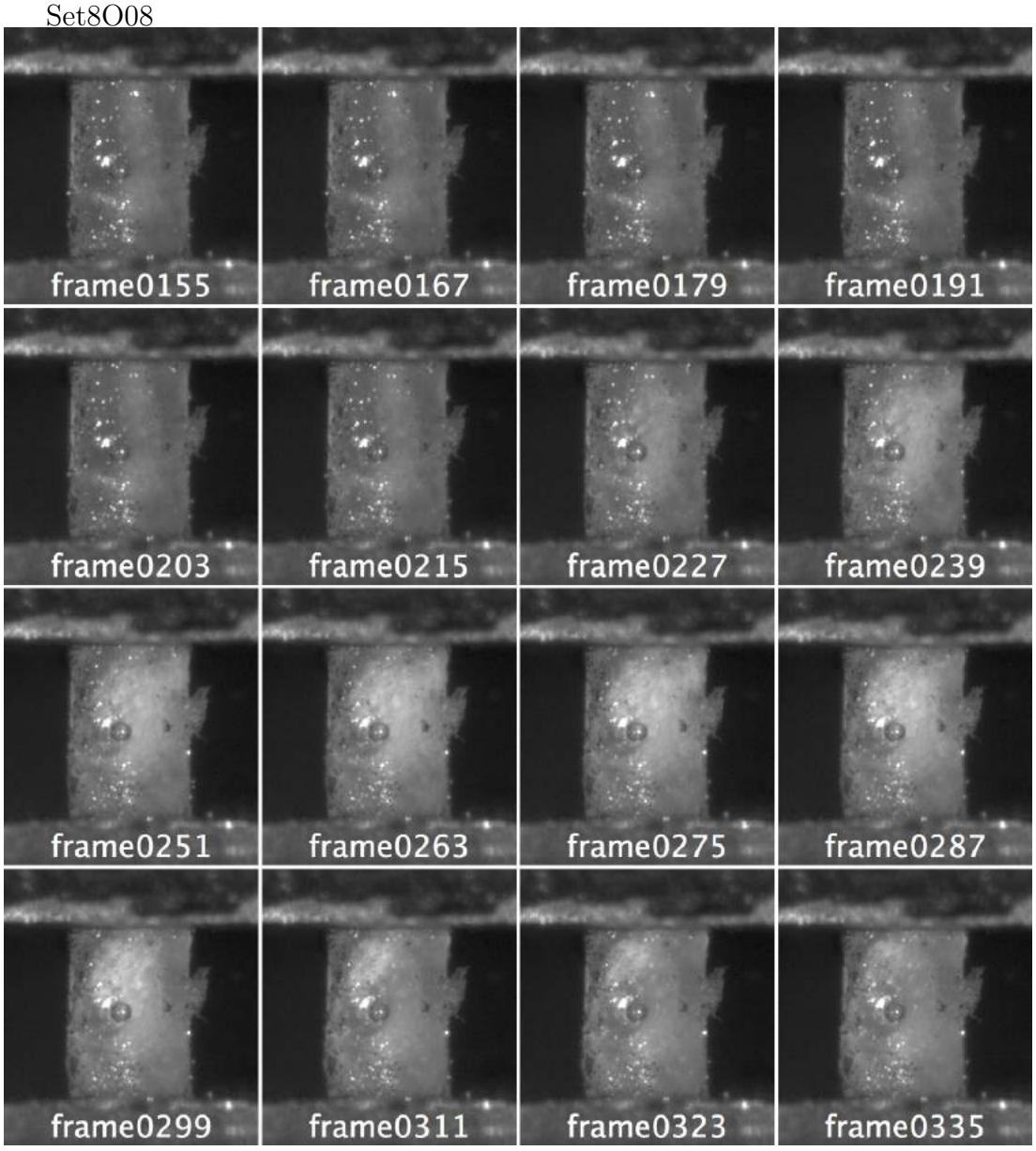
frame0155
frame0167
frame0179
frame0191
frame0203
frame0215
frame0227
frame0239
frame0251
frame0263
frame0275
frame0287
frame0299
frame0311
frame0323
frame0335

Set8O09

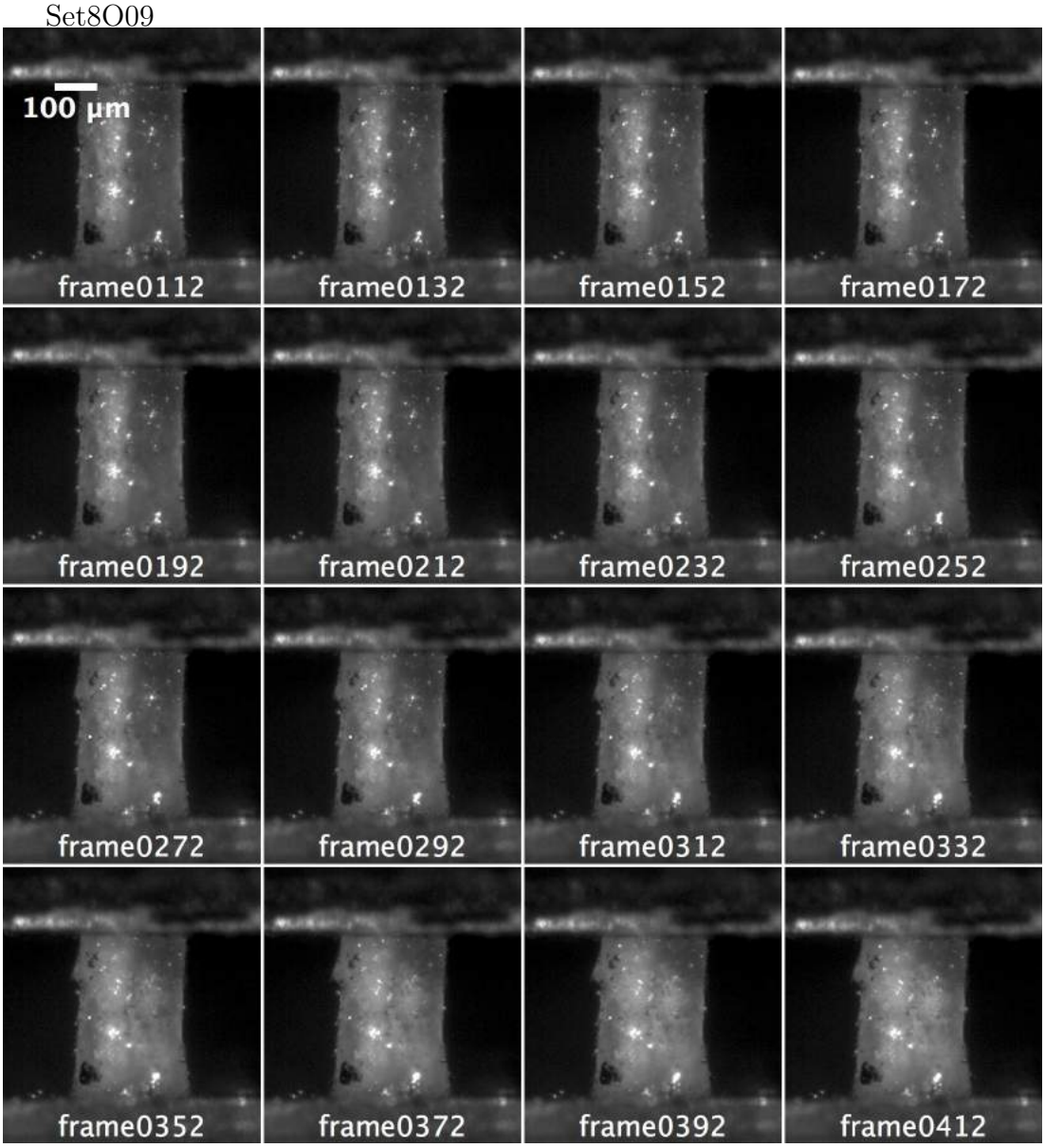
100 µm
frame0112
frame0132
frame0152
frame0172
frame0192
frame0212
frame0232
frame0252
frame0272
frame0292
frame0312
frame0332
frame0352
frame0372
frame0392
frame0412

Set8O11

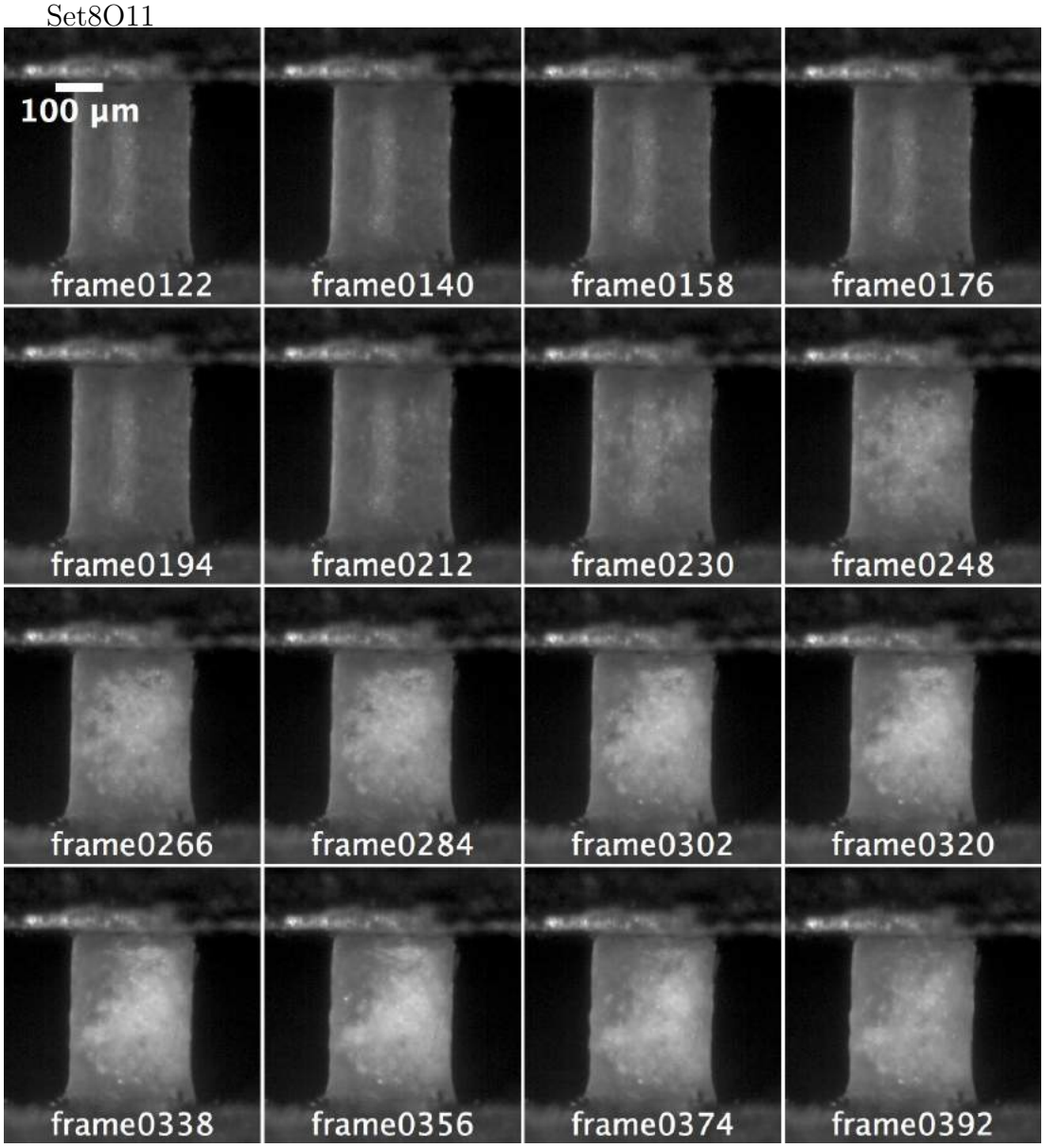
100 µm
frame0122
frame0140
frame0158
frame0176
frame0194
frame0212
frame0230
frame0248
frame0266
frame0284
frame0302
frame0320
frame0338
frame0356
frame0374
frame0392

Set8O12

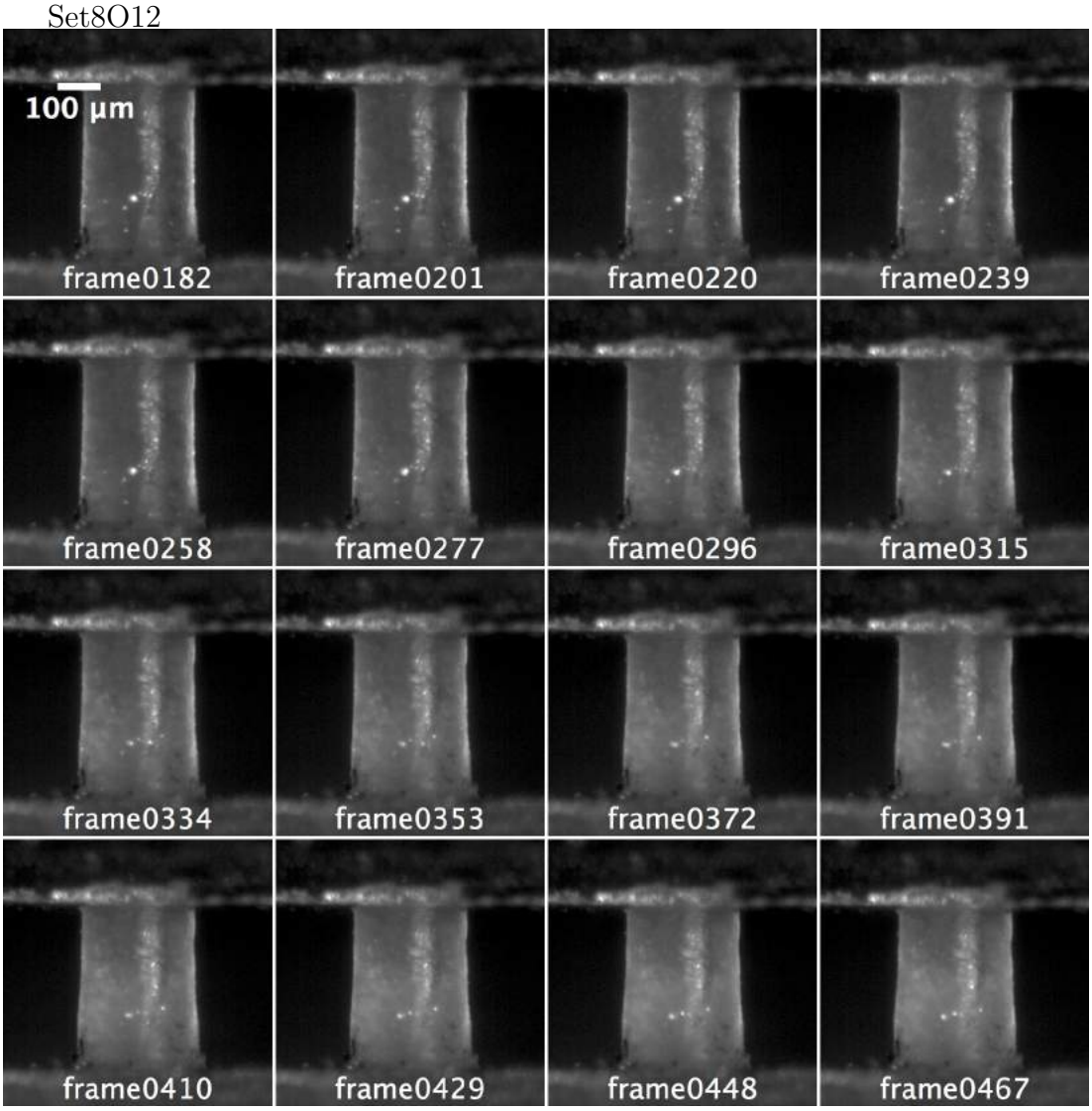
100 µm
frame0182
frame0201
frame0220
frame0239
frame0258
frame0277
frame0296
frame0315
frame0334
frame0353
frame0372
frame0391
frame0410
frame0429
frame0448
frame0467

Set8O15

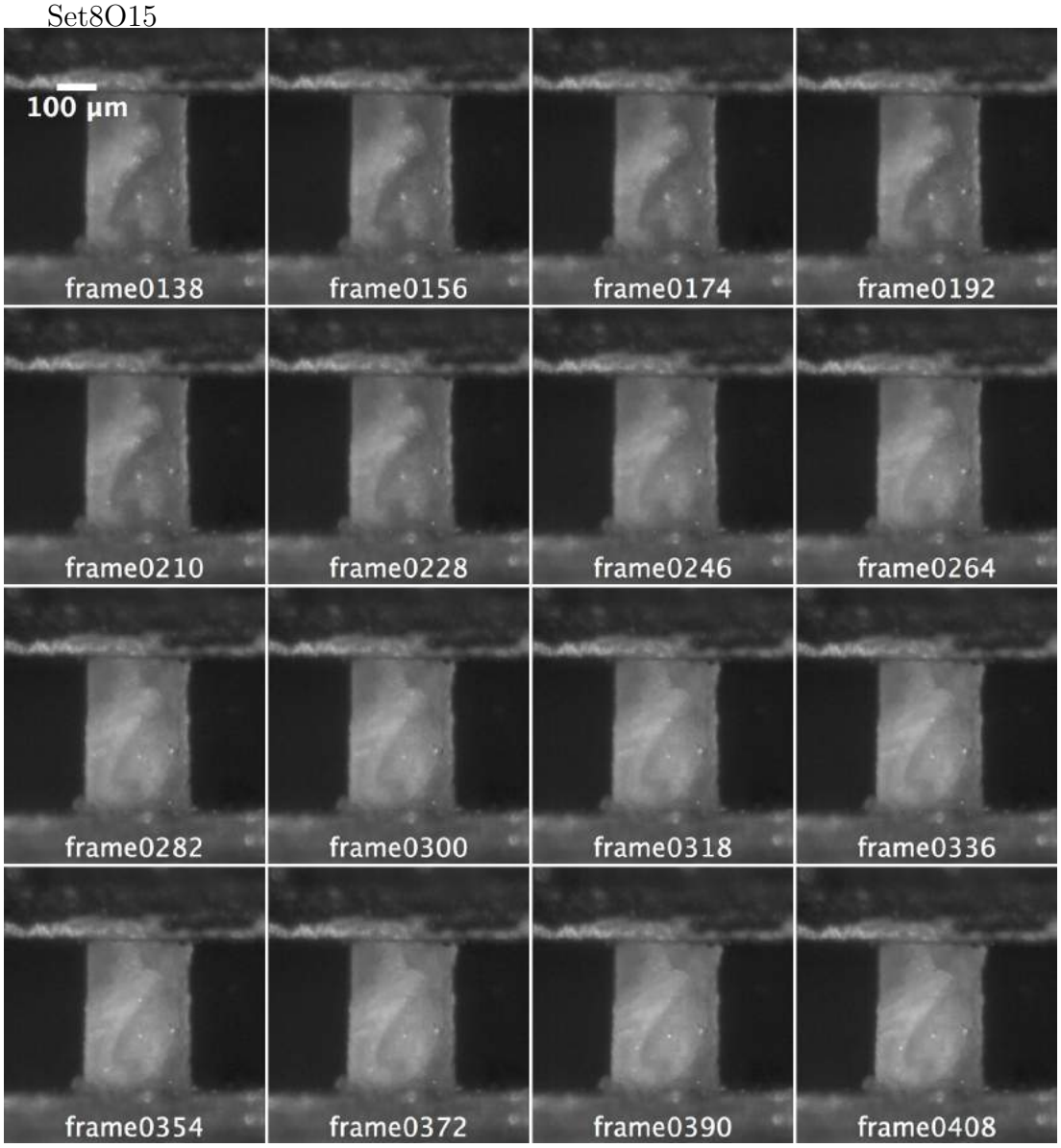
100 µm
frame0138
frame0156
frame0174
frame0192
frame0210
frame0228
frame0246
frame0264
frame0282
frame0300
frame0318
frame0336
frame0354
frame0372
frame0390
frame0408

Set8O16

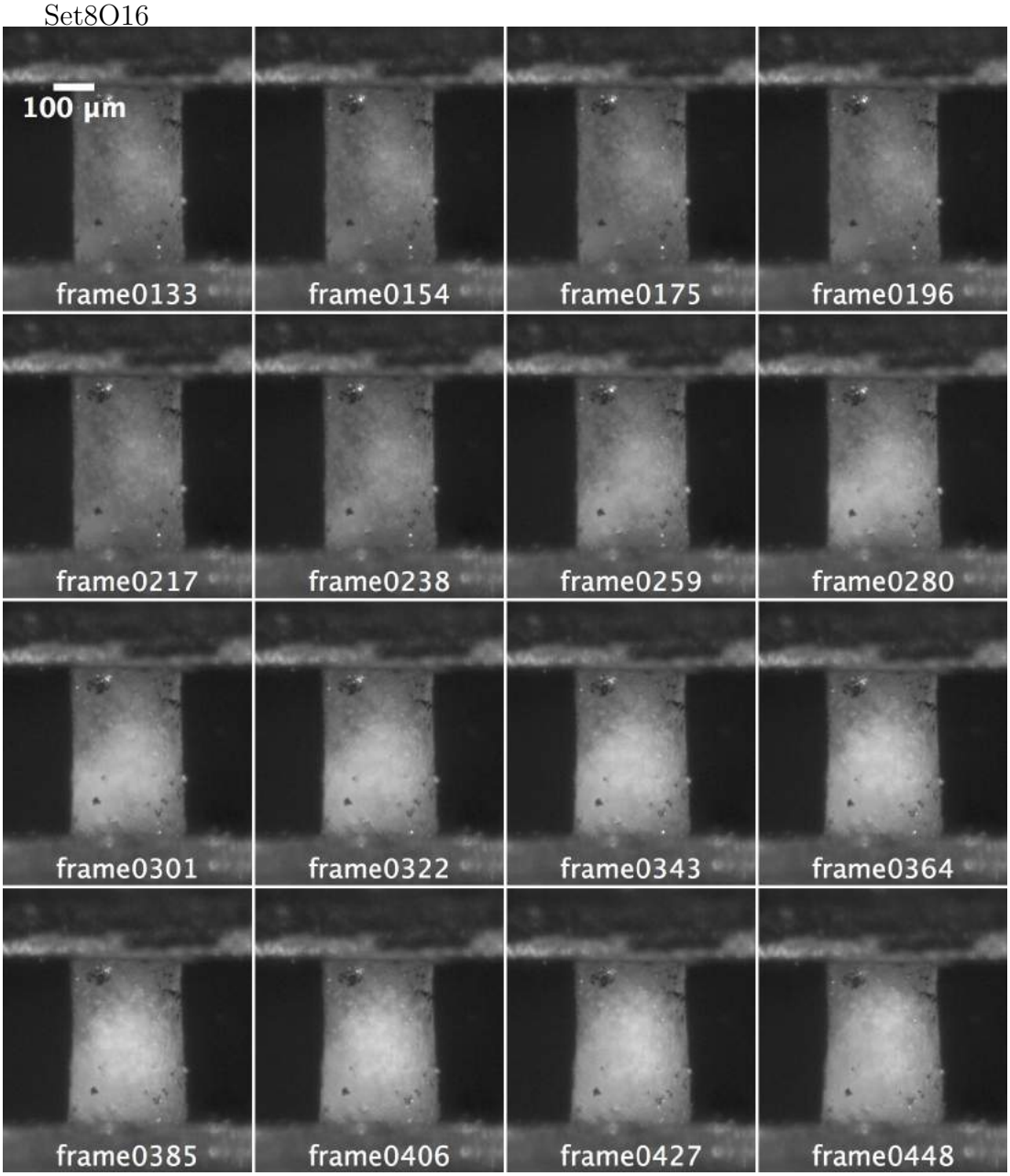
100 µm
frame0133
frame0154
frame0175
frame0196
frame0217
frame0238
frame0259
frame0280
frame0301
frame0322
frame0343
frame0364
frame0385
frame0406
frame0427
frame0448

Set8O17

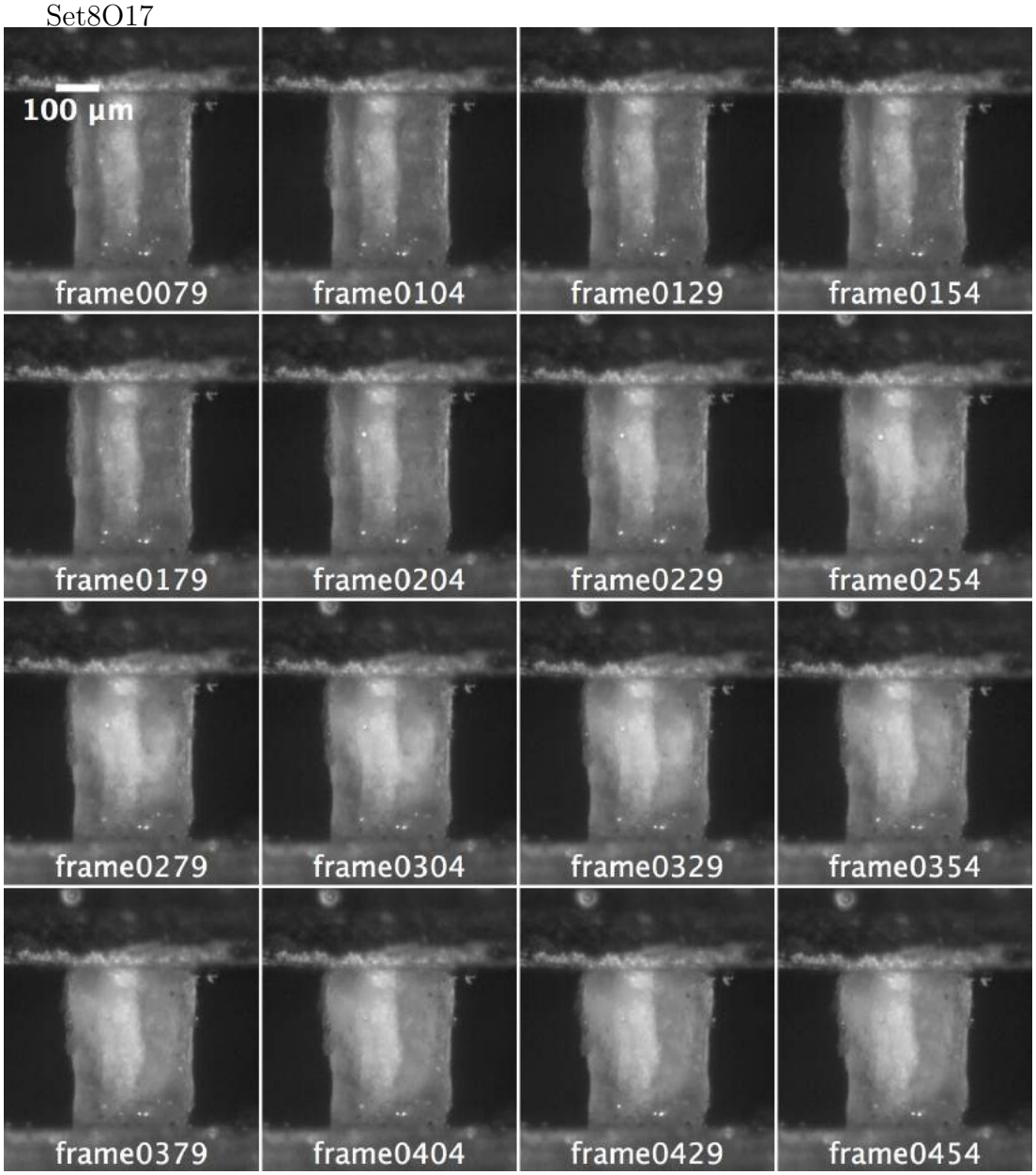
100 µm
frame0079
frame0104
frame0129
frame0154
frame0179
frame0204
frame0229
frame0254
frame0279
frame0304
frame0329
frame0354
frame0379
frame0404
frame0429
frame0454

Set8O18

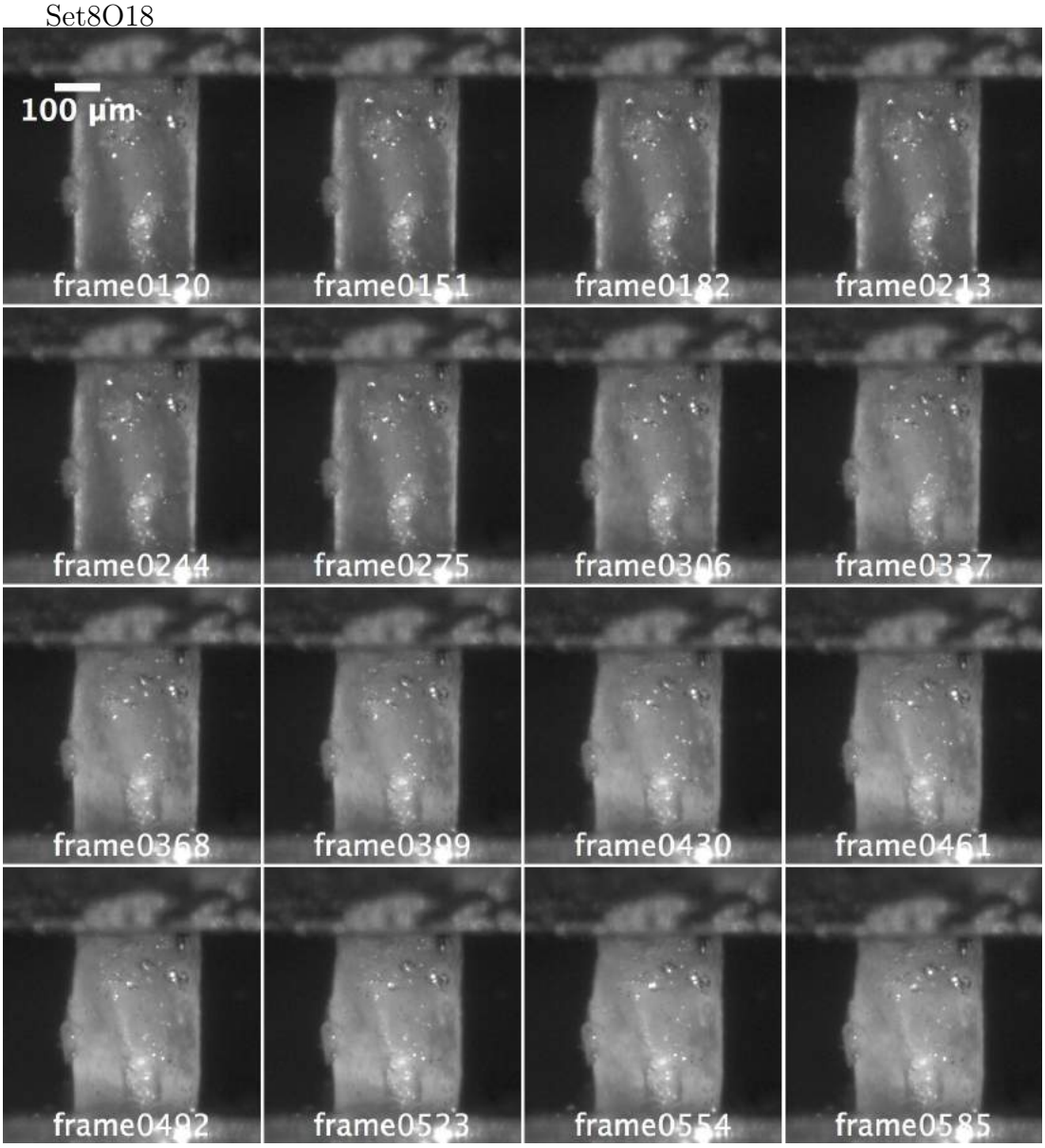
100 µm
frame0120
frame0151
frame0182
frame0213
frame0244
frame0275
frame0306
frame0337
frame0368
frame0399
frame0430
frame0461
frame0492
frame0523
frame0554
frame0585

Set8O19

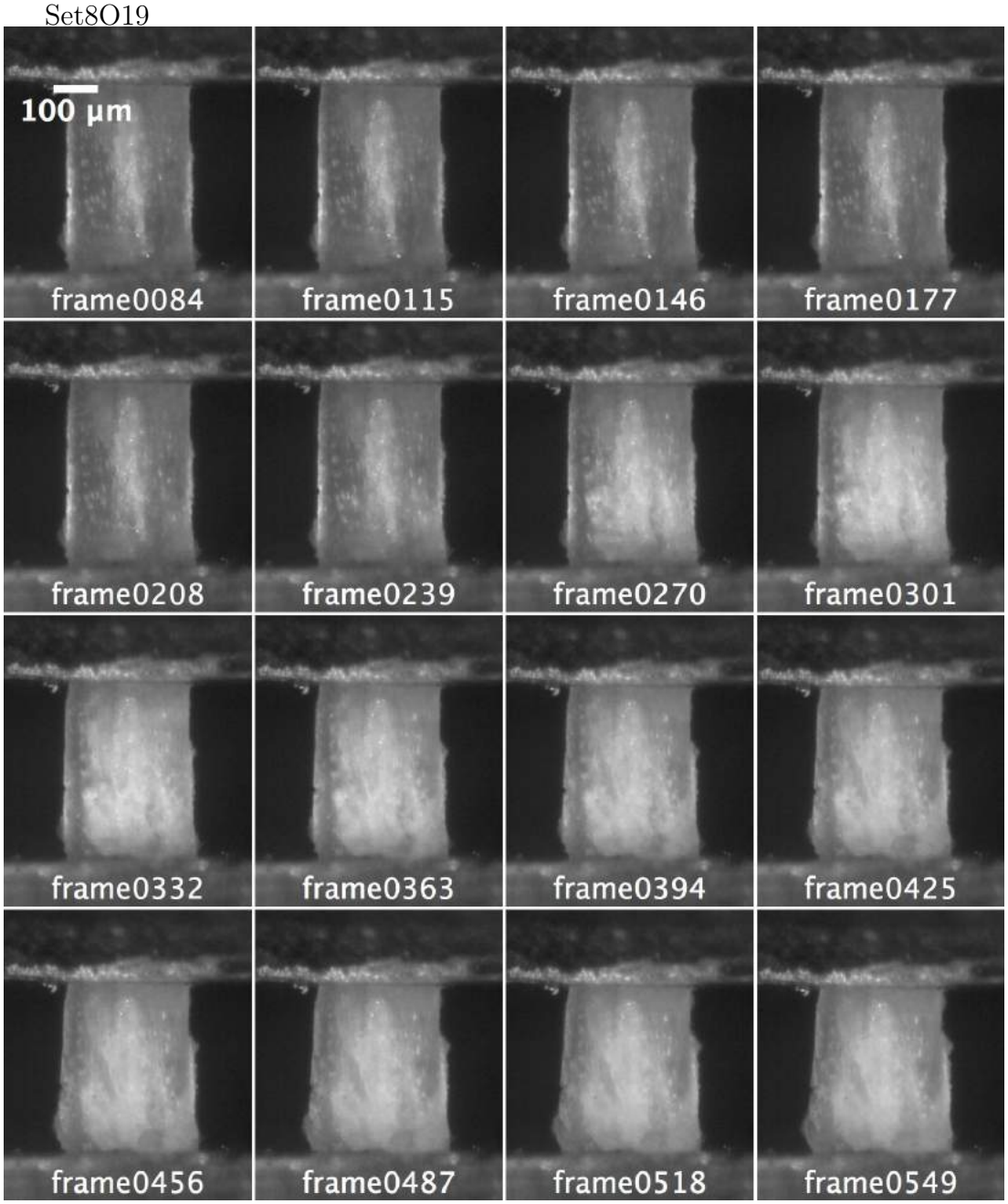
100 µm
frame0084
frame0115
frame0146
frame0177
frame0208
frame0239
frame0270
frame0301
frame0332
frame0363
frame0394
frame0425
frame0456
frame0487
frame0518
frame0549

Set9O02

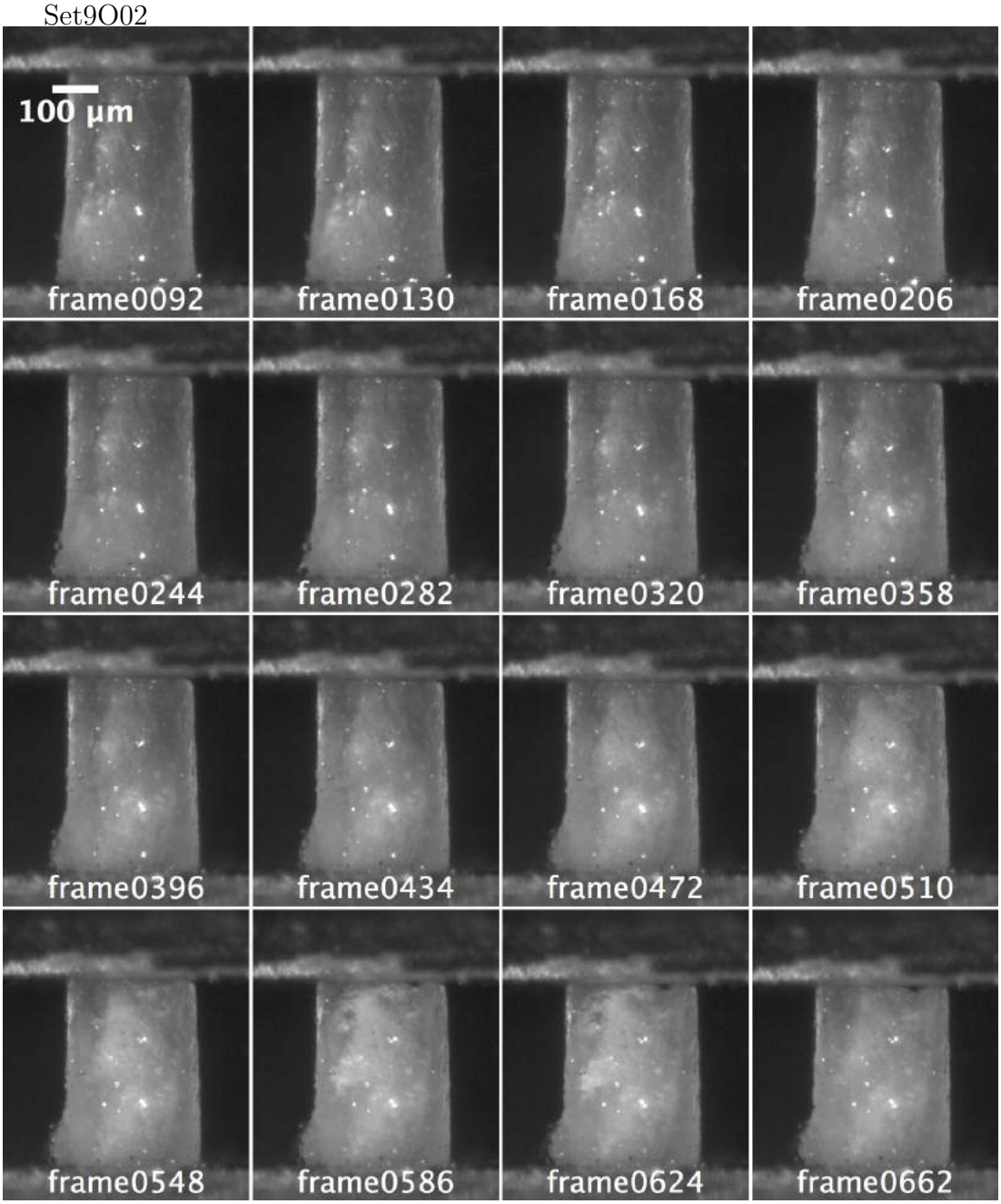
100 µm
frame0092
frame0130
frame0168
frame0206
frame0244
frame0282
frame0320
frame0358
frame0396
frame0434
frame0472
frame0510
frame0548
frame0586
frame0624
frame0662

Set9O03

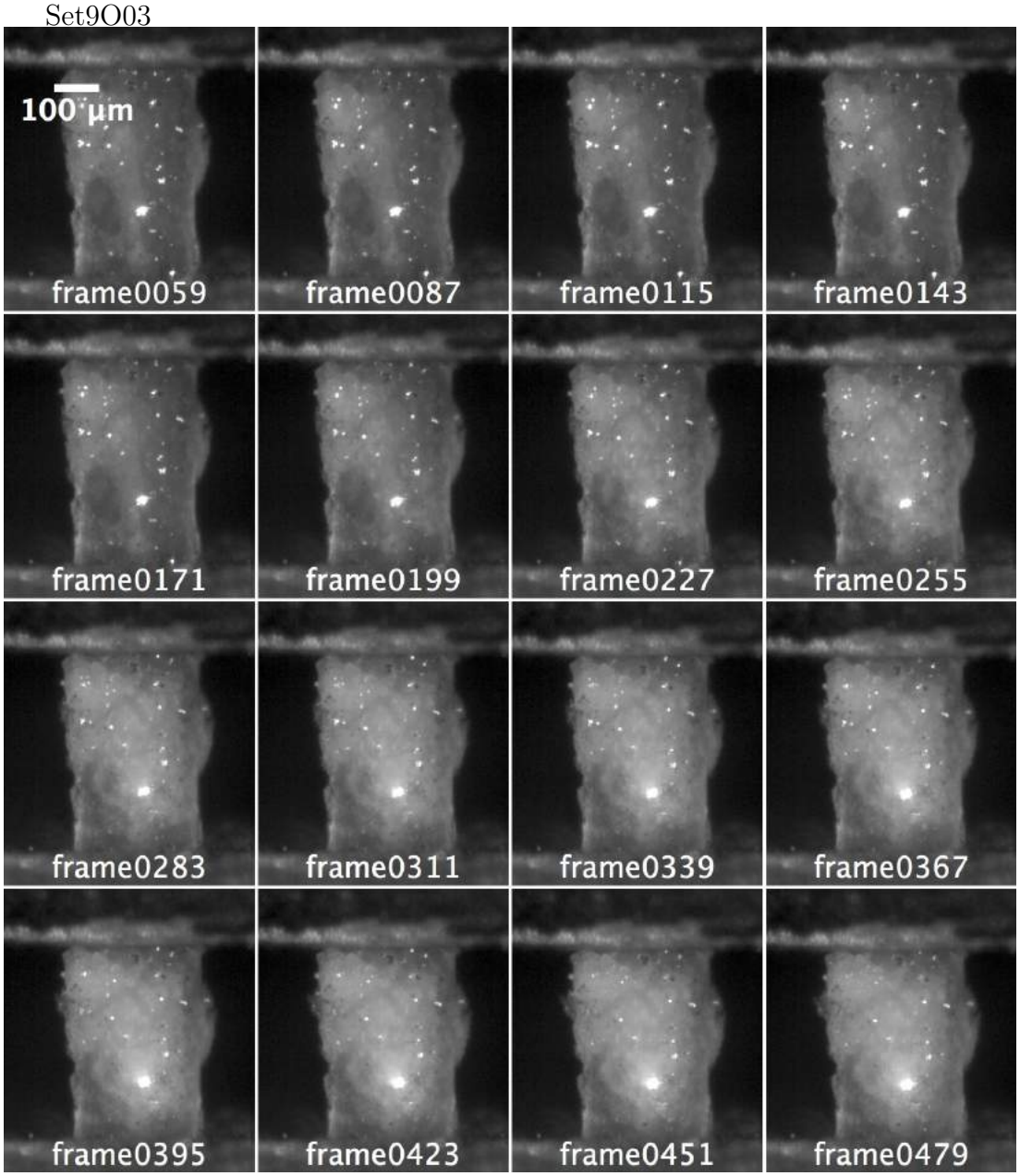
100 µm
frame0059
frame0087
frame0115
frame0143
frame0171
frame0199
frame0227
frame0255
frame0283
frame0311
frame0339
frame0367
frame0395
frame0423
frame0451
frame0479

Set9O04

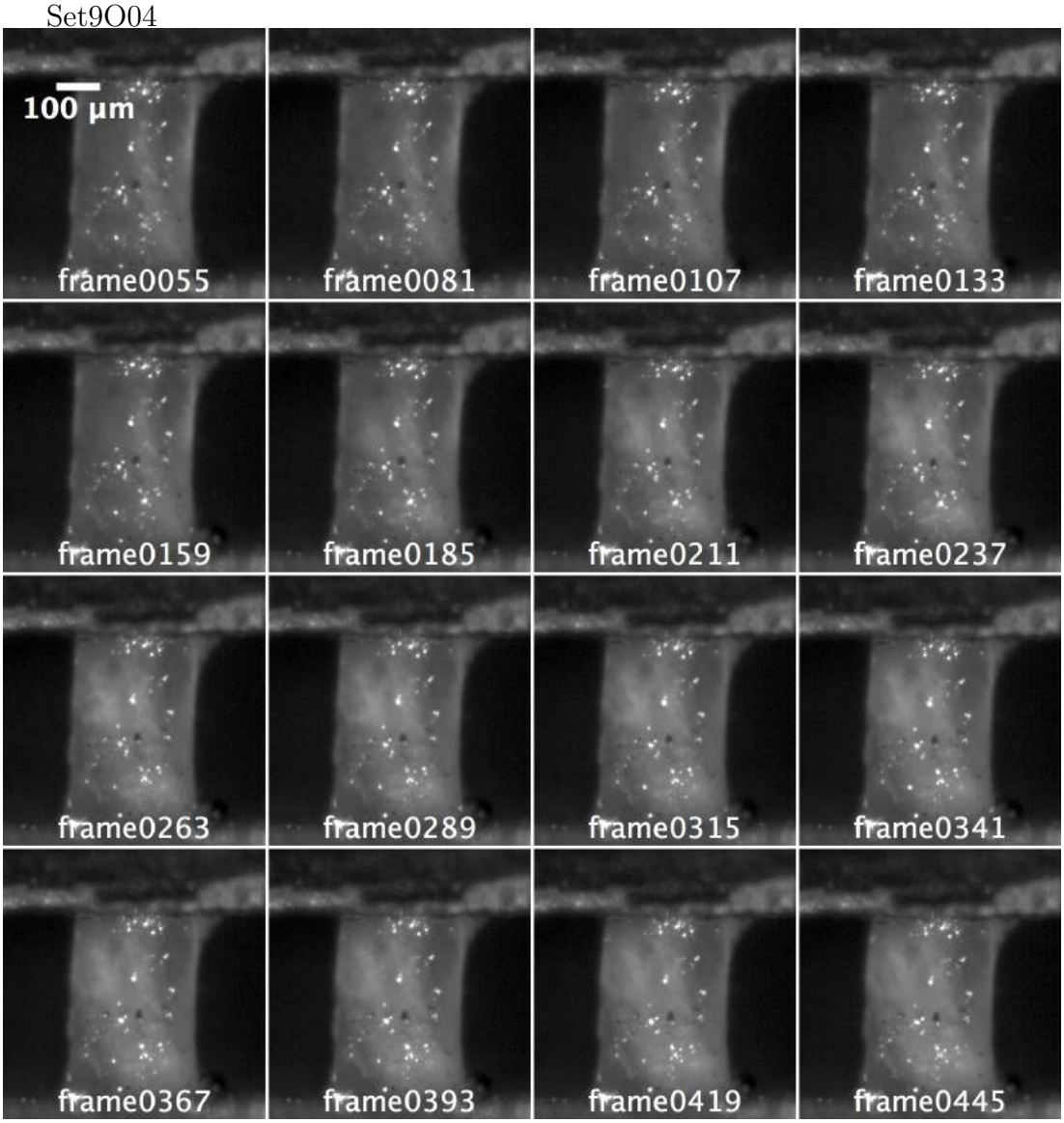
100 µm
frame0055
frame0081
frame0107
frame0133
frame0159
frame0185
frame0211
frame0237
frame0263
frame0289
frame0315
frame0341
frame0367
frame0393
frame0419
frame0445

Set9O05

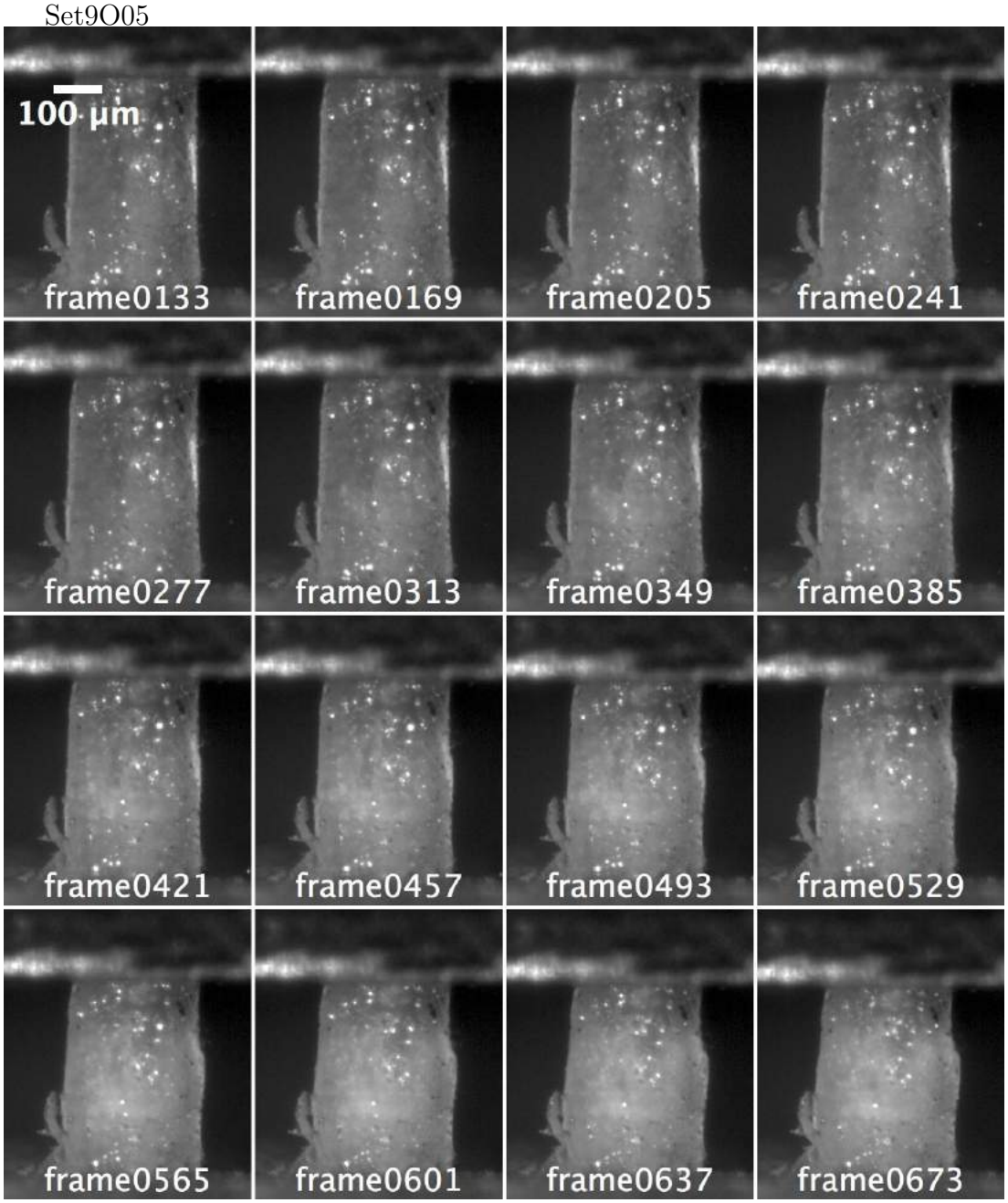
100 µm
frame0133
frame0169
frame0205
frame0241
frame0277
frame0313
frame0349
frame0385
frame0421
frame0457
frame0493
frame0529
frame0565
frame0601
frame0637
frame0673

Set9O06

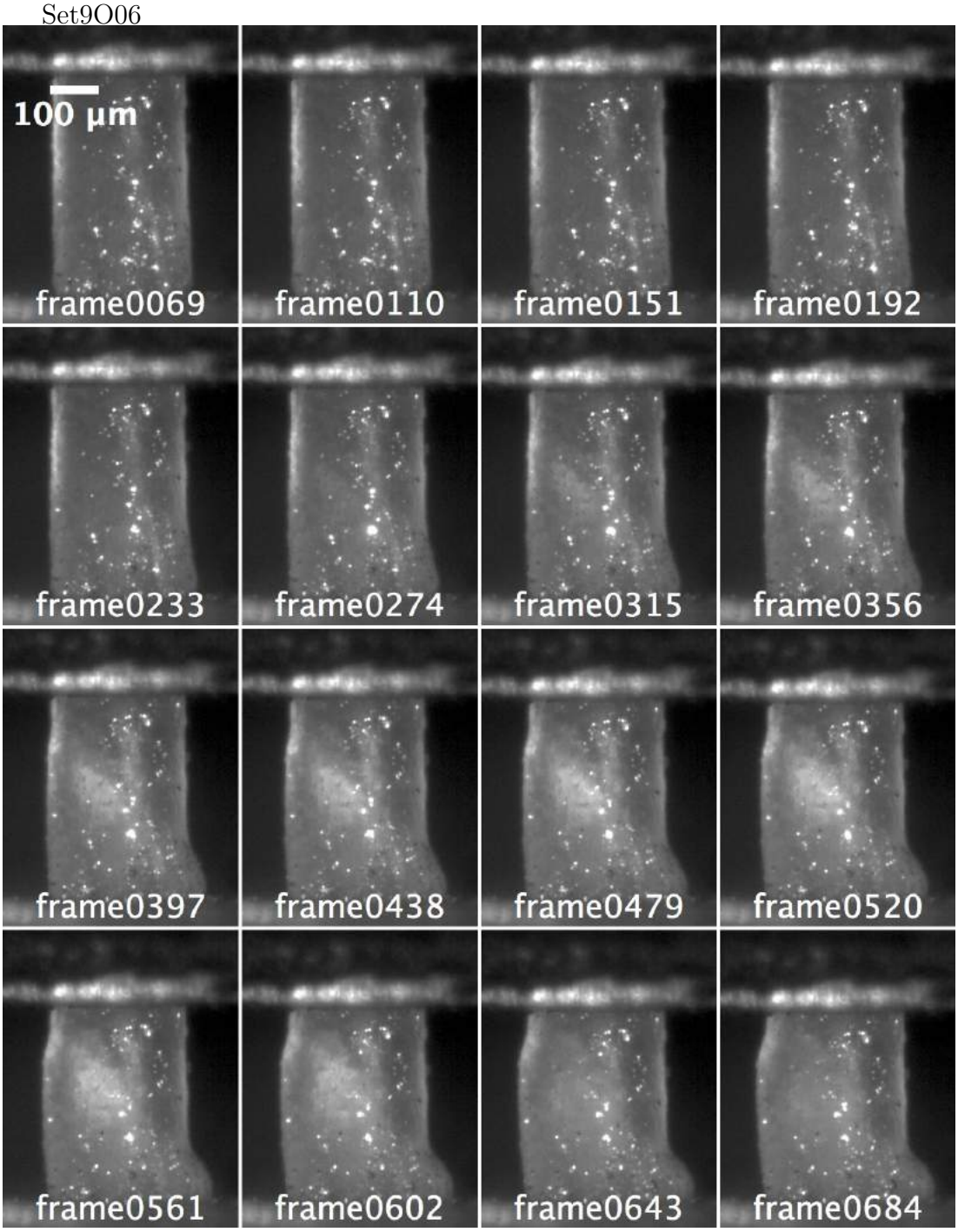
100 µm
frame0069
frame0110
frame0151
frame0192
frame0233
frame0274
frame0315
frame0356
frame0397
frame0438
frame0479
frame0520
frame0561
frame0602
frame0643
frame0684

Set9O07

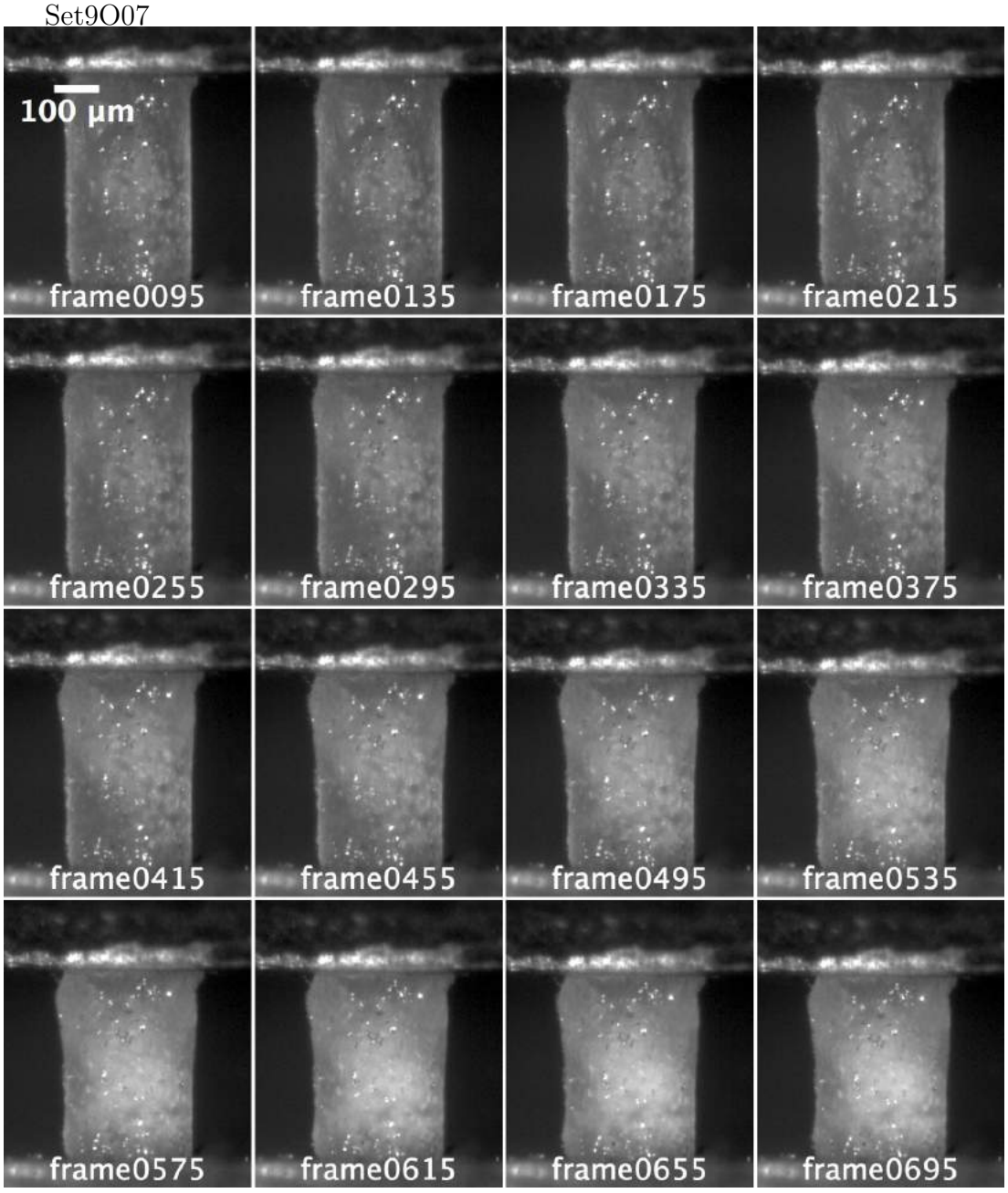
100 μm
frame0095
frame0135
frame0175
frame0215
frame0255
frame0295
frame0335
frame0375
frame0415
frame0455
frame0495
frame0535
frame0575
frame0615
frame0655
frame0695

Set9O08

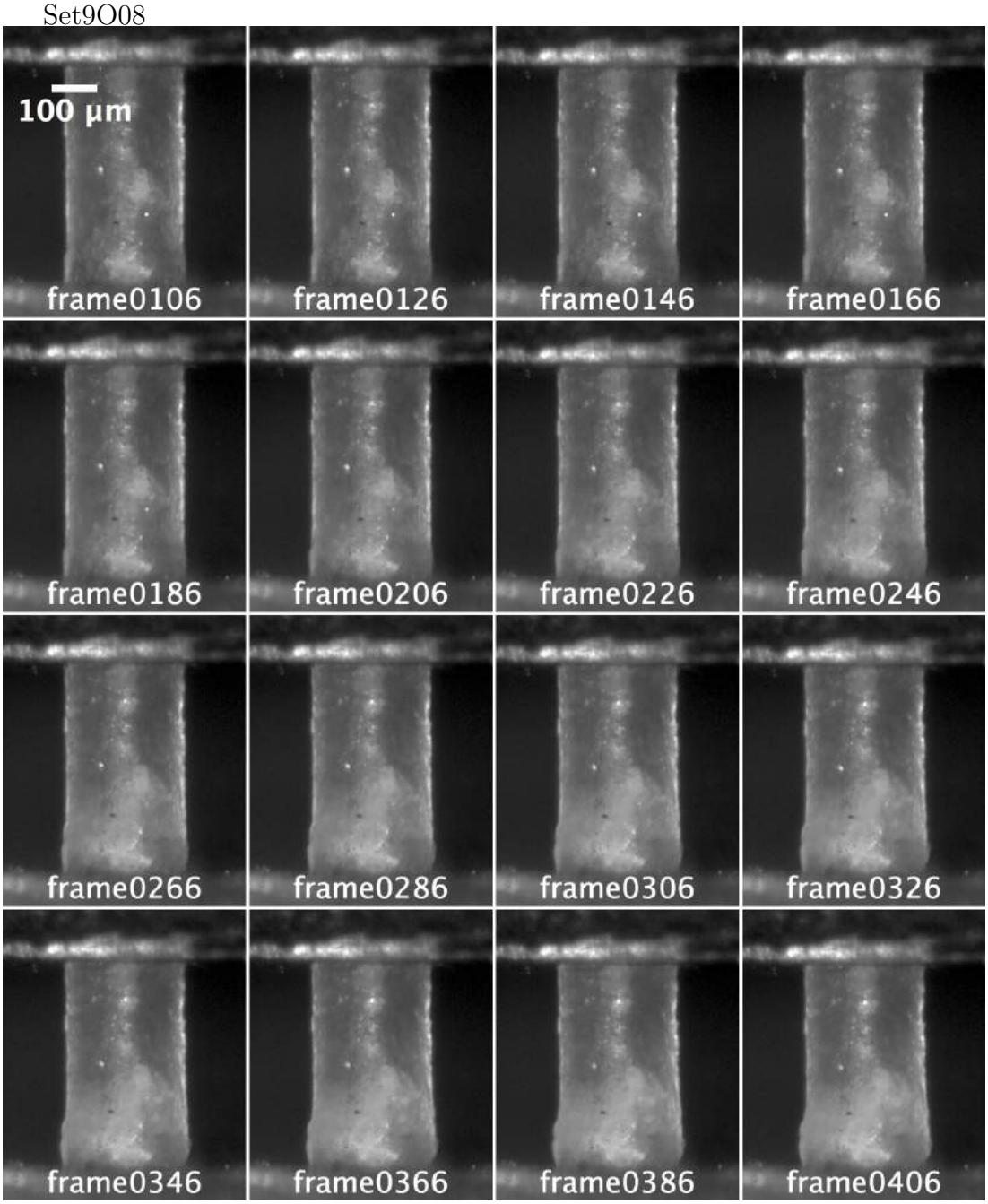
100 µm
frame0106
frame0126
frame0146
frame0166
frame0186
frame0206
frame0226
frame0246
frame0266
frame0286
frame0306
frame0326
frame0346
frame0366
frame0386
frame0406

Set9O09

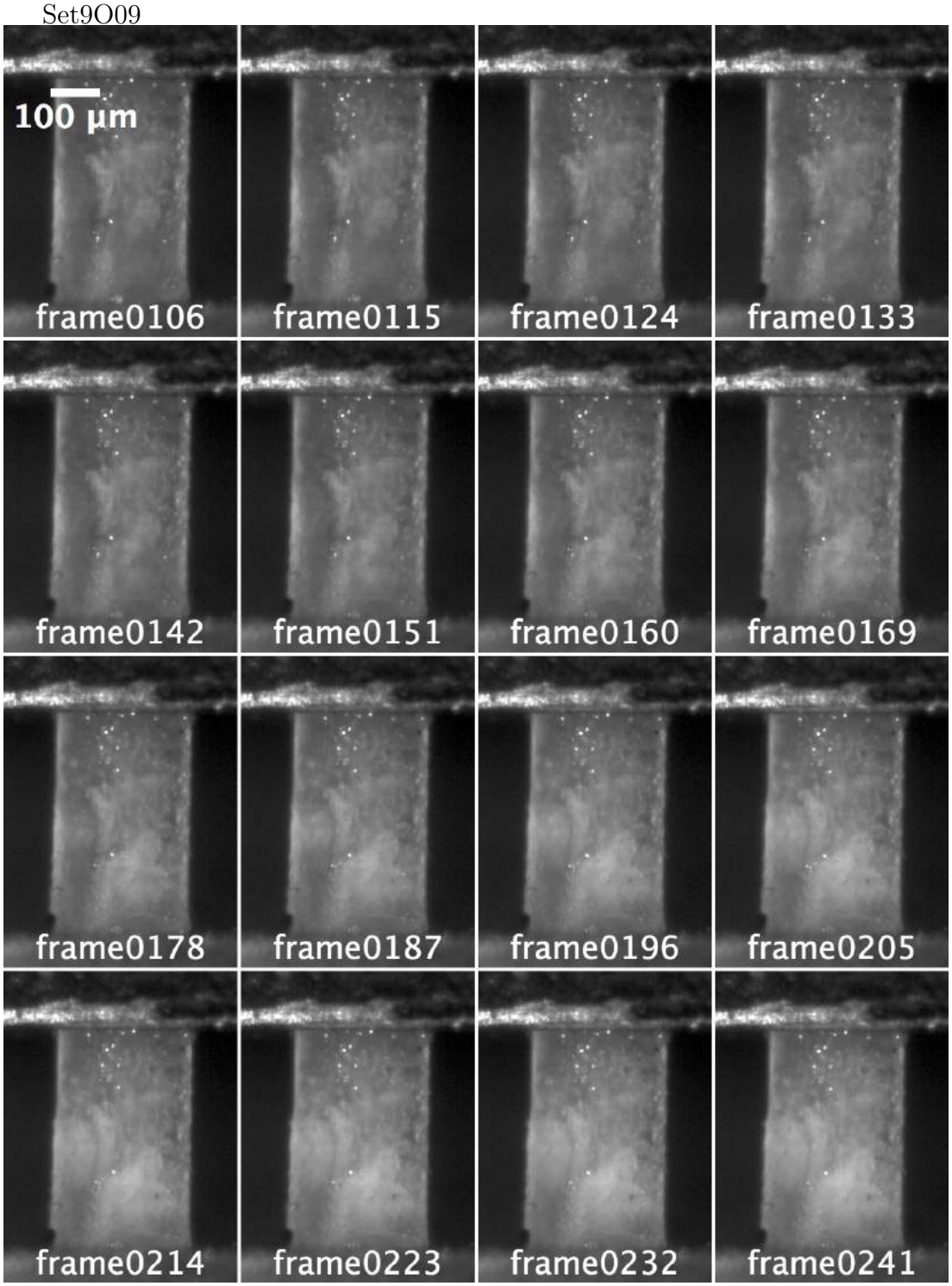
100 µm
frame0106
frame0115
frame0124
frame0133
frame0142
frame0151
frame0160
frame0169
frame0178
frame0187
frame0196
frame0205
frame0214
frame0223
frame0232
frame0241

Set9O10

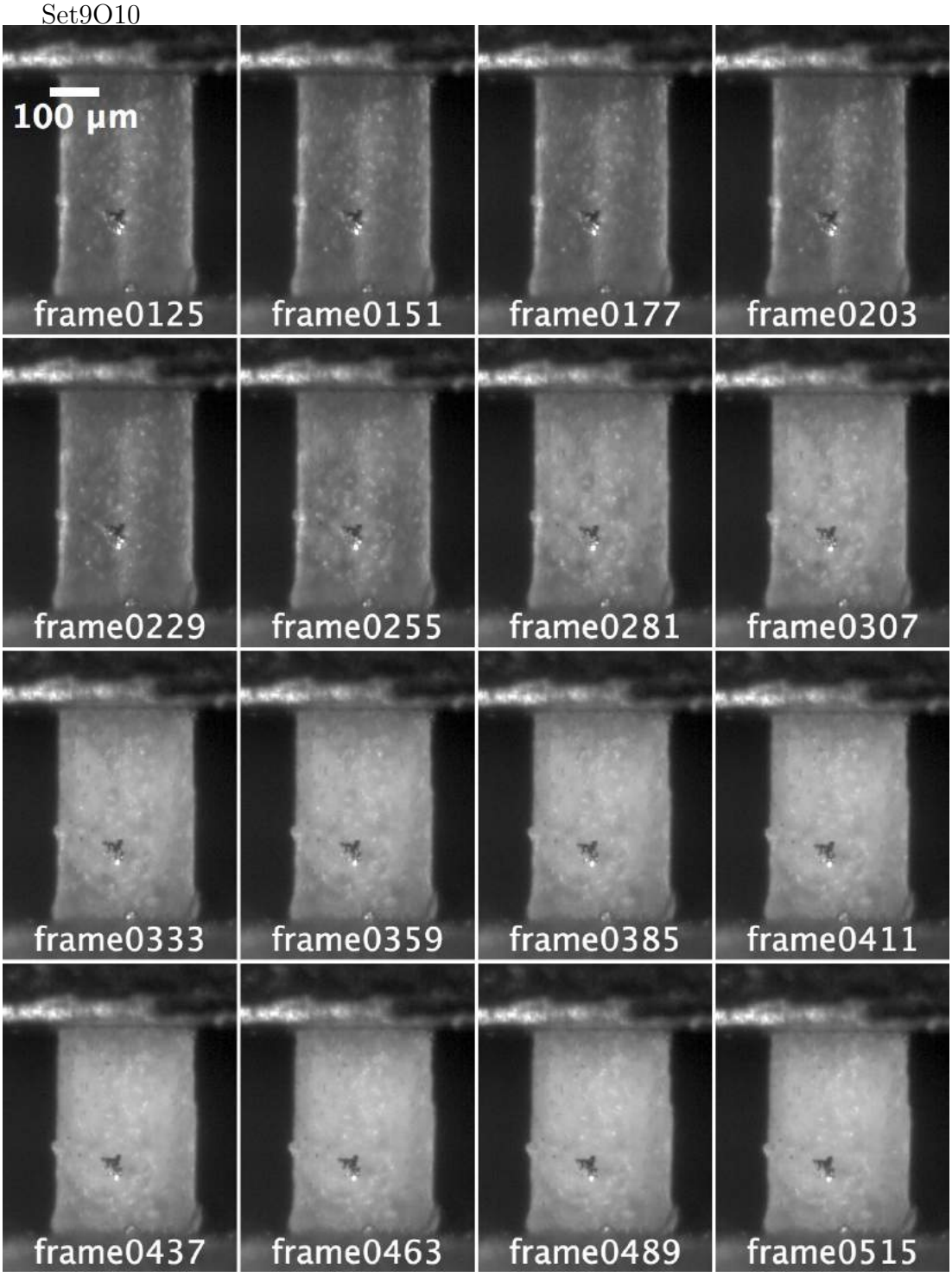
100 µm
frame0125
frame0151
frame0177
frame0203
frame0229
frame0255
frame0281
frame0307
frame0333
frame0359
frame0385
frame0411
frame0437
frame0463
frame0489
frame0515

Set9O11

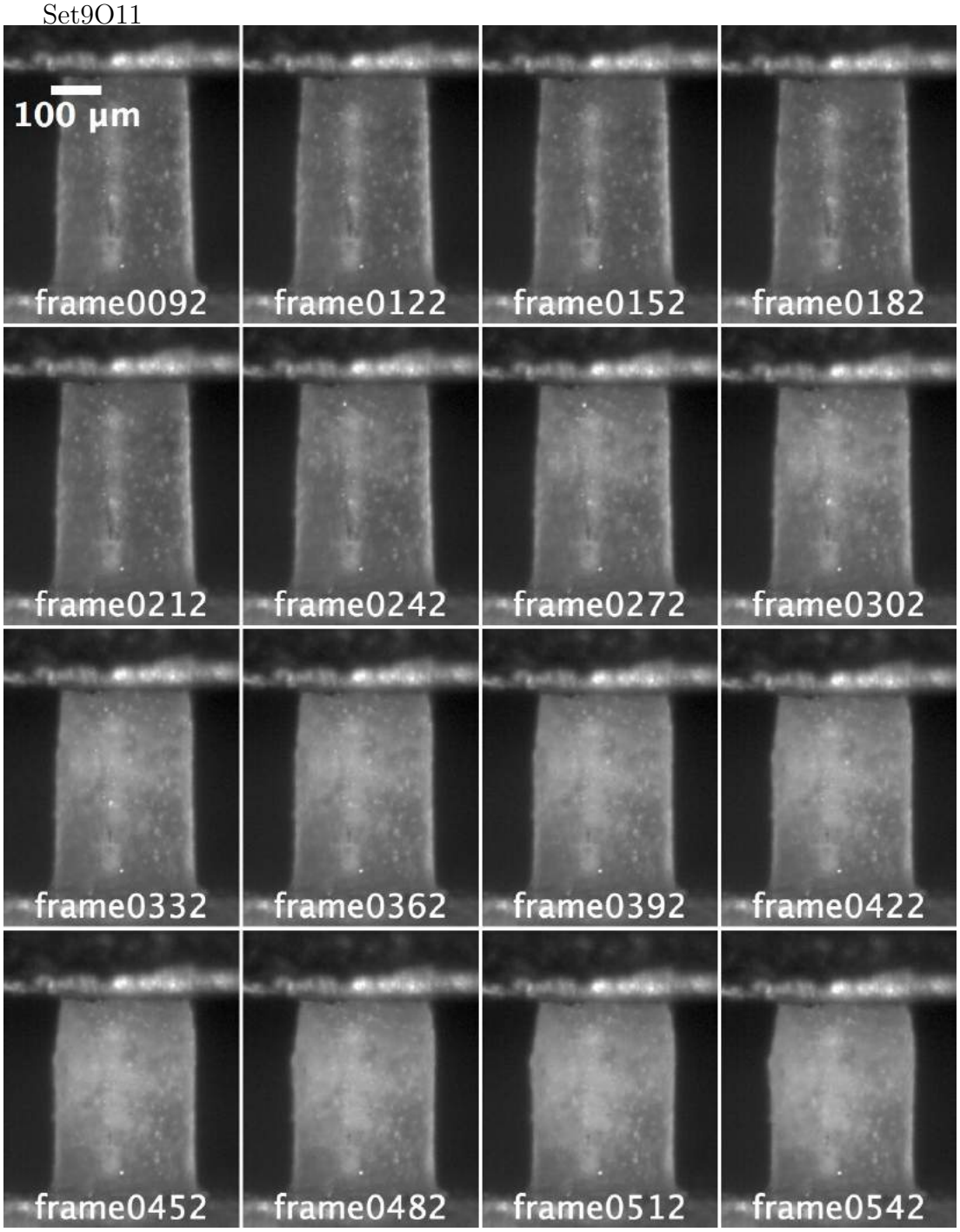
100 µm
frame0092
frame0122
frame0152
frame0182
frame0212
frame0242
frame0272
frame0302
frame0332
frame0362
frame0392
frame0422
frame0452
frame0482
frame0512
frame0542

Set9O12

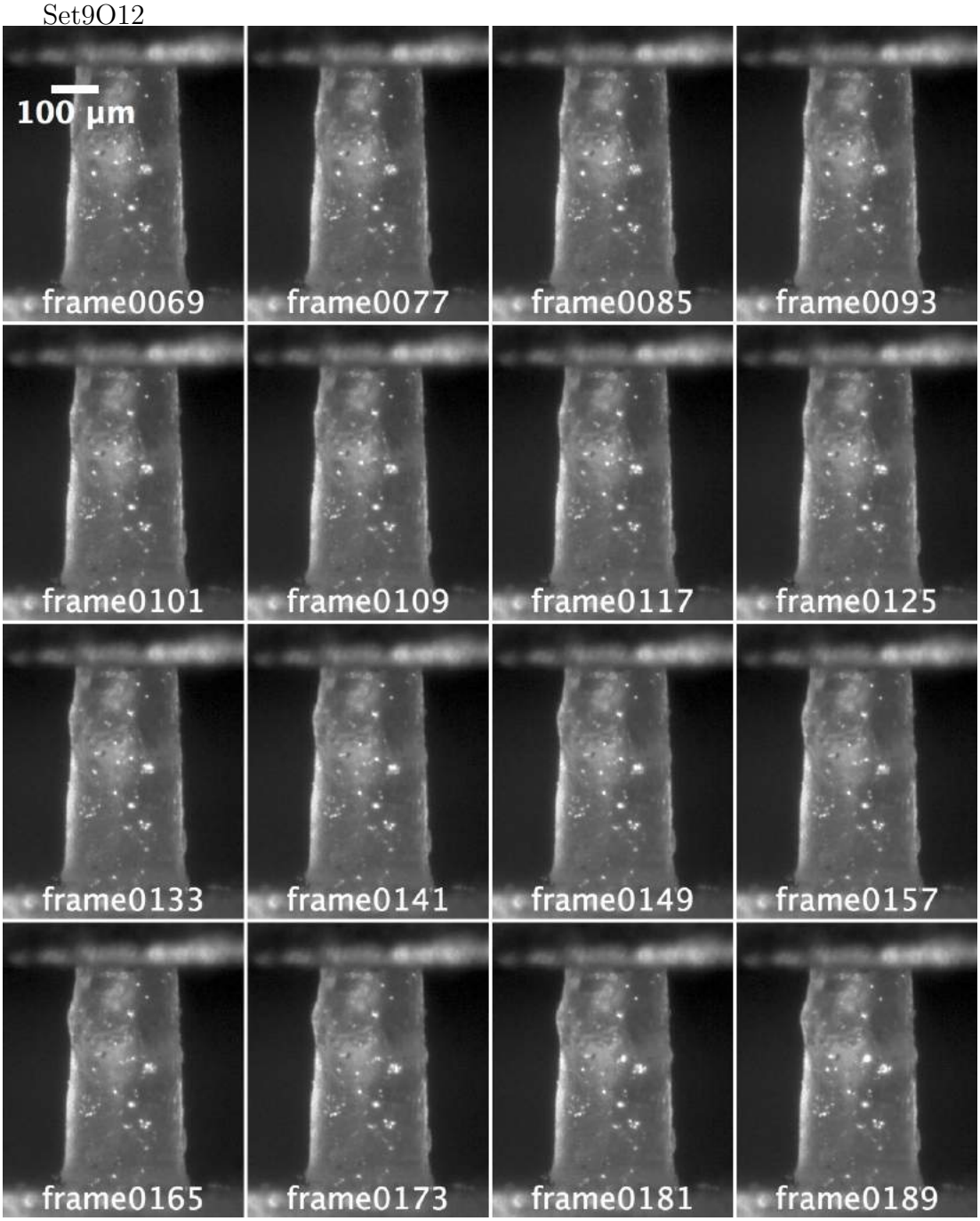
100 µm
frame0069
frame0077
frame0085
frame0093
frame0101
frame0109
frame0117
frame0125
frame0133
frame0141
frame0149
frame0157
frame0165
frame0173
frame0181
frame0189

Set9O14

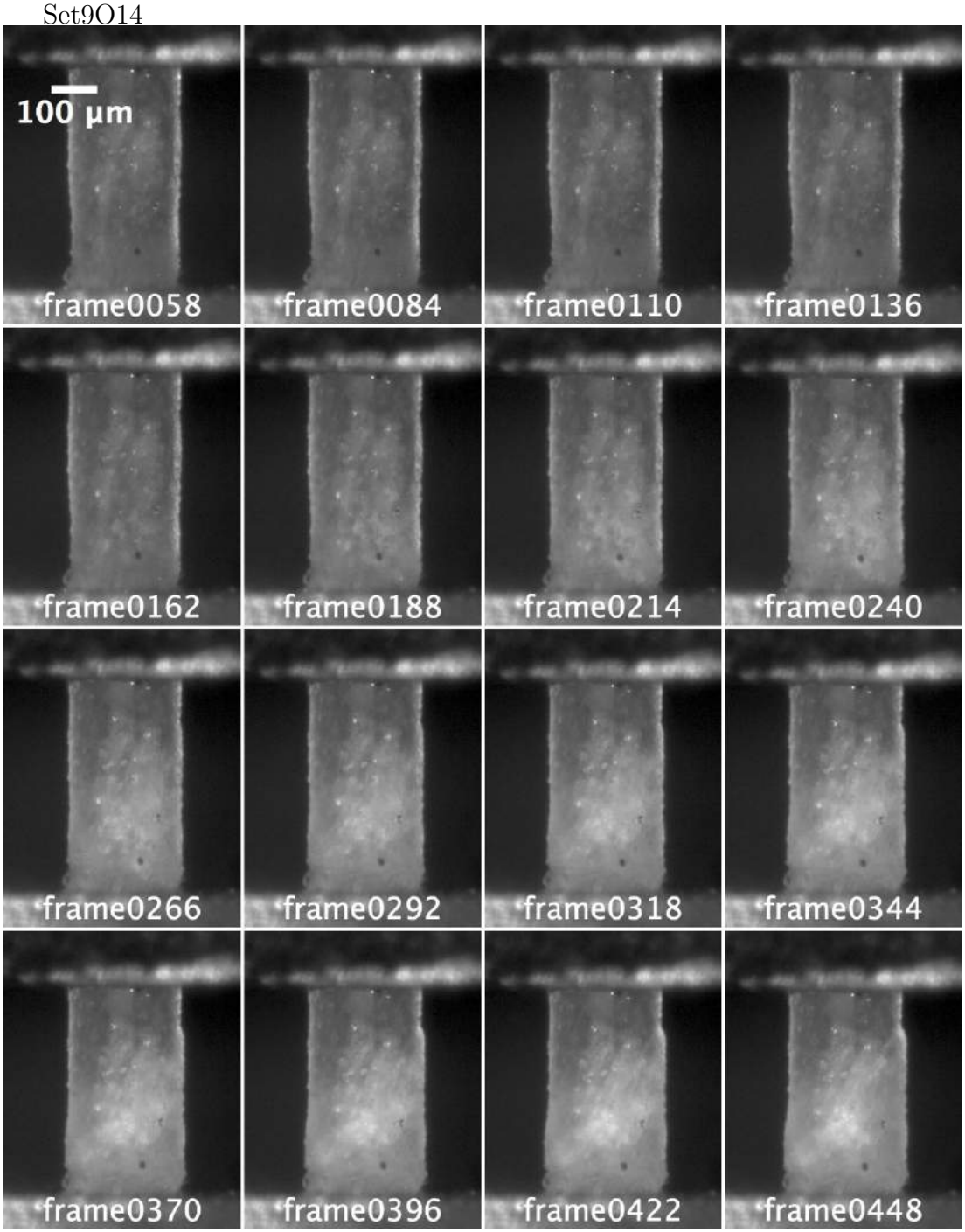
100 µm
frame0058
frame0084
frame0110
frame0136
frame0162
frame0188
frame0214
frame0240
frame0266
frame0292
frame0318
frame0344
frame0370
frame0396
frame0422
frame0448

Set9O15

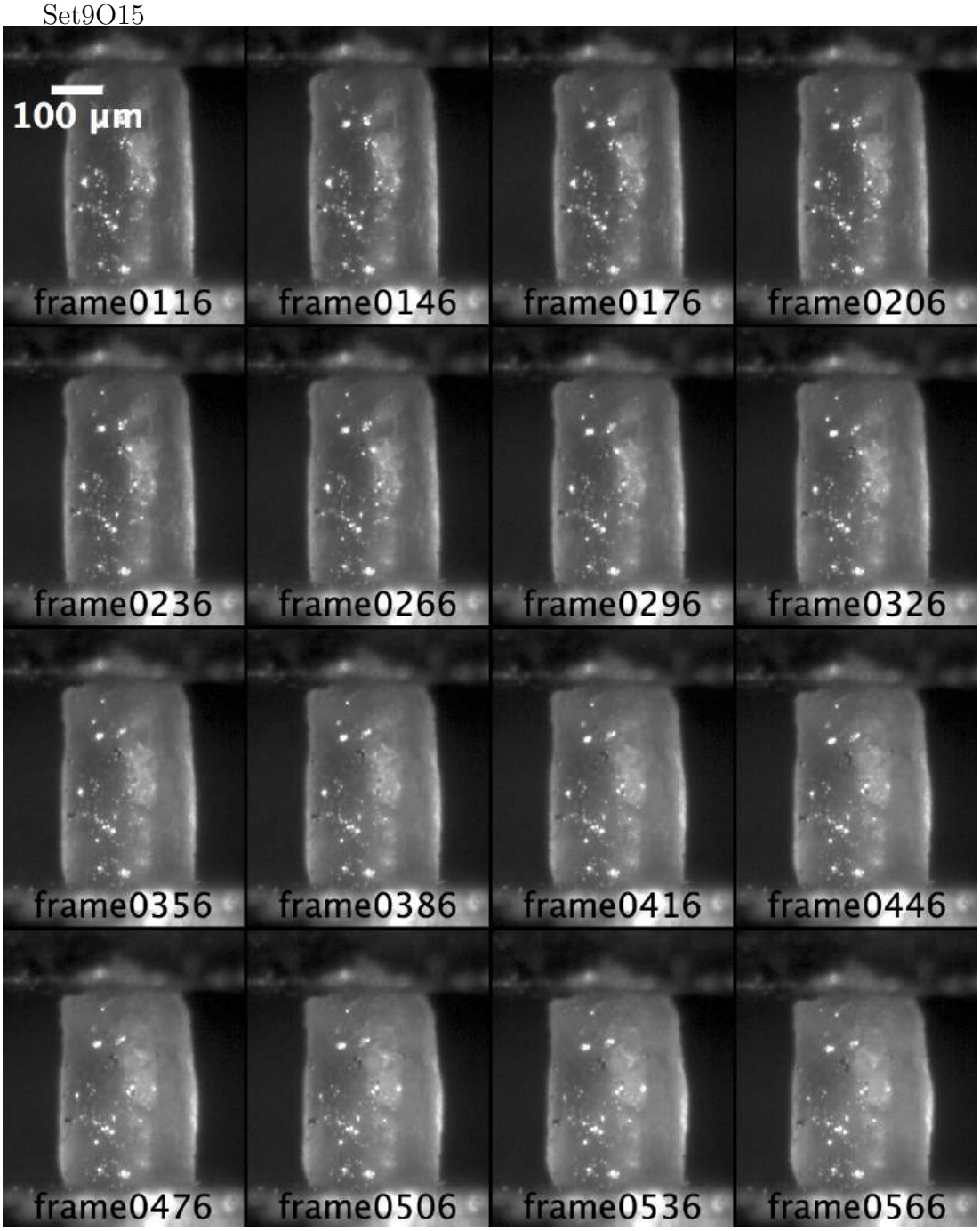
100 µm
frame0116
frame0146
frame0176
frame0206
frame0236
frame0266
frame0296
frame0326
frame0356
frame0386
frame0416
frame0446
frame0476
frame0506
frame0536
frame0566

Set9O16

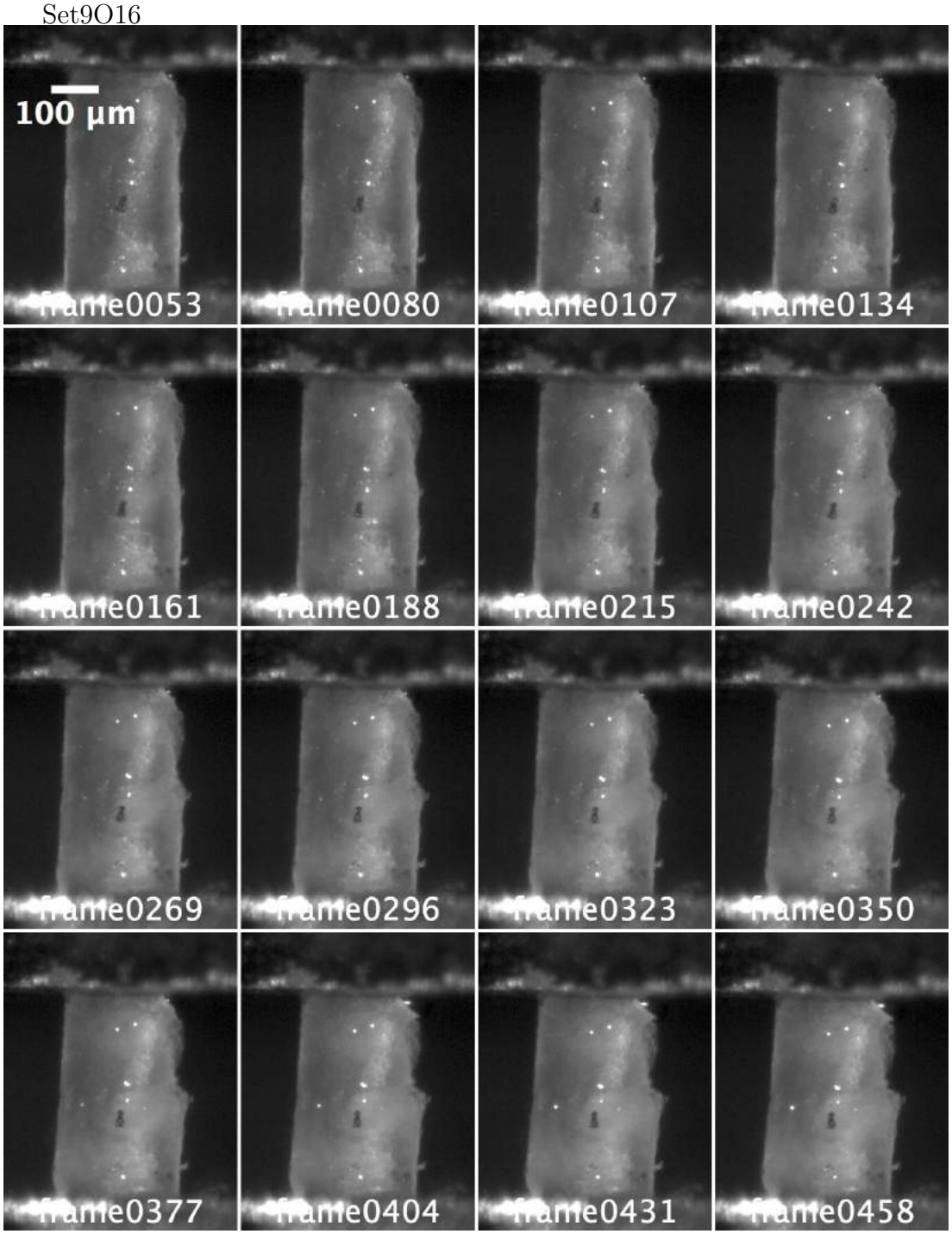
100 µm
frame0053
frame0080
frame0107
frame0134
frame0161
frame0188
frame0215
frame0242
frame0269
frame0296
frame0323
frame0350
frame0377
frame0404
frame0431
frame0458

Bibliography

[1] A. Ascenzi and E. Bonucci, "The compressive properties of single osteons," *Anatomical Record*, vol. 161, no. 3, pp. 377–391, 1968.

[2] K. W. Luczynski, A. Steiger-Thirsfeld, J. Bernardi, J. Eberhardsteiner, and C. Hellmich, "Extracellular bone matrix exhibits hardening elastoplasticity and more than double cortical strength: Evidence from homogeneous compression of non-tapered single micron-sized pillars welded to a rigid substrate," *Journal of the Mechanical Behavior of Biomedical Materials*, vol. 52, pp. 51–62, 2015.

[3] K. Storheim and J.-A. Zwart, "Musculoskeletal disorders and the Global Burden of Disease study," *Annals of the Rheumatic Diseases*, vol. 73, pp. 949–950, jun 2014.

[4] "Global Burden of Disease Study 2015 (GBD 2015) Risk Factor Results 1990-2015," 2016.

[5] S. Amin, S. J. Achenbach, E. J. Atkinson, S. Khosla, L. J. Melton, and III, "Trends in fracture incidence: a population-based study over 20 years.," *Journal of bone and mineral research : the official journal of the American Society for Bone and Mineral Research*, vol. 29, pp. 581–9, mar 2014.

[6] P. F. Lata and M. E. Elliott, "Patient assessment in the diagnosis, prevention, and treatment of osteoporosis.," *Nutrition in clinical practice : official publication of the American Society for Parenteral and Enteral Nutrition*, vol. 22, pp. 261–275, jun 2007.

[7] J. A. Kanis, "Osteoporosis III: Diagnosis of osteoporosis and assessment of fracture risk," *Lancet*, vol. 359, pp. 1929–1936, jun 2002.

[8] E. M. Curtis, R. J. Moon, E. M. Dennison, N. C. Harvey, and C. Cooper, "Recent advances in the pathogenesis and treatment of osteoporosis," *Clinical Medicine*, vol. 16, pp. 360–364, aug 2016.

[9] S. Weiner and H. D. Wagner, "The material bone: structure-mechanical function relations.," *Annu. Rev. Mater. Sci.*, vol. 28, no. 1, pp. 271–298, 1998.

[10] T. White and P. Folkens, *The Human Bone Manual*. 2005.

[11] B. Clarke, "Normal bone anatomy and physiology.," 2008.

[12] E. A. Zimmermann, B. Busse, and R. O. Ritchie, "The fracture mechanics of human bone: influence of disease and treatment," *BoneKEy Reports*, vol. 4, 2015.

[13] H. Gupta, U. Stachewicz, W. Wagermaier, P. Roschger, H. Wagner, and P. Fratzl, "Mechanical modulation at the lamellar level in osteonal bone," *Journal of Materials Research*, vol. 21, no. 08, pp. 1913–1921, 2006.

[14] Z. Fan, J. G. Swadener, J. Y. Rho, M. E. Roy, and G. M. Pharr, "Anisotropic properties of human tibial cortical bone as measured by nanoindentation," *Journal of Orthopaedic Research*, vol. 20, no. 4, pp. 806–810, 2002.

[15] D. B. Burr, M. B. Schaffler, and R. G. Frederickson, "Composition of the cement line and its possible mechanical role as a local interface in human compact bone," *Journal of Biomechanics*, vol. 21, no. 11, 1988.

[16] R. Korsa, J. Lukes, J. Sepitka, and T. Mares, "Elastic Properties of Human Osteon and Osteonal Lamella Computed by a Bidirectional Micromechanical Model and Validated by Nanoindentation," *Journal of Biomechanical Engineering*, vol. 137, p. 081002, aug 2015.

[17] E. P. Katz and S.-T. Li, "Structure and function of bone collagen fibrils," *Journal of Molecular Biology*, vol. 80, no. 1, pp. 1–15, 1973.

[18] J. P. R. O. Orgel, T. C. Irving, A. Miller, and T. J. Wess, "Microfibrillar structure of type I collagen in situ," *Proceedings of the National Academy of Sciences*, vol. 103, no. 24, pp. 9001–9005, 2006.

[19] B. Alexander, T. L. Daulton, G. M. Genin, J. Lipner, J. D. Pasteris, B. Wopenka, and S. Thomopoulos, "The nanometre-scale physiology of bone: steric modelling and scanning transmission electron microscopy of collagen-mineral structure," *Journal of The Royal Society Interface*, vol. 9, no. 73, pp. 1774–1786, 2012.

[20] O. Johnell and J. A. Kanis, "An estimate of the worldwide prevalence, mortality and disability associated with hip fracture," *Osteoporosis International*, vol. 15, pp. 897–902, dec 2004.

[21] W. Tong, M. J. Glimcher, J. L. Katz, L. Kuhn, and S. J. Eppell, "Size and shape of mineralites in young bovine bone measured by atomic force microscopy," in *Calcified Tissue International*, vol. 72, pp. 592–598, 2003.

[22] M. D. Shoulders and R. T. Raines, "Collagen Structure and Stability," *Annual Review of Biochemistry*, vol. 78, no. 1, pp. 929–958, 2009.

[23] H. Ping, H. Xie, B.-l. Su, Y.-b. Cheng, W. Wang, H. Wang, Y. Wang, J. Zhang, F. Zhang, and Z. Fu, "Organized intrafibrillar mineralization, directed by a rationally designed multi-functional protein," *J. Mater. Chem. B*, vol. 3, no. 22, pp. 4496–4502, 2015.

[24] R. F. M. van Oers, R. Ruimerman, B. van Rietbergen, P. A. J. Hilbers, and R. Huiskes, "Relating osteon diameter to strain," *Bone*, vol. 43, no. 3, pp. 476–482, 2008.

[25] R. Georgia, I. Albu, M. Sico, and M. Georoceanu, "Comparative Aspects of the Density and Diameter of Haversian Canals in the Diaphyseal Compact Bone of Man and Dog," *Morphol Embryol (Bucur)*, vol. 28, no. 1, pp. 11–14, 1982.

[26] E. Bonucci and P. M. Motta, *Ultrastructure of skeletal tissues: bone and cartilage in health and disease*. 1990.

[27] W. Gebhardt, "Über funktionell wichtige Anordnungsweisen der feineren und gröberen Bauelemente des Wirbeltierknochens II. Spezieller Teil. 1. Der Bau der Haversschen Lamellensysteme und seine funktionelle Bedeutung," *Arch Entwickl Mech Org*, vol. 20, pp. 187–322, 1906.

[28] Y. H. An and R. a. Draughn, "Mechanical Testing of Bone and the Bone-Implant Interface," *Medical*, 1999.

[29] M. M. Giraud-Guille, "Twisted plywood architecture of collagen fibrils in human compact bone osteons," *Calcified Tissue International*, vol. 42, no. 3, pp. 167–180, 1988.

[30] S. Weiner, T. Arad, I. Sabanay, and W. Traub, "Rotated plywood structure of primary lamellar bone in the rat: Orientations of the collagen fibril arrays," *Bone*, vol. 20, no. 6, pp. 509–514, 1997.

[31] W. Wagermaier, H. S. Gupta, A. Gourrier, M. Burghammer, P. Roschger, and P. Fratzl, "Spiral twisting of fiber orientation inside bone lamellae," *Biointerphases*, vol. 1, no. 1, pp. 1–5, 2006.

[32] G. Marotti, M.-A. Muglia, and C. Palumbo, "Structure and Function of Lamellar Bone," 1994.

[33] J. Mitchell and A. H. van Heteren, "A literature review of the spatial organization of lamellar bone," *Comptes Rendus - Palevol*, vol. 15, no. 1-2, pp. 23–31, 2016.

[34] M. B. Schaffler, W.-Y. Cheung, R. Majeska, and O. Kennedy, "Osteocytes: Master Orchestrators of Bone," *Calcified Tissue International*, vol. 94, pp. 5–24, jan 2014.

[35] T. T. Hlaing and J. E. Compston, "Biochemical markers of bone turnover – uses and limitations," *Annals of Clinical Biochemistry*, vol. 51, no. 2, pp. 189–202, 2014.

[36] L. J. Raggatt and N. C. Partridge, "Cellular and molecular mechanisms of bone remodeling.," *The Journal of biological chemistry*, vol. 285, no. 33, pp. 25103–8, 2010.

[37] X. Feng and J. M. McDonald, "Disorders of Bone Remodeling," *Annual Review of Pathology: Mechanisms of Disease*, vol. 6, no. 1, pp. 121–145, 2011.

[38] S. T. Chamberlain, Andrew T.; Forbes, "A preliminary study of microscopic evidence for lactation in cattle," *The Zooarchaeology of Fats, Oils, Milk and Dairying.*, pp. pp. 44–49., 2005.

[39] M.-G. Ascenzi, "The osteon: the micromechanical unit of compact bone," *Frontiers in Bioscience*, vol. 17, no. 1, p. 1551, 2012.

[40] A. Bernhard, P. Milovanovic, E. A. Zimmermann, M. Hahn, D. Djonic, M. Krause, S. Breer, K. Püschel, M. Djuric, M. Amling, and B. Busse,

"Micro-morphological properties of osteons reveal changes in cortical bone stability during aging, osteoporosis, and bisphosphonate treatment in women," *Osteoporosis International*, vol. 24, pp. 2671–2680, oct 2013.

[41] J. D. Currey, "Some Effects of Ageing in Human Haversian Systems," *Journal of anatomy*, vol. 98, pp. 69–75, 1964.

[42] I. J. Singh and D. L. Gunberg, "Estimation of age at death in human males from quantitative histology of bone fragments," *American Journal of Physical Anthropology*, vol. 33, no. 3, pp. 373–381, 1970.

[43] E. A. Zimmermann, E. Schaible, H. Bale, H. D. Barth, S. Y. Tang, P. Reichert, B. Busse, T. Alliston, J. W. Ager, and R. O. Ritchie, "Age-related changes in the plasticity and toughness of human cortical bone at multiple length scales," *Proceedings of the National Academy of Sciences*, vol. 108, no. 35, pp. 14416–14421, 2011.

[44] H. M. Britz, C. D. L. Thomas, J. G. Clement, and D. M. L. Cooper, "The relation of femoral osteon geometry to age, sex, height and weight," *Bone*, vol. 45, no. 1, pp. 77–83, 2009.

[45] O. L. Katsamenis, T. Jenkins, and P. J. Thurner, "Toughness and damage susceptibility in human cortical bone is proportional to mechanical inhomogeneity at the osteonal-level," *Bone*, vol. 76, pp. 158–168, jul 2015.

[46] Y. N. Yeni and T. L. Norman, "Calculation of porosity and osteonal cement line effects on the effective fracture toughness of cortical bone in longitudinal crack growth.," *Journal of biomedical materials research*, vol. 51, pp. 504–9, sep 2000.

[47] R. B. Martin, D. B. Burr, N. A. Sharkey, and D. P. Fyhrie, *Skeletal tissue mechanics*, vol. 112. Springer, 2015.

[48] A. Ascenzi and E. Bonucci, "The tensile properties of single osteons," *The Anatomical Record*, vol. 158, no. 4, pp. 375–386, 1967.

[49] A. Ascenzi, P. Baschieri, and A. Benvenuti, "The bending properties of single osteons.," *Journal of biomechanics*, vol. 23, no. 8, pp. 763–71, 1990.

[50] J. Y. Rho, R. B. Ashman, and C. H. Turner, "Young's modulus of trabecular and cortical bone material: Ultrasonic and microtensile measurements," *Journal of Biomechanics*, vol. 26, no. 2, pp. 111–119, 1993.

[51] D. T. Reilly and A. H. Burstein, "The Mechanical Properties of Cortical Bone," *The Journal of Bone and Joint Surgery*, vol. 56, no. 5, pp. 1001–1022, 1974.

[52] V. Frankel and M. Nordin, *Basic Biomechanics of the Skeletal System*. 1980.

[53] A. A. Poundarik and D. Vashishth, "Multiscale imaging of bone microdamage.," *Connective tissue research*, vol. 56, no. 2, pp. 87–98, 2015.

[54] V. H. Nguyen, T. Lemaire, and S. Naili, "Influence of interstitial bone microcracks on strain-induced fluid flow," *Biomechanics and Modeling in Mechanobiology*, vol. 10, no. 6, pp. 963–972, 2011.

[55] F. J. O'Brien, D. Taylor, and T. C. Lee, "The effect of bone microstructure on the initiation and growth of microcracks," *Journal of Orthopaedic Research*, vol. 23, no. 2, pp. 475–480, 2005.

[56] Z. Seref-Ferlengez, J. Basta-Pljakic, O. D. Kennedy, C. J. Philemon, and M. B. Schaffler, "Structural and mechanical repair of diffuse damage in cortical bone in vivo," *Journal of Bone and Mineral Research*, vol. 29, no. 12, pp. 2537–2544, 2014.

[57] J. Y. Rho, T. Y. Tsui, and G. M. Pharr, "Elastic properties of human cortical and trabecular lamellar bone measured by nanoindentation," *Biomaterials*, vol. 18, no. 20, pp. 1325–1330, 1997.

[58] D. Vashishth, "Hierarchy of bone microdamage at multiple length scales," *International Journal of Fatigue*, vol. 29, no. 6, pp. 1024–1033, 2007.

[59] A. A. Poundarik, T. Diab, G. E. Sroga, A. Ural, A. L. Boskey, C. M. Gundberg, and D. Vashishth, "Dilatational band formation in bone," *Proceedings of the National Academy of Sciences of the United States of America*, vol. 109, no. 47, pp. 19178–19183, 2012.

[60] P. J. Thurner, C. G. Chen, S. Ionova-Martin, L. Sun, A. Harman, A. Porter, J. W. Ager, R. O. Ritchie, and T. Alliston, "Osteopontin deficiency increases bone fragility but preserves bone mass," *Bone*, vol. 46, no. 6, pp. 1564–1573, 2010.

[61] A. Ascenzi, P. Baschieri, and A. Benvenuti, "The torsional properties of single selected osteons," *Journal of Biomechanics*, vol. 27, pp. 875–884, jul 1994.

[62] P. Frasca, R. A. Harper, and J. L. Katz, "Isolation of single osteons and osteon lamellae," *Acta Anat (Basel)*, vol. 95, no. 1, pp. 122–129, 1976.

[63] M. Doube, M. M. Klosowski, I. Arganda-Carreras, F. P. Cordelières, R. P. Dougherty, J. S. Jackson, B. Schmid, J. R. Hutchinson, and S. J. Shefelbine, "BoneJ: Free and extensible bone image analysis in ImageJ," *Bone*, vol. 47, no. 6, pp. 1076–1079, 2010.

[64] P. Campagnola, "Second harmonic generation imaging microscopy: Applications to diseases diagnostics," *Analytical Chemistry*, vol. 83, no. 9, pp. 3224–3231, 2011.

[65] I. R. Savage, E. S. Pearson, and H. O. Hartley, "Biometrika Tables for Statisticians," *Mathematics of Computation*, vol. 21, no. 98, p. 271, 1967.

[66] X. J. Wang, X. B. Chen, P. D. Hodgson, and C. E. Wen, "Elastic modulus and hardness of cortical and trabecular bovine bone measured by nanoindentation," *Transactions of Nonferrous Metals Society of China (English Edition)*, vol. 16, no. SUPPL., 2006.

[67] P. K. Zysset, "Indentation of bone tissue: A short review," in *Osteoporosis International*, vol. 20, pp. 1049–1055, 2009.

[68] Z. Manilay, E. Novitskaya, E. Sadovnikov, and J. McKittrick, "A comparative study of young and mature bovine cortical bone," *Acta Biomaterialia*, vol. 9, no. 2, pp. 5280–5288, 2013.

[69] C. J. Hernandez and T. M. Keaveny, "A biomechanical perspective on bone quality," 2006.

[70] E. Torres-Del-Pliego, L. Vilaplana, R. Güerri-Fernández, and A. Diez-Pérez, "Measuring bone quality," *Current Rheumatology Reports*, vol. 15, no. 11, 2013.

[71] J. Schwiedrzik, R. Raghavan, A. Bürki, V. LeNader, U. Wolfram, J. Michler, and P. Zysset, "In situ micropillar compression reveals superior strength and ductility but an absence of damage in lamellar bone.," *Nature materials*, vol. 13, no. June, pp. 1–8, 2014.

[72] X. Sun, J. Hoon Jeon, J. Blendell, and O. Akkus, "Visualization of a phantom post-yield deformation process in cortical bone," *Journal of Biomechanics*, vol. 43, no. 10, pp. 1989–1996, 2010.

[73] P. J. Thurner, B. Erickson, R. Jungmann, Z. Schriock, J. C. Weaver, G. E. Fantner, G. Schitter, D. E. Morse, and P. K. Hansma, "High-speed photography of compressed human trabecular bone correlates whitening to microscopic damage," *Engineering Fracture Mechanics*, vol. 74, no. 12, pp. 1928–1941, 2007.

[74] T. Diab, K. W. Condon, D. B. Burr, and D. Vashishth, "Age-related change in the damage morphology of human cortical bone and its role in bone fragility," *Bone*, vol. 38, no. 3, pp. 427–431, 2006.